MODEL-BASED STRIPMAP SYNTHETIC APERTURE RADAR PROCESSING

by

Roger D. West

A dissertation submitted in partial fulfillment
of the requirements for the degree

of

DOCTOR OF PHILOSOPHY

in

Electrical Engineering

Approved:

Dr. Jacob H. Gunther Major Professor	Dr. Todd K. Moon Committee Member
Dr. Randy J. Jost Committee Member	Dr. Wei Ren Committee Member
Dr. Mark E. Fels Committee Member	Dr. Byron R. Burnham Dean of Graduate Studies

UTAH STATE UNIVERSITY
Logan, Utah

2011

Abstract

Model-Based Stripmap Synthetic Aperture Radar Processing

by

Roger D. West, Doctor of Philosophy

Utah State University, 2011

Major Professor: Dr. Jacob H. Gunther
Department: Electrical and Computer Engineering

Synthetic aperture radar (SAR) is a type of remote sensor that provides its own illumination and is capable of forming high resolution images of the reflectivity of a scene. The reflectivity of the scene that is measured is dependent on the choice of carrier frequency; different carrier frequencies will yield different images of the same scene.

There are different modes for SAR sensors; two common modes are spotlight mode and stripmap mode. Furthermore, SAR sensors can either be continuously transmitting a signal, or they can transmit a pulse at some pulse repetition frequency (PRF). The work in this dissertation is for pulsed stripmap SAR sensors.

The resolvable limit of closely spaced reflectors in range is determined by the bandwidth of the transmitted signal and the resolvable limit in azimuth is determined by the bandwidth of the induced azimuth signal, which is strongly dependent on the length of the physical antenna on the SAR sensor. The point-spread function (PSF) of a SAR system is determined by these resolvable limits and is limited by the physical attributes of the SAR sensor.

The PSF of a SAR system can be defined in different ways. For example, it can be defined in terms of the SAR system including the image processing algorithm. By using this definition, the PSF is an algorithm-specific sinc-like function and produces the bright, star-like artifacts that are noticeable around strong reflectors in the focused image. The

PSF can also be defined in terms of just the SAR system before any image processing algorithm is applied. This second definition of the PSF will be used in this dissertation. Using this definition, the bright, algorithm-specific, star-like artifacts will be denoted as the inter-pixel interference (IPI) of the algorithm. To be specific, the combined effect of the second definition of PSF and the algorithm-dependent IPI is a decomposition of the first definition of PSF.

A new comprehensive forward model for stripmap SAR is derived in this dissertation. New image formation methods are derived in this dissertation that invert this forward model and it is shown that the IPI that corrupts traditionally processed stripmap SAR images can be removed. The removal of the IPI can increase the resolvability to the resolution limit, thus making image analysis much easier.

SAR data is inherently corrupted by uncompensated phase errors. These phase errors lower the contrast of the image and corrupt the azimuth processing which inhibits proper focusing (to the point of the reconstructed image being unusable). If these phase errors are not compensated for, the images formed by system inversion are useless, as well. A model-based autofocus method is also derived in this dissertation that complements the forward model and corrects these phase errors before system inversion.

(167 pages)

To Jenny, Kaitlynd, Ethan, and Dylan...

Acknowledgments

I would first like to thank my advisor, Dr. Jake Gunther, for all of his ideas, suggestions, and patience over the years; this dissertation would never have materialized without his continual guidance. I am very thankful to Dr. Todd Moon for all of the help and ideas that he has provided over the years. I would also like to thank the rest of my committee for the discussions that we have had and for their willingness to be on my committee.

I am very grateful for the patience and understanding that my wife and kids have shown throughout my PhD program; I could not have finished without their constant support and daily encouragement. I am also very thankful for the encouragement from my parents and my in-laws.

I am deeply grateful for all the divine inspiration that I have received; it is the only explanation for some of the roadblocks that I have been able to overcome.

I am very grateful to Scott A. Anderson and Chad Knight for all the SAR discussions we have had and the suggestions they have offered. I would also like to thank the countless others that have offered suggestions, advice, and ideas.

I am very grateful to the powers-that-be at the Space Dynamics Laboratory for granting the Tomorrow Fellowship to me; the financial assistance is another very important component that has made this dissertation possible.

Finally, I would like to thank Mary Lee Anderson for her guidance through all the required paperwork and for reviewing my dissertation for publication.

Roger D. West

Contents

Page

Abstract . . . . . **iii**

Acknowledgments . . . . . **vi**

List of Figures . . . . . **x**

Notation . . . . . **xiv**

Acronyms . . . . . **xv**

1 Introduction **1**
1.1 Introduction to SAR 1
1.2 Advantages of Model-Based SAR Processing 4
1.3 Contributions of this Dissertation 4
1.4 Outline of Dissertation 5

2 Radar Preliminaries **7**
2.1 Ideal Point Reflectors 7
2.2 Range Resolution 8
2.3 Pulsed LFM Transmitted Signals 9
2.4 Received Pulsed LFM Signal 10
2.5 Matched Filtering and Pulse Compression 13

3 Pulsed Synthetic Aperture Radar Preliminaries **19**
3.1 SAR Antenna 19
3.2 SAR Coordinate Frames 21
3.3 Induced Azimuth Signal 25
3.4 Bandwidth of the Induced Azimuth Signal 28
3.5 Pulse Transmission and Range Sampling 29
3.6 Model for the Range Sampled Data 29
3.7 SAR Image Formation 33
3.7.1 SAR Point-Spread Function 34
3.7.2 SAR Resolution 36

4 Pulsed LFM Stripmap Synthetic Aperture Radar **37**
4.1 Stripmap Geometry 37
4.2 Synthetic Aperture for Stripmap SAR 39
4.3 Induced Azimuth Signal for Stripmap SAR 41
4.4 Bandwidth of the Induced Azimuth Signal 42
4.5 Induced Discrete Doppler Signal for Pulsed LFM Stripmap SAR 50
4.6 Resolution Limits 52

4.7 Basic Steps for Image Formation 54
4.8 Image Formation Algorithms 56

5 Forward Model for Pulsed LFM Stripmap SAR 60
5.1 Forward Model for Stripmap SAR 60
5.1.1 Circularly Symmetric Additive White Gaussian Noise 63
5.1.2 Signal-to-Noise Ratio 65
5.2 Region of Interest 67
5.3 Summary 68

6 Maximum Likelihood Image Formation 69
6.1 Likelihood Function 69
6.2 Simulated Results 74
6.3 Cramér-Rao Lower Bound Analysis 78
6.4 Insights into the ML Estimation Method 79
6.5 Summary 82

7 Maximum *A Posteriori* Image Formation 83
7.1 *A Posteriori* Distribution 83
7.2 A More General Cost Function 84
7.3 Stripmap SAR Data Matrix 88
7.4 Block Recursive Least-Squares Algorithm for Stripmap SAR 91
7.4.1 Block RLS Algorithm Derivation 91
7.4.2 Block RLS Algorithm Results 95
7.5 Block Fast Array RLS Algorithm for Stripmap SAR 98
7.5.1 Block FARLS Algorithm Derivation 99
7.5.2 Block FARLS Algorithm Results 104
7.6 Comparison Between the BRLS and FARLS Methods 105
7.7 Summary 109

8 Model-Based Stripmap Autofocus 110
8.1 Background 110
8.2 Phase Error Model Development 112
8.2.1 Phase Error Free Model 112
8.2.2 Phase Error Model 113
8.3 Subspace Fitting Autofocus 114
8.3.1 Subspace Fitting Autofocus Derivation 115
8.3.2 Subspace Fitting Autofocus Optimization Strategy 117
8.4 Results of Proposed Autofocus Methods 122
8.4.1 Results Using Gradient Ascent 122
8.4.2 Results Using Regularized Newton's Method 122
8.4.3 Results Using Convex Optimization 123
8.5 Comparison of Optimization Strategies 123
8.5.1 Optimization Results 123
8.5.2 Comparison of Computational Complexity 132
8.6 Summary 133

9 Summary and Future Work 134
9.1 Summary 134
9.2 Future Work 137

References 139

Appendix 142
Appendix Circular and Hyperbolic Transformations 143
A.1 Traditional Circular and Hyperbolic Householder Transformations . 143
A.2 Block Circular and Hyperbolic Householder Transformations 145

Vita 151

List of Figures

Figure Page

2.1 Illustration of a baseband LFM signal with $T_p = 5 \times 10^{-6}$ sec, $\alpha = 7 \times 10^{11}$ Hz/sec^2, and $f_c = 0$. 10

2.2 Illustration of a simple pulsed LFM transmitter. 11

2.3 Illustration of the quadrature demodulation portion of the receiver for a pulsed LFM signal. 13

2.4 Illustration of the cases to consider for the convolution integral for the output of matched filtering. 15

2.5 Illustration of the real and imaginary parts and the autocorrelation of the window function for the output of the non-causal matched filter for a single reflector ($\sigma_1 = 1$). 17

2.6 Illustration of the magnitude and the autocorrelation of the window function for the output of the non-causal matched filter for a single reflector ($\sigma_1 = 1$). 17

3.1 Contour plot of the antenna power pattern with $L = 0.4$ m, $W = 0.2$ m, and $\lambda = 0.1$ m. 20

3.2 Illustration of inertial reference frame for SAR. 22

3.3 Illustration of the expanding wavefront from a transmitted pulse from an isotropic antenna. The bold blue contours are a two-dimensional slice of the spherical wavefronts and the red lines are the intersection between these wavefronts and the ground. 31

3.4 Illustration of the expanding wavefront from a transmitted pulse from a two-dimensional antenna array at a single instant in time. The bold blue line indicates the weighting of the reflectors along the red line. 32

3.5 Illustration of all of the ground region that contributes to $d(k, n)$ (the n^{th} sample of the received signal from the k^{th} pulse). 34

4.1 Illustration of stripmap SAR geometry. The sensor, moving with constant velocity in the x-direction, is at an altitude h in the z-direction and the main beam of the antenna makes a grazing angle ψ_0 with the plane containing the SAR sensor in the cross-track (range) y-direction. 38

4.2 Illustration of the synthetic aperture geometry for stripmap SAR (the perspective is from above). 40

4.3 Illustration of the changing range from a linear flight path past a stationary reflector. 43

4.4 Illustration of the relative velocity between the sensor and the stationary reflector with the parameters as given in the text. 43

4.5 Illustration of the Doppler shift in the received signal with the parameters as given in the text. 44

4.6 Illustration of the real part of the quadrature demodulated baseband signal with the parameters as given in the text. Note the similar appearance to a symmetric LFM signal. 44

4.7 Illustration of the actual induced Doppler shift for the parameters given in the text versus the LFM approximation. 48

4.8 Illustration of the signal induced with the antenna pattern and the signal induced with the isotropic antenna. Both signals include propagation loss. . 49

4.9 Illustration of the normalized spectrums of the signal induced with the antenna pattern and the signal induced with the isotropic antenna. The solid red vertical lines illustrate the bandwidth as defined in (4.35) and the dashed red lines indicate the traditionally used bandwidth. 49

4.10 Illustration of the matched filter outputs for the derived bandwidth and the traditionally used bandwidth. Notice that the matched filter output of the traditionally used bandwidth has two aliased peaks that are only -24 dB down from the main peak. 51

4.11 Illustration of the geometry for finding the ground range resolution from the slant range resolution. 54

4.12 Illustration of the real part of the PSR from a single ideal point reflector. . 57

4.13 Illustration of the (zoomed-in) real part of the data after being range compressed. 57

4.14 Illustration of "aligning" the data for azimuth compression. 58

4.15 Illustration of the focused reconstruction of the ideal point reflector. 58

5.1 Illustration of the power spectral density of a white noise process through each stage of the quadrature demodulator (including the A/D converter). . 66

5.2 Illustration of the concept of ROI, DOI, and ROIC for an arbitrary reconstruction grid. The ROI gives rise to the DOI, the DOI also contains data from the ROIC. 68

6.1 Illustration of the antenna beam pattern overlaying the image for the center pulse location. 75

6.2 Illustration of the magnitude of the baseband SAR data array for SNR $= \infty$ dB. 75

6.3 Illustration of the CBP image reconstruction for SNR $= \infty$ dB. 76

6.4 Illustration of the ML image reconstruction for SNR $= \infty$ dB. 76

6.5 Illustration of the ML image reconstruction for SNR $= 0$ dB. 77

6.6 Illustration of the ML image reconstruction for SNR $= 20$ dB. 77

6.7 Illustration of the ML image reconstruction for SNR $= 40$ dB. 78

6.8 Illustration of the CRLB for the simulation as stated above for SNR $= 40$ dB. 80

6.9 Illustration of the averaged (along azimuth) CRLB for each range for the ideal flight simulation as stated above for SNR $= 40$ dB. 80

6.10 Illustration of the absolute value of the elements of the grammian matrix. . 81

7.1 Illustration of the error (in dB) versus μ for $SNR = \infty$ dB. 89

7.2 Illustration of the error (in dB) versus μ for $SNR = 2$ dB. Notice the semi-convergence property. 89

7.3 Illustration of the ML image reconstruction (for comparison with the block RLS image reconstruction) for $SNR = 2$ dB. 96

7.4 Illustration of the block RLS image reconstruction for $SNR = 2$ dB. 96

7.5 Illustration of the ML image reconstruction (for comparison with the block RLS image reconstruction) for $SNR = 20$ dB. 97

7.6 Illustration of the block RLS image reconstruction for $SNR = 20$ dB. 97

7.7 Illustration of the ML image reconstruction (for comparison with the block FARLS image reconstruction) for $SNR = 2$ dB. 106

7.8 Illustration of the image reconstruction using the block FARLS for $SNR = 2$ dB. 106

7.9 Illustration of the pre-array on iteration 35. 107

7.10 Illustration of the post-array on iteration 35. 107

7.11 Illustration of the ML image reconstruction (for comparison with the block FARLS image reconstruction) for $SNR = 20$ dB. 108

7.12 Illustration of the image reconstruction using the block FARLS for $SNR = 20$ dB. 108

8.1 Illustration of the applied phase error. 124

8.2 Illustration of the original image. 124

8.3 CBP reconstruction without phase compensation. 125

8.4 ML reconstruction without phase compensation. 125

8.5 Top: Illustration of the gradient ascent method phase error estimates after $100,000$ iterations. Bottom: Illustration of the phase estimate error. 126

8.6 Illustration of the norm of the gradient versus iteration number. 126

8.7 CBP reconstruction after applying the phase estimates from the gradient ascent method. Compare to figure 8.3. 127

8.8 ML reconstruction after applying the phase estimates from the gradient ascent method. Compare to figure 8.4. 127

8.9 Top: Illustration of the regularized Newton method phase error estimates after $1,000$ iterations. Bottom: Illustration of the phase estimate error. . . 128

8.10 Illustration of the norm of the regularized Newton step versus iteration number. 128

8.11 CBP reconstruction after applying the phase estimates from the regularized Newton method. Compare to figure 8.3. 129

8.12 ML reconstruction after applying the phase estimates from the regularized Newton method. Compare to figure 8.4. 129

8.13 Top: Illustration of the linearized convex method phase error estimates after 500 iterations. Bottom: Illustration of the phase estimate error. 130

8.14 Illustration of the norm of the step taken each iteration versus iteration number for the linearized convex method. 130

8.15 CBP reconstruction after applying the phase estimates from the linearized convex method. Compare to figure 8.3. 131

8.16 ML reconstruction after applying the phase estimates from the linearized convex method. Compare to figure 8.4. 131

Notation

c	speed of light
f_c	carrier frequency
f_D	Doppler frequency
f_s	sampling rate of received signal
h	altitude of SAR sensor
L	length of antenna (azimuth)
N_a	number of azimuth cells in reconstructed image
N_d	number of sample delay associated with the range gate delay
N_k	number of pulses transmitted
N_n	number of samples collected from each transmitted pulse
N_r	number of range cells in reconstructed image
R_0	range from the sensor to where the antenna boresight hits the ground
R_n	range from the sensor to the n^{th} reflector
T	pulse repetition interval
T_p	transmitted pulse duration
T_s	sampling interval
W	width of antenna (elevation)
α	slope for a linear transmitted waveform
λ	wave-length of carrier frequency
σ_n	radar cross section of the n^{th} reflector
τ_n	round-trip delay from the sensor to the n^{th} reflector
ψ_0	antenna pointing direction with respect to the vehicle frame
θ_N	first-null beamwidth of antenna (azimuth)
ϕ_N	first-null beamwidth of antenna (elevation)

Acronyms

AWGN	additive white Gaussian noise
BFARLS	block fast array recursive least squares
BRLS	block recursive least squares
CBP	convolution back-projection
CRLB	Cramér-Rao lower bound
DEM	digital elevation model
DOI	data of interest
FFT	fast Fourier transform
GMTI	ground moving target indication
GPS	global positioning system
IMU	inertial measurement unit
IPI	inter-pixel interference
LFM	linear frequency modulation
LPF	low-pass filter
MAP	maximum *a posteriori*
ML	maximum likelihood
PRI	pulse repetition interval
PRF	pulse repetition frequency
RCMC	range cell migration correction
RCS	radar cross section
ROI	region of interest
ROIC	region of interest closure
RGD	range gate delay
SAR	synthetic aperture radar
SNR	signal-to-noise ratio

Chapter 1

Introduction

This chapter gives an introduction to synthetic aperture radar (SAR) and explains some of its uses. It is also explained that there are different modes of SAR imaging, such as stripmap SAR and spotlight SAR. A brief survey of different SAR image formation methods are explained and some of the issues that prevent a well-focused SAR image are also explained. One source of image artifact that is common in SAR images is the inter-pixel interference (IPI) of the processing algorithm. This chapter also explains that the IPI that is present in the commonly-used SAR image formation methods can be accounted for and removed with model-based SAR image formation methods.

This chapter concludes by stating the major contributions this dissertation makes to stripmap SAR and gives an outline of the contents of this dissertation.

1.1 Introduction to SAR

Synthetic aperture radar (SAR) is a remote sensor that provides its own illumination, which makes it an active remote sensor (as opposed to a passive remote sensor which relies on the reflected illumination from some naturally incident source in the scene being observed). The illumination that a SAR sensor provides is a transmitted radio-wave signal centered about a chosen carrier frequency.

A SAR sensor can produce a high resolution image of ground reflectivity that looks similar to an optical image. However, the information content of a SAR image is different than what is in an image at the visible spectrum. What a SAR sensor measures is the reflectivity of a scene at a particular wavelength of the electromagnetic spectrum. Some objects, such as lakes and rivers, that are very apparent in an optical images may be virtually invisible in SAR images, and vice versa.

There are many applications for SAR sensors. With a properly selected carrier frequency, a SAR sensor can penetrate foliage or dry sand to image scenes beneath the canopy of a forest or measure the sand layer thickness in deserts [1, 2]. Since SAR sensors provide their own illumination, they can be used to image the ground at night. Properly equipped SAR sensors can identify motion in a scene [3] or measure ground elevation (topography) [4]. A SAR sensor can be flown over a scene at different times to measure such things as the changes in the terrain elevation after an earthquake [5].

SAR sensors are usually flown on either a satellite or an airplane. There are also different modes in which a SAR sensor can be used. The two most common modes are spotlight SAR (where the antenna is gimbaled to always point at the same spot on the ground as the platform moves) and stripmap SAR (where the antenna is fixed to the side of the vehicle and the path of the antenna beam traces a strip on the ground as the platform moves). There are also different types of SAR sensors such as continuous wave (continuously transmitting) or pulsed (transmit a signal at equally spaced time intervals). Processing SAR data to form a focused image is dependent on the vehicle the sensor is mounted to and the choice of the SAR mode and type.

A SAR sensor obtains its high resolution in range from pulse compression techniques well known in the radar literature [6–8]. How SAR obtains its high azimuth resolution is what differentiates it from traditional radar systems. It is well known in antenna theory [9] that to obtain good resolvability in the direction of interest with an antenna, the antenna must have a narrow beamwidth (in SAR this direction is the cross-range or azimuth direction). With carrier frequencies typically used for SAR sensors, the size of the antenna to produce this narrow beamwidth for the resolution that is desired is prohibitively large. The way a SAR sensor achieves its high azimuth resolution is by synthesizing a larger antenna array by transmitting and receiving at locations where the antenna elements of the required (much larger) antenna aperture would have been and combining the collected data in an appropriate manner. Hence the name *synthetic* aperture radar.

In order for the collected data to be combined correctly, the phase of the carrier frequency at each pulsing instant and the phase of the received signal must be known, hence SAR systems are coherent systems. Embedded in the collected data are azimuth phase signals, constructed from the phase of the carrier, that can be compressed using matched filtering. The compression of these azimuth signals is what gives SAR its high azimuth resolution. If the phase is not known, or if the incorrect phase is used, the image that is formed will be out of focus (perhaps to the point of not even being usable).

One of the big challenges of producing a well focused SAR image is the azimuth focusing. The azimuth focusing is also accomplished by matched filtering and is very sensitive to phase errors. The phase errors that corrupt the azimuth matched filtering stem from unaccounted motion of the sensor, incorrect digital elevation models (DEM), and signal propagation effects. By using a global positioning system (GPS) and an inertial measurement unit (IMU), the motion and attitude of the sensor can be tracked to a fairly high level of accuracy. Motion compensation algorithms exist that use the GPS and IMU data to help correct for most of the known flight path deviations. However, the data from GPS and IMU are not perfect, thus residual phase errors may still exist. These residual phase errors, along with the phase errors from incorrect DEMs and signal propagation effects, will blur a SAR image. Data driven algorithms, known as autofocus algorithms, correct these phase errors and can greatly improve the focusing of a blurred SAR image.

The traditional algorithms that are used to focus SAR data fall into either time-domain methods or frequency-domain methods. The frequency-domain methods are very efficient because they utilize efficient fast Fourier transform (FFT) algorithms in their processing. However, there are many assumptions that go along with using FFT methods, such as transmitting a pulse at equally spaced locations and having an ideal flight (no deviation from a linear path). If these assumptions do not hold, then the frequency-domain methods produce blurred SAR images. The time-domain methods are more computationally intensive than the frequency-domain methods, but such things as motion errors and DEMs are easily taken into account. Thus, the time-domain methods typically produce better focused

images than frequency-domain methods, at the cost of computation.

Both the time and frequency domain methods are essentially different ways (with different assumptions) of implementing a two-dimensional matched filter or two-dimensional correlation. One artifact that will be referred to as inter-pixel interference (IPI) that is inherent in images produced by either method is the bright, star-like patterns around strong reflectors in a processed image. IPI is actually an artifact of all correlation-based methods, thus is exists about each reflector in the image, though it is usually more noticeable around strong reflectors. IPI can make it difficult to analyze what is actually in the image because the IPI around strong reflectors masks weaker reflectors.

1.2 Advantages of Model-Based SAR Processing

Fairly recently, a new class of "inverse problems" methods has been introduced for spotlight SAR [10, 11]. These methods derive the forward model of the spotlight SAR data acquisition, then invert the model to form an image. These methods can produce the best spotlight SAR images at the cost of higher computational complexity. Model-based methods are capable of achieving higher quality SAR images by including as many real effects as possible in the model and by providing a mathematically principled approach to solving for the parameters of interest. In SAR, these parameters are the ground reflectivity. Among the effects that can be modeled is the IPI. Thus, upon system inversion, the IPI can be removed, resulting in an image that is much easier to analyze.

Currently, there is not an explicit forward model for stripmap SAR that accounts for a generic pulsed signal, an arbitrary antenna beam pattern, that can account for arbitrary flight paths and sensor attitude angles, and that can model arbitrary additive noise.

1.3 Contributions of this Dissertation

The first contribution to stripmap SAR in this dissertation is the development of a comprehensive linear forward model for the data collected from stripmap SAR. Although a pulsed linear frequency modulated (LFM) signal is used throughout this dissertation, the model allows for an arbitrary pulsed signal to be used. The model also allows for the

antenna beam pattern to be modeled, it allows for arbitrary flight paths, and it also allows for arbitrary additive noise to be modeled.

Due to the additive noise in the forward model, the collected data also has a statistical interpretation. Based on this statistical interpretation of the forward model, the second contribution is the development of the maximum likelihood (ML) image formation method. The ML method has two steps. It is shown that the first step is equivalent to the convolution back projection (CBP) algorithm which is a time-domain image formation method, and the second step removes the IPI in the image.

The third contribution is the development of two maximum *a posteriori* (MAP) image formation methods. It is shown that if the noise is additive white Gaussian noise (AWGN) and the prior probabilities of the ground reflectivity are Gaussian, then the MAP methods have a close connection to regularized least squares algorithms. Under these assumptions, it is shown that a novel application of the block recursive least squares (BRLS) algorithm is to form a MAP stripmap SAR image. Furthermore, if an ideal stripmap flight is flown, then there is structure in the stripmap SAR data collection process. This structure allows a new block fast array RLS (BFARLS) algorithm to be used to form a MAP image. The BFARLS requires a block hyperbolic transformation and while it is not a direct contribution to stripmap SAR, the block hyperbolic transformation that is developed is still interesting in its own right.

The final contribution is the development of a model-based autofocus algorithm for stripmap SAR. Based on the linear forward model, it is shown that estimating the phase error is a constrained subspace fitting problem. It is shown that the phase error can be estimated and applied to correct the image without iterating between the image and data domain.

1.4 Outline of Dissertation

The outline of this dissertation is as follows. Chapter 2 introduces the concepts of range resolution and pulse compression (matched filtering) from radar theory that will be needed in the development of SAR. Chapter 3 introduces some basic concepts for generic

pulsed SAR systems. Chapter 4 covers the important concepts for a pulsed stripmap SAR system. The concepts and equations in Chapters 2-4 form the foundation of the forward model for stripmap SAR and are also used to build the SAR simulator that is used to test the proposed algorithms.

The forward model is developed in Chapter 5. Based on the forward model, Chapter 6 derives the ML image formation method and Chapter 7 derives the MAP image formation methods. Chapter 8 extends the forward model to account for phase corrupted data and derives a model-based autofocus algorithm. The new autofocus algorithm is a constrained subspace fitting problem and methods are derived for solving for the phase estimates.

The conclusion of this dissertation and the future work in model-based stripmap SAR are presented in Chapter 9. Finally, the Appendix covers the block hyperbolic transformations that are needed in the BFARLS algorithm.

Chapter 2

Radar Preliminaries

This chapter briefly introduces some topics from radar systems that are common to both radar and SAR systems that we will need throughout this dissertation. Although there is not anything new being contributed to the field in this chapter, the content lays the groundwork for the development in the remainder of this dissertation. Ideal point reflectors are described in this chapter. Range resolution is described, which is the ability to distinguish between reflectors in the range direction. The linear frequency modulated (LFM) waveform is discussed and a simple block diagram is given for generating a pulsed LFM signal. The receiver for quadrature demodulating a pulsed LFM signal is also discussed and is illustrated in a simple block diagram. Finally, the matched filter in the receiver is also discussed. Range compressing the reflected signal has the effect of greatly improving the range resolution of a radar system.

2.1 Ideal Point Reflectors

The reflectivity of an object is a function of many different parameters: the geometry of the object, the size of the object (relative to wavelength), and the angle of incidence, just to name a few. The reflectivity of an isolated object in free-space with no background reflectivity (or with the background much less reflective than the object) is called the radar cross section (RCS). In imaging radar the reflectivity of a scene is measured and a pixel in the reconstructed image represents a patch of ground. The patch of ground is an aggregate of smaller reflectors that are too closely space to be resolvable by the radar imaging system. In this case, it is not correct to interpret the results as RCS, but as an average RCS. Some radar literature refers to the average RCS as scattering brightness [12].

The term ideal point reflector will be used in this dissertation to describe a reflector

that has unit reflectivity from any angle of incidence (isotropic) and that is independent of wavelength over the bandwidth of interest (non-dispersive) [12]. In this dissertation, it will be assumed that these ideal reflectors are on the ground and that they are much more reflective than the ambient background. Also, the term reflector will be used interchangeably with ideal point reflector.

2.2 Range Resolution

Being able to resolve multiple reflectors in range is very important to a radar system. Range resolution is defined as the ability to distinguish between two separate but closely spaced reflectors in range. Similar discussions on range resolution can be found in the radar literature [6, 13].

Consider a monostatic radar system that transmits and receives a single pulsed signal. Let the transmitted pulse (denoted $s(t)$) have duration T_p seconds. For a discrete set of ideal reflectors, the reflected signal will have the form (neglecting antenna pattern, propagation loss, and noise)

$$r(t) = \sum_{n=1}^{N} \sigma_n s(t - \tau_n), \tag{2.1}$$

where σ_n denotes the radar cross section (RCS) of the n^{th} ideal reflector and τ_n denotes the round-trip delay from the radar system to the n^{th} reflector. The round-trip delay to the n^{th} reflector and the range from the n^{th} reflector to the radar are related by

$$\tau_n = \frac{2}{c} R_n, \tag{2.2}$$

where R_n is the range from the radar to the n^{th} reflector.

It is clear that if the reflectors are separated in time by greater than $T_p/2$ seconds in the direction of the propagation of the signal (this accounts for the round-trip of the signal) that each signal reflected from a reflector will not be overlapped by its neighbor and therefore the number of reflectors (and their distance from the radar) can be easily resolved.

Converting this to range by multiplying by c gives the range resolution as

$$\Delta R = \frac{c}{2} T_p. \tag{2.3}$$

As an illustration, if a transmitted pulse has duration 1×10^{-6} seconds (let $c = 3 \times 10^8$), then the reflectors are resolvable if they are 150 meters apart. The pulse duration could always be shortened to improve range resolution, however to maintain the same signal-to-noise ratio (SNR) the transmitted power would need to be increased, also the bandwidth would increase. It will be shown below that the range resolution can be increased by using pulse compression.

2.3 Pulsed LFM Transmitted Signals

One of the most popular transmitted signals in radar systems is the pulsed linear frequency modulated (LFM) waveform, sometimes referred to as a chirp signal [13, 14]. There are many reasons for using the LFM waveform. One reason is that it has good pulse compression properties. The LFM signal is the signal that will be used throughout this dissertation unless otherwise specified.

A single LFM pulse with a duration of T_p seconds is given by the equation

$$\begin{aligned} s(t) &= \Re\left\{ w(t) e^{j2\pi\left(f_c t + \frac{\alpha}{2} t^2\right)} \right\} && (2.4) \\ &= w(t) \cos\left(2\pi f_c t + \pi \alpha t^2\right) && (2.5) \end{aligned}$$

where α is the linear frequency rate and $w(t)$ is the window function, defined as

$$w(t) = \begin{cases} 1, & 0 \le t \le T_p, \\ 0, & \text{otherwise.} \end{cases} \tag{2.6}$$

An example of a baseband ($f_c = 0$) pulsed LFM signal is illustrated in figure 2.1. The window function is overlaid on top of the pulse $s(t)$. The radar transmits many of these pulses that are separated in time by T seconds. T is known as the pulse repetition interval

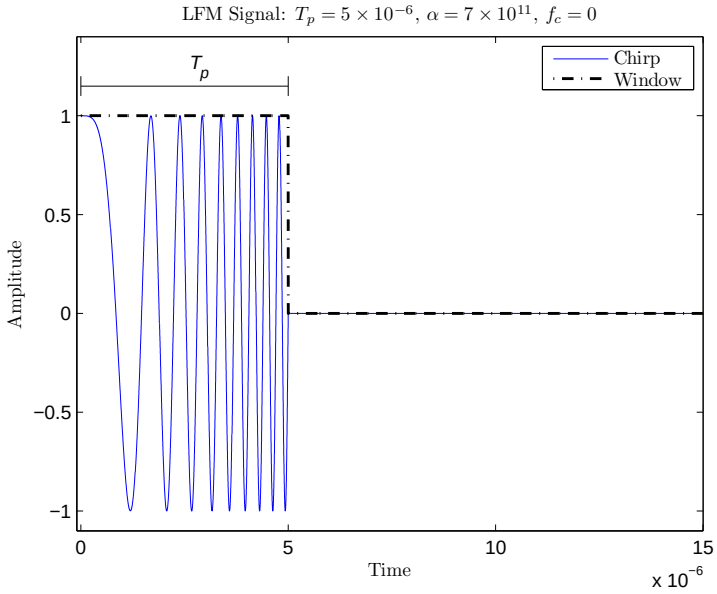

Fig. 2.1: Illustration of a baseband LFM signal with $T_p = 5 \times 10^{-6}$ sec, $\alpha = 7 \times 10^{11}$ Hz/sec^2, and $f_c = 0$.

(PRI) and the reciprocal of T is called the pulse repetition frequency (PRF). The signal model for transmitting successive pulses is given by

$$s(t) = \sum_k w(t - kT) \cos\left(2\pi f_c(t - kT) + \pi\alpha(t - kT)^2 + \psi_k\right), \tag{2.7}$$

where $\psi_k = 2\pi f_c T k$ is the phase of the carrier frequency at the instant of the k^{th} pulse. A simple block diagram for a pulsed LFM system is illustrated in figure 2.2. In figure 2.2, the time variable is t and has limits $-\infty < t < \infty$; the notation $((t))_T$ is time modulo T so that $((t))_T$ falls in the interval $0 \leq ((t))_T \leq T$.

2.4 Received Pulsed LFM Signal

Consider a stationary monostatic radar system located at $\mathbf{x}$ and a stationary reflector located at $\mathbf{u}$. Because both are stationary, there is no Doppler shift in the reflected signal, and using the same assumptions, the received signal has the same form as in (2.1). Suppose

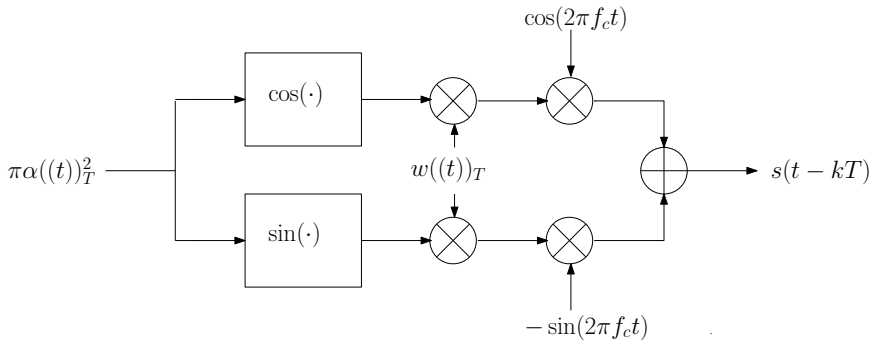

Fig. 2.2: Illustration of a simple pulsed LFM transmitter.

the transmitted LFM signal

$$s(t) = w(t)\cos\left(2\pi f_c t + \pi\alpha t^2\right) \tag{2.8}$$

is reflected from a single reflector. The received signal has the form

$$r(t) = \sigma_1 w(t-\tau_1)\cos\left(2\pi f_c(t-\tau_1) + \pi\alpha(t-\tau_1)^2\right). \tag{2.9}$$

The received signal is obviously still at the carrier frequency (the received signal is also bandpass filtered for practical reasons) and because the time delay to the reflector is embedded in the phase, a quadrature demodulator is used to demodulate the received signal so that the phase can be recovered [6,13]. The signal in the in-phase branch of the demodulator is multiplied by $\cos(2\pi f_c t)$

$$\begin{aligned} r_I(t) &= r(t)\cos(2\pi f_c t) && (2.10)\\ &= \sigma_1 w(t-\tau_1)\cos\left(2\pi f_c(t-\tau_1) + \pi\alpha(t-\tau_1)^2\right)\cos(2\pi f_c t). && (2.11) \end{aligned}$$

Using the trigonometric identity

$$\cos(A)\cos(B) = \frac{1}{2}(\cos(A+B) + \cos(A-B)), \tag{2.12}$$

the in-phase branch signal is

$$r_I(t) = \frac{\sigma_1}{2}[w(t-\tau_1)\cos\left(2\pi(2t-\tau_1)+\pi\alpha(t-\tau_1)^2\right) \tag{2.13}$$

$$+\cos\left(-2\pi f_c\tau_1+\pi\alpha(t-\tau_1)^2\right)]. \tag{2.14}$$

Similarly, the quadrature branch is multiplied by $-\sin(2\pi f_c t)$

$$r_Q(t) = \frac{\sigma_1}{2}w(t-\tau_1)[-\sin\left(2\pi(2t-\tau_1)+\pi\alpha(t-\tau_1)^2\right) \tag{2.15}$$

$$+\sin\left(-2\pi f_c\tau_1+\pi\alpha(t-\tau_1)^2\right)], \tag{2.16}$$

where the trigonometric identity

$$\cos(A)\sin(B) = \frac{1}{2}(\sin(A+B)-\sin(A-B)) \tag{2.17}$$

is used. Both branches have a term that is twice the carrier frequency and a baseband term. Low-pass filtering (assume the LPF has a gain of two to get rid of the fractions) each branch removes the double frequency term and passes the baseband term, giving

$$r_{I,LPF}(t) = \sigma_1 w(t-\tau_1)\cos\left(-2\pi f_c\tau_1+\pi\alpha(t-\tau_1)^2\right) \tag{2.18}$$

$$r_{Q,LPF}(t) = \sigma_1 w(t-\tau_1)\sin\left(-2\pi f_c\tau_1+\pi\alpha(t-\tau_1)^2\right). \tag{2.19}$$

It is convenient at this point to sample both branches at $t = nT_s$ and create a complex signal by adding the in-phase branch to j times the quadrature branch. However, for this derivation, the development will continue with continuous time signals and the connection to sampled signals will be made at the end of the derivation. Adding the continuous-time in-phase signal to j times the continuous-time quadrature signal gives

$$r_C(t) = \sigma_1 w(t-\tau_1)e^{j\left(-2\pi f_c\tau_1+\pi\alpha(t-\tau_1)^2\right)} \tag{2.20}$$

$$= \sigma_1 w(t-\tau_1)e^{-j\left(2\pi f_c\tau_1-\pi\alpha(t-\tau_1)^2\right)}. \tag{2.21}$$

Up to this point, the signal has been brought to baseband; the time delay to the reflector has not been recovered. A block diagram of these signal operations is illustrated in figure 2.3. It is clear from (2.21) that if there is only one reflector in the radar beam then the delay to the single reflector could be obtained by just noting when the reflected signal is present at the receiver. The effective time duration of the signal in the receiver is T_p seconds, hence nothing has been done to improve the range resolution. However, the pulsed LFM signal has good pulse compression properties and, as will be shown, after pulse compression the effective time duration of the compressed signal is greatly reduced from T_p, and therefore much better range resolution is possible.

2.5 Matched Filtering and Pulse Compression

A matched filter is used to compress a pulsed LFM signal, the output of the matched filter gives greatly improved resolution. The following development is common in the radar literature [13, 14]. Let the matched filter be given as

$$h_{MF}(t) = w(-t)e^{-j\left(\pi\alpha(-t)^2\right)}, \tag{2.22}$$

which is a time reversed and conjugated version of the transmitted signal with the carrier removed. Let $*$ denote the convolution operator, then the output of the matched filter is

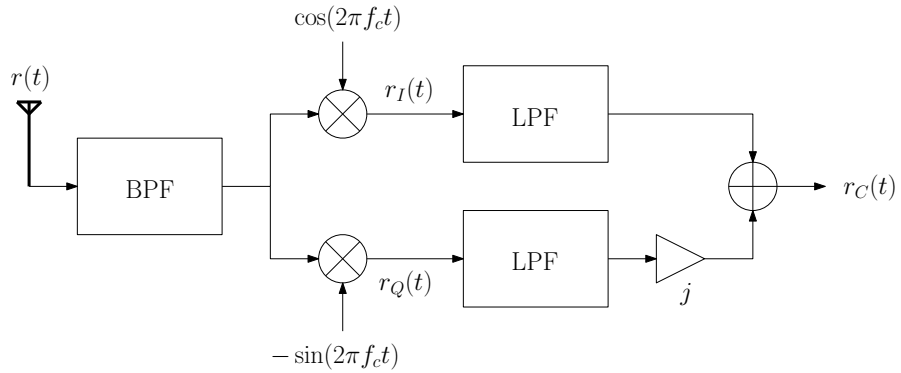

Fig. 2.3: Illustration of the quadrature demodulation portion of the receiver for a pulsed LFM signal.

given as

$$\begin{aligned} r_{MF}(t) &= r_C(t) * h_{MF}(t) && (2.23)\\ &= \int_{-\infty}^{\infty} r_C(\lambda) h_{MF}(t-\lambda) d\lambda && (2.24)\\ &= \sigma_1 \int_{-\infty}^{\infty} w(\lambda-\tau_1) e^{-j\left(2\pi f_c \tau_1 - \pi\alpha(\lambda-\tau_1)^2\right)} w(\lambda-t) e^{-j\left(\pi\alpha(\lambda-t)^2\right)} d\lambda. && (2.25) \end{aligned}$$

Let $\rho = \lambda - \tau_1$, thus $\lambda = \rho + \tau_1$ and $d\rho = d\lambda$. Using this change of variables gives

$$\begin{aligned} r_{MF}(t) &= \sigma_1 \int_{-\infty}^{\infty} w(\rho) e^{-j\left(2\pi f_c \tau_1 - \pi\alpha\rho^2\right)} w(\rho-(t-\tau_1)) e^{-j\left(\pi\alpha(\rho-(t-\tau_1))^2\right)} d\rho && (2.26)\\ &= \sigma_1 e^{-j2\pi f_c\tau_1} e^{-j\pi\alpha(t-\tau_1)^2} \int_{-\infty}^{\infty} w(\rho) w(\rho-(t-\tau_1)) e^{j2\pi\alpha(t-\tau_1)\rho} d\rho, && (2.27) \end{aligned}$$

where the second term comes from expanding the square, canceling terms, and factoring out terms from the integral that are not dependent on ρ. From the definition of the window function given in (2.6), the limits on ρ are

$$w(\rho) = \begin{cases} 1, & 0 \le \rho \le T_p, \\ 0, & \text{otherwise}, \end{cases} \tag{2.28}$$

$$w(\rho-(t-\tau_1)) = \begin{cases} 1, & t-\tau_1 \le \rho \le t-\tau_1+T_p, \\ 0, & \text{otherwise}, \end{cases} \tag{2.29}$$

thus there are two cases to consider for the limits of the convolution integral as illustrated in figure 2.4. Consider the first case where $t < \tau_1$. Let $\gamma = t - \tau_1$, then the integral becomes

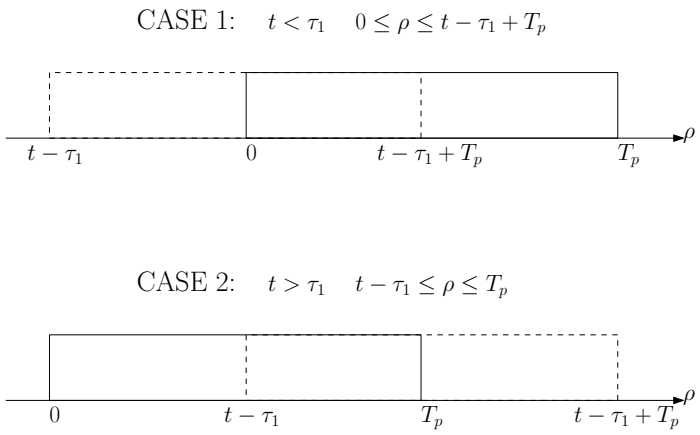

Fig. 2.4: Illustration of the cases to consider for the convolution integral for the output of matched filtering.

$$
\begin{aligned}
r_{MF}(t) &= \sigma_1 e^{-j2\pi f_c \tau_1} e^{-j\pi\alpha\gamma^2} \int_0^{\gamma+T_p} e^{j2\pi\alpha\gamma\rho} d\rho && (2.30)\\
&= \sigma_1 e^{-j2\pi f_c \tau_1} e^{-j\pi\alpha\gamma^2} \left(\frac{1}{j2\pi\alpha\gamma} \left[e^{j2\pi\alpha\gamma(\gamma+T_p)} - 1 \right] \right) && (2.31)\\
&= \sigma_1 e^{-j2\pi f_c \tau_1} e^{-j\pi\alpha\gamma^2} \left(\frac{1}{\pi\alpha\gamma} \frac{\left[e^{j\pi\alpha\gamma(\gamma+T_p)} - e^{-j2\pi\alpha\gamma(\gamma+T_p)} \right]}{j2} e^{j\pi\alpha\gamma(\gamma+T_p)} \right) && (2.32)\\
&= \sigma_1 e^{-j2\pi f_c \tau_1} e^{j\pi\alpha T_p\gamma} \left(\frac{\sin(\pi\alpha\gamma(T_p+\gamma))}{\pi\alpha\gamma} \right). && (2.33)
\end{aligned}
$$

Now, consider the second case where $t > \tau_1$. Again, let $\gamma = t - \tau_1$, then the integral becomes

$$
\begin{aligned}
r_{MF}(t) &= \sigma_1 e^{-j2\pi f_c \tau_1} e^{-j\pi\alpha\gamma^2} \int_\gamma^{T_p} e^{j2\pi\alpha\gamma\rho} d\rho && (2.34)\\
&= \sigma_1 e^{-j2\pi f_c \tau_1} e^{-j\pi\alpha\gamma^2} \left(\frac{1}{j2\pi\alpha\gamma} \left[e^{j2\pi\alpha\gamma T_p} - e^{j2\pi\alpha\gamma^2} \right] \right) && (2.35)\\
&= \sigma_1 e^{-j2\pi f_c \tau_1} e^{j\pi\alpha T_p\gamma} \left(\frac{1}{\pi\alpha\gamma} \frac{\left[e^{j\pi\alpha\gamma(T_p-\gamma)} - e^{-j\pi\alpha\gamma(T_p-\gamma)} \right]}{j2} \right) && (2.36)\\
&= \sigma_1 e^{-j2\pi f_c \tau_1} e^{j\pi\alpha T_p\gamma} \left(\frac{\sin(\pi\alpha\gamma(T_p-\gamma))}{\pi\alpha\gamma} \right). && (2.37)
\end{aligned}
$$

In the second step, the relationship

$$
e^A - e^B = \left(e^{\frac{A-B}{2}} - e^{-\frac{A-B}{2}} \right) e^{\frac{A+B}{2}} \qquad (2.38)
$$

is used.

Notice that in the first case, $\gamma < 0$ and in the second case $\gamma > 0$. Using this, the two cases can be combined into the single equation

$$r_{MF}(t) = \sigma_1 e^{-j2\pi f_c \tau_1} e^{j\pi\alpha T_p \gamma} \left(\frac{\sin(\pi\alpha\gamma(T_p - |\gamma|))}{\pi\alpha\gamma} \right). \tag{2.39}$$

Substituting in $\gamma = t - \tau_1$ gives the final equation for the matched filter output

$$r_{MF}(t) = \sigma_1 e^{-j2\pi f_c \tau_1} e^{j\pi\alpha T_p (t-\tau_1)} \left(\frac{\sin(\pi\alpha(t-\tau_1)(T_p - |t-\tau_1|))}{\pi\alpha(t-\tau_1)} \right). \tag{2.40}$$

From the limits of integration, the equation for the matched filter output (2.40) is valid for the time interval $-T_p \leq t \leq T_p$ and is zero outside this interval. A plot of the real and imaginary parts of this signal along with the envelope generated by the autocorrelation of the window function is illustrated in figure 2.5 for a reflector with $\sigma_1 = 1$ and $\tau_1 = 15 \times 10^{-6}$ seconds. The magnitude of the matched filter output is illustrated in figure 2.6. Notice at the time instant $t = \tau_1$ that the equation reduces to

$$r_{MF}(\tau_1) = \sigma_1 e^{-j2\pi f_c \tau_1} T_p, \tag{2.41}$$

from which σ_1 and τ_1 can be extracted. In general σ_1 will be a complex number which will alter the phase.

This derivation for the output of the matched filter used a non-causal matched filter. In practice, a causal matched filter is employed. To make the matched filter causal, it must be delayed by T_p seconds. Thus, using

$$h_{MF}(t) = w(T_p - t) e^{j\pi\alpha(T_p - t)^2} \tag{2.42}$$

as the matched filter will produce the matched filter output

$$r_{MF}(t) = \sigma_1 e^{-j2\pi f_c \tau_1} e^{j\pi\alpha T_p (t-\tau_1-T_p)} \left(\frac{\sin(\pi\alpha(t-\tau_1-T_p)(T_p - |t-\tau_1-T_p|))}{\pi\alpha(t-\tau_1-T_p)} \right). \tag{2.43}$$

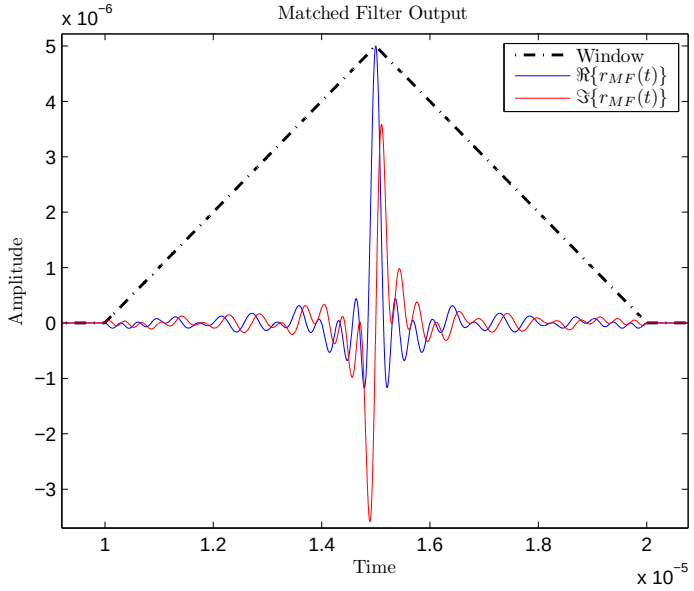

Fig. 2.5: Illustration of the real and imaginary parts and the autocorrelation of the window function for the output of the non-causal matched filter for a single reflector ($\sigma_1 = 1$).

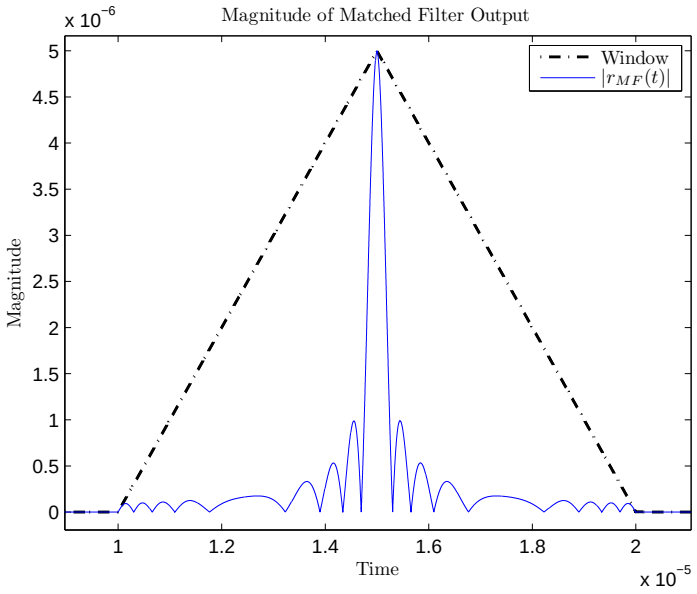

Fig. 2.6: Illustration of the magnitude and the autocorrelation of the window function for the output of the non-causal matched filter for a single reflector ($\sigma_1 = 1$).

The output of the causal matched filter at $t = \tau_1 + T_p$ gives the same result as the output of the non-causal matched filter at $t = \tau_1$.

As discussed above, the range resolution without any processing is determined by the duration of the transmitted pulse, T_p. Let T_p' denote the time duration of the main peak of the matched filter output. Using T_p' as the new pulse duration, the range resolution is now

$$\Delta R' = \frac{c}{2} T_p'. \tag{2.44}$$

As an example, take $T_p = 5 \times 10^{-6}$ seconds (as illustrated in figure 2.1). Computing the time duration of the main peak of the matched filter output from either (2.40) or (2.43) gives $T_p' = 6.0844 \times 10^{-7}$ seconds. Thus $\Delta R = 750$ meters and $\Delta R' = 91.266$ meters. This is an improvement of over a factor of eight. Typical improvements for SAR systems are factors on the order of $1,000$ [15].

Chapter 3

Pulsed Synthetic Aperture Radar Preliminaries

This chapter introduces several elements of SAR that are common to most modalities. Although no significant contribution is being made to SAR in this chapter, the development here provides the necessary foundation for the forward model for stripmap SAR. Also many of the concepts in this chapter are needed to create a SAR simulator. The antenna that will be used throughout this dissertation is introduced. Coordinate frames for the vehicle, antenna, and an inertial reference are also introduced to help describe SAR geometry and the antenna pointing direction. The induced azimuth signal that forms the basis for SAR is derived and the bandwidth of this signal is discussed. It is also explained that one of the factors that determines the pulse repetition frequency (PRF) for pulsed SAR systems is the bandwidth of this induced signal. A model for the data contained in each range sample is also derived. Finally, some concepts that pertain to image formation such as the SAR point-spread function and SAR resolution are briefly discussed. More will be said on these when a specific SAR modality is chosen.

3.1 SAR Antenna

One of the most critical elements of SAR is the antenna. Therefore, we must first briefly describe the antenna that will be referenced throughout this chapter and dissertation.

The antenna that will be used throughout this dissertation is a uniformly weighted rectangular two-dimensional array of half-wave dipoles. Two important physical parameters of this antenna are its length and width (denoted as L and W, respectively). An equation that approximately describes the power pattern of this antenna is [13]

$$a(\phi,\theta) = \left(\frac{\sin\left(\pi \frac{L}{\lambda}\sin(\theta)\right)\sin\left(\pi \frac{W}{\lambda}\sin(\phi)\right)}{\left(\pi \frac{L}{\lambda}\sin(\theta)\right)\left(\pi \frac{W}{\lambda}\sin(\phi)\right)} \right)^2, \tag{3.1}$$

where λ is the wavelength of the center frequency being transmitted from the antenna and θ and ϕ are the azimuth and elevation angles, repectively, and are measured from the boresight of the antenna. The boresight of the antenna is said to be pointing in the direction of the peak of the power pattern. This power pattern is essentially a squared, two-dimensional, 2π-periodic, sinc-like function. Figure 3.1 shows a contour plot of the power pattern with $L = 0.4$ m, $W = 0.2$ m, and $\lambda = 0.1$ m for $-90^\circ \leq \phi \leq 90^\circ$ and $-90^\circ \leq \theta \leq 90^\circ$. This antenna also has another mainlobe at $\phi = \theta = 180^\circ$. For the sake of using this simplified model, it will be assumed that this other mainlobe is suppressed by a back-wave absorber.

Some other important parameters for this antenna are the first null beam widths (the angle between the first nulls on either side of the mainlobe), the half-power beam widths (the angle between the first points that are 3 dB down from the peak of the mainlobe) in both the azimuth and elevation directions, and the effective area. Denote the first-null beam width in azimuth by ϑ_N and in elevation by φ_N. The angle ϑ_N can be found by setting $\theta = \vartheta_N$ in (3.1) and solving (3.1) equal to zero for ϑ_N. The angle φ_N can be found similarly. If $\lambda << L$ and $\lambda << W$, then the antenna narrow beam assumption and the

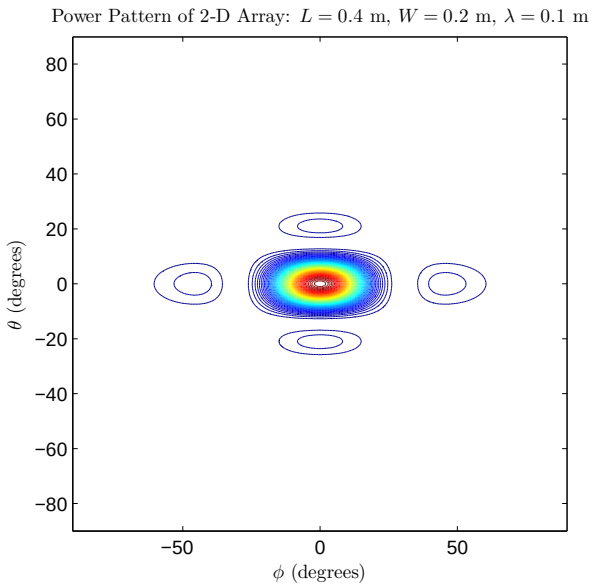

Fig. 3.1: Contour plot of the antenna power pattern with $L = 0.4$ m, $W = 0.2$ m, and $\lambda = 0.1$ m.

small angle approximation, $\sin(x) \approx x$, can be used giving [9, 13]

$$\vartheta_N \approx \frac{2\lambda}{L} \tag{3.2}$$

$$\varphi_N \approx \frac{2\lambda}{W}. \tag{3.3}$$

Let ϑ_{3dB} denote the half-power beam width in azimuth and φ_{3dB} denote the half-power beam width in elevation. Using the antenna narrow beam assumption, an approximate way to compute their values is [13]

$$\vartheta_{3dB} \approx \frac{\lambda}{L}, \tag{3.4}$$

$$\varphi_{3dB} \approx \frac{\lambda}{W}. \tag{3.5}$$

Let A_e denote the effective area of the antenna. The effective area is computed as the product of the length and width of the antenna array

$$A_e = LW \approx \frac{\lambda^2}{\vartheta_{3dB}\varphi_{3dB}} \tag{3.6}$$

3.2 SAR Coordinate Frames

It is helpful to introduce some coordinate frames to help fully describe the geometry of SAR and the antenna pointing direction. For the sake of defining a (relatively) inertial frame for the scene to be imaged, assume that the scene to be imaged is flat and rectangular and that the antenna is mounted on the pilot's left hand side of the vehicle. Let the origin of the inertial reference frame be located on the ground, half-way up the azimuth direction of the scene to be imaged, and on the side of the image closest to the path of the sensor. Then, define the orthogonal coordinate frame by the following unit vectors: $\mathbf{i}_1^i$ points in the cross-range (azimuth) direction, $\mathbf{i}_2^i$ points in the range direction, and $\mathbf{i}_3^i = \mathbf{i}_1^i \times \mathbf{i}_2^i$ points up. This frame is illustrated in figure 3.2.

To define the coordinate frame for the vehicle, let the origin be the center of mass, then define the orthogonal coordinate frame by the following unit vectors: $\mathbf{v}_1^v$ points in the

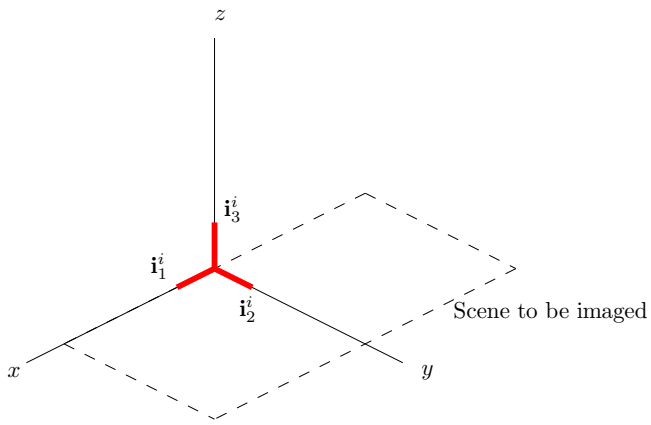

Fig. 3.2: Illustration of inertial reference frame for SAR.

direction out of the front of the vehicle, $\mathbf{v}_2^v$ points out the pilots left hand side of the vehicle, and $\mathbf{v}_3^v = \mathbf{v}_1^v \times \mathbf{v}_2^v$ points out of the top of the vehicle. The inertial frame and the vehicle frame should be perfectly aligned (only displaced) if a perfectly straight flight path is flown.

Finally, to define the coordinate frame for the antenna, let the origin be the phase center. Then define the orthogonal coordinate frame by the following unit vectors: $\mathbf{a}_1^a$ points in the azimuth direction, $\mathbf{a}_2^a$ points in the elevation direction, and $\mathbf{a}_3^a = \mathbf{a}_1^a \times \mathbf{a}_2^a$ points in the boresight direction of the antenna (in the direction of the peak of the mainlobe). These coordinate frames are needed in order to describe the attitude of the vehicle, which effects the antenna pointing direction $\mathbf{a}_3^a$.

The attitude of the vehicle carrying the SAR sensor is described by roll, pitch, and yaw. Roll is a rotation about the $\mathbf{v}_1^v$ axis, pitch is a rotation about the $\mathbf{v}_2^v$ axis, and yaw is a rotation about the $\mathbf{v}_3^v$ axis each with respect to the inertial coordinate frame. The vehicle's attitude with respect to the inertial frame can be described by the rotation matrix $\Psi_v^i(t)$ where the subscripts are read "from vehicle to inertial" and the origin of the vehicle's coordinate frame can be described as a displacement from the inertial frame by the vector $\mathbf{x}^i(t)$. Note that since $\Psi_v^i(t)$ is a rotation matrix its inverse is equal to its transpose, thus

$(\Psi_v^i(t))^{-1} = (\Psi_v^i(t))^T = \Psi_i^v(t)$. The matrix $\Psi_i^v(t)$ describes a vector from the inertial frame in the vehicle frame.

As an example of changing coordinate frames, the unit vector that points out of the front of the vehicle has the following description in the inertial frame

$$\mathbf{v}_1^i(t) = \Psi_v^i(t)\mathbf{v}_1^v + \mathbf{x}^i(t). \tag{3.7}$$

This equation can also be written more compactly as

$$\begin{bmatrix} \mathbf{v}_1^i(t) \\ 1 \end{bmatrix} = \left[\begin{array}{c|c} \Psi_v^i(t) & \mathbf{x}^i(t) \\ \hline \mathbf{0}^T & 1 \end{array}\right] \begin{bmatrix} \mathbf{v}_1^v \\ 1 \end{bmatrix}. \tag{3.8}$$

The inverse of this rotation and translation matrix is

$$\left[\begin{array}{c|c} \Psi_v^i(t) & \mathbf{x}^i(t) \\ \hline \mathbf{0}^T & 1 \end{array}\right]^{-1} = \left[\begin{array}{c|c} \Psi_i^v(t) & -\Psi_i^v(t)\mathbf{x}^i(t) \\ \hline \mathbf{0}^T & 1 \end{array}\right]. \tag{3.9}$$

The antenna phase center is typically at a fixed distance from the origin of the vehicle coordinate frame and is rigidly fixed to the vehicle carrying it. However, in some SAR modes it is allowed to be gimballed. For the sake of generality in this development, the antenna frame will be allowed to be gimballed. If the antenna coordinate frame is aligned with the vehicle frame, its non-gimballed orientation with respect to the vehicle reference frame is described by a rotation of $(-90° + \psi_0)$ about $\mathbf{a}_1^a$ and a displacement, $\mathbf{b}_0$, from the origin of the vehicle coordinate system. The antenna pointing direction as seen from the vehicle coordinate frame is given by the matrix equation

$$\begin{bmatrix} \mathbf{a}_3^v(t) \\ 1 \end{bmatrix} = \left[\begin{array}{c|c} \Psi_a^v(t) & \mathbf{b}_0^v \\ \hline \mathbf{0}^T & 1 \end{array}\right] \begin{bmatrix} \mathbf{a}_3^a \\ 1 \end{bmatrix}. \tag{3.10}$$

Combining the two frame changes, the antenna pointing direction in the inertial frame is described by the equation

$$\left[\begin{array}{c} \mathbf{a}_3^i(t) \\ \hline 1 \end{array}\right] = \left[\begin{array}{c|c} \Psi_v^i(t) & \mathbf{x}^i(t) \\ \hline \mathbf{0}^T & 1 \end{array}\right] \left[\begin{array}{c|c} \Psi_a^v(t) & \mathbf{b}_0^v \\ \hline \mathbf{0}^T & 1 \end{array}\right] \left[\begin{array}{c} \mathbf{a}_3^a \\ \hline 1 \end{array}\right]. \tag{3.11}$$

Similarly, the rest of the antenna coordinate directions can be found in the inertial frame and are denoted as $\mathbf{a}_1^i(t)$ and $\mathbf{a}_2^i(t)$.

There are several reasons for keeping track of the pointing direction and location of the antenna. For one, some processing algorithms need to know when a reflector is under the antenna illumination (for some antenna threshold level). Another reason is that compensation for motion errors from some predetermined flight path becomes possible. Another reason is that it makes it possible for a better two-dimensional matched filter to be designed. All of these reasons have the benefit that the image formed from the processed SAR data will be more focused.

Let $\mathbf{u}_0^i$ be a stationary point on the ground in the inertial coordinate frame. This point as viewed from the antenna coordinate frame is

$$\left[\begin{array}{c} \mathbf{u}_0^a(t) \\ \hline 1 \end{array}\right] = \underbrace{\left[\begin{array}{c|c} \Psi_v^a(t) & -\Psi_v^a(t)\mathbf{b}_0^v \\ \hline \mathbf{0}^T & 1 \end{array}\right] \left[\begin{array}{c|c} \Psi_i^v(t) & -\Psi_i^v(t)\mathbf{x}^i(t) \\ \hline \mathbf{0}^T & 1 \end{array}\right]}_{G_i^a(t)} \left[\begin{array}{c} \mathbf{u}_0^i \\ \hline 1 \end{array}\right]. \tag{3.12}$$

With the stationary point on the ground now mapped into the antenna frame, the azimuth and elevation angles that this point makes with the bore-sight of the antenna can be found by projecting this vector onto two appropriate planes spanned by the antenna coordinates. The two projection matrices are

$$P_{az} = \left(\left[\begin{array}{cc} \mathbf{a}_1^a & \mathbf{a}_3^a \end{array}\right] \left(\left[\begin{array}{c} (\mathbf{a}_1^a)^T \\ (\mathbf{a}_3^a)^T \end{array}\right] \left[\begin{array}{cc} \mathbf{a}_1^a & \mathbf{a}_3^a \end{array}\right] \right)^{-1} \left[\begin{array}{c} (\mathbf{a}_1^a)^T \\ (\mathbf{a}_3^a)^T \end{array}\right] \right) \tag{3.13}$$

and

$$P_{el} = \left(\begin{bmatrix} \mathbf{a}_2^a & \mathbf{a}_3^a \end{bmatrix} \left(\begin{bmatrix} (\mathbf{a}_2^a)^T \\ (\mathbf{a}_3^a)^T \end{bmatrix} \begin{bmatrix} \mathbf{a}_2^a & \mathbf{a}_3^a \end{bmatrix} \right)^{-1} \begin{bmatrix} (\mathbf{a}_2^a)^T \\ (\mathbf{a}_3^a)^T \end{bmatrix} \right). \tag{3.14}$$

Using the identity to find the cosine of the angle between two vectors

$$\cos(\vartheta) = \frac{\langle \mathbf{x}, \mathbf{y} \rangle}{||\mathbf{x}||_2 ||\mathbf{y}||_2}, \tag{3.15}$$

the antenna azimuth angle is computed from

$$\theta(t) = \arccos\left(\frac{\langle \mathbf{a}_3^a, P_{az}\mathbf{u}_0^a(t) \rangle}{||P_{az}\mathbf{u}_0^a(t)||_2} \right), \tag{3.16}$$

and the antenna elevation angle is computed from

$$\phi(t) = \arccos\left(\frac{\langle \mathbf{a}_3^a, P_{el}\mathbf{u}_0^a(t) \rangle}{||P_{el}\mathbf{u}_0^a(t)||_2} \right), \tag{3.17}$$

where the fact that $\mathbf{a}_3^a$ is a unit vector has been used. These angles can be used in (3.1) to determine the weighting caused by the antenna pattern in the reflected signal.

3.3 Induced Azimuth Signal

Consider a stationary reflector at a ground location $\mathbf{u}_0^i = (x_0^i, y_0^i, z_0^i)$ and a vehicle (such as an airplane) flying past the reflector with a flight profile given by $\mathbf{x}^i(t) = (x^i(t), y^i(t), z^i(t))$. Unless the airplane is flying an exact circle around the reflector, there will be a relative distance that changes with time between the airplane and the reflector, given as

$$R_0(t) = ||\mathbf{x}^i(t) - \mathbf{u}_0^i||_2 \tag{3.18}$$

$$= \sqrt{(x^i(t) - x_0^i)^2 + (y^i(t) - y_0^i)^2 + (z^i(t) - z_0^i)^2}. \tag{3.19}$$

The time derivative of the relative distance between the airplane and the reflector gives the relative velocity, denoted by $v_{REL}(t)$, between the two. This is described by the equation

$$\begin{aligned} v_{REL}(t) &= \frac{d}{dt}R_0(t) && (3.20)\\ &= \frac{d}{dt}\sqrt{(x^i(t)-x_0^i)^2+(y^i(t)-y_0^i)^2+(z^i(t)-z_0^i)^2} && (3.21)\\ &= \frac{1}{2R_0(t)}\frac{d}{dt}\left((x^i(t)-x_0^i)^2+(y^i(t)-y_0^i)^2+(z^i(t)-z_0^i)^2\right) && (3.22)\\ &= \frac{1}{R_0(t)}\left((x^i(t)-x_0^i)\dot{x}^i(t)+(y^i(t)-y_0^i)\dot{y}^i(t)+(z^i(t)-z_0^i)\dot{z}^i(t)\right) && (3.23)\\ &= \frac{(\mathbf{x}^i(t)-\mathbf{u}_0^i)^T\dot{\mathbf{x}}^i(t)}{||\mathbf{x}^i(t)-\mathbf{u}_0^i||_2} && (3.24)\\ &= \frac{\left\langle\dot{\mathbf{x}}^i(t),(\mathbf{x}^i(t)-\mathbf{u}_0^i)\right\rangle}{||\mathbf{x}^i(t)-\mathbf{u}_0^i||_2}. && (3.25) \end{aligned}$$

In a later chapter, the time derivative of the relative velocity will also be needed. This quantity is the relative acceleration between the airplane and the reflector and is denoted by $a_{REL}(t)$. Computing the derivative and after some algebraic manipulations, the relative acceleration is given by

$$a_{REL}(t)=\frac{\left(||\dot{\mathbf{x}}^i(t)||_2^2+\left\langle\ddot{\mathbf{x}}^i(t),(\mathbf{x}^i(t)-\mathbf{x}_0^i)\right\rangle\right)||\mathbf{x}^i(t)-\mathbf{x}_0^i||_2^2-\left(\left\langle\dot{\mathbf{x}}^i(t),(\mathbf{x}^i(t)-\mathbf{x}_0^i)\right\rangle\right)^2}{||\mathbf{x}^i(t)-\mathbf{x}_0^i||_2^{3/2}}. \quad (3.26)$$

If the sensor is transmitting a pure sinusoidal signal through an isotropic antenna, the relative velocity induces a Doppler shift in the received signal. The Doppler shift is a function of time because the relative velocity is. The equation for the Doppler shift is given by (note that $v_{REL}(t) << c$, $\forall t$)

$$f_D(t)=-\frac{2v_{REL}(t)}{\lambda}, \quad (3.27)$$

where λ is the wavelength of the transmitted frequency. Notice that the equation for $f_D(t)$ is just a scaling of the equation for the relative velocity. Another important function is the

time derivative of the Doppler frequency,

$$\dot{f}_D(t) = -\frac{2a_{REL}(t)}{\lambda}. \tag{3.28}$$

Let the sensor transmit the pure sinusoidal signal

$$s(t) = \cos(2\pi f_c t), \tag{3.29}$$

and assume there is only a single ideal reflector and the sensor transmits through an isotropic antenna. Ignoring propagation loss, the received reflected signal is

$$r(t) = \cos(2\pi f_c(t - \tau(t)), \tag{3.30}$$

where $\tau(t)$ is the time delay of the round trip of the signal. To be explicit, the received signal is

$$\begin{aligned} r(t) &= \cos\left(2\pi f_c\left(t - \frac{2R_0(t)}{c}\right)\right) && (3.31)\\ &= \cos\left(2\pi f_c t - 4\pi R_0(t)\frac{f_c}{c}\right) && (3.32)\\ &= \cos\left(2\pi f_c t - \frac{4\pi}{\lambda}R_0(t)\right). && (3.33) \end{aligned}$$

Quadrature demodulating (to preserve the phase of the received signal) the received signal becomes

$$\begin{aligned} \tilde{r}(t) &= e^{-j\frac{4\pi}{\lambda}R_0(t)} && (3.34)\\ &= e^{j2\pi\phi(t)}. && (3.35) \end{aligned}$$

A SAR image has excellent range resolution due to pulse compression, but the high azimuth resolution comes from exploiting this induced signal.

3.4 Bandwidth of the Induced Azimuth Signal

As we have seen in the previous section, an azimuth signal is induced by the Doppler shift between the sensor and a stationary reflector. Since the pulsed signal is being transmitted through an antenna, the induced azimuth signal will be modulated by the power pattern of the antenna. More explicitly, the quadrature demodulated received signal from a pure sinusoidal transmission has the form

$$\tilde{r}(t) = a(\theta(t), \phi(t)) e^{-j\frac{4\pi}{\lambda} R_0(t)}. \tag{3.36}$$

Upon first glance, the bandwidth of this signal may appear to be range dependent. In a future chapter, it will be shown the the bandwidth of this induced signal is *not* range dependent. In fact, it will be shown that the important contributing factors to the bandwidth of this signal is the velocity of the sensor and the length of the antenna.

The spectrum of the induced signal is greatly affected by the azimuth dimension of the antenna. The antenna has a finite size, therefore the bandwidth of the induced signal is infinite and a pulsed SAR system will automatically have spatial aliasing in the azimuth direction. A wider main lobe in the azimuth direction increases the bandwidth of the induced signal. This is very important to know, because to design a pulsed system, we need to know how often to pulse (the spatial sampling rate) and this can be determined by setting some frequency threshold level. Based on this threshold level, the Nyquist sampling rate tells us what our PRF should be to avoid significant spatial aliasing.

Another factor that affects the spectrum of the azimuth signal is if the vehicle carrying the sensor has a non-zero yaw angle, as this causes the antenna to squint. The antenna squinting, forward or backward, has the effect of shifting the spectrum of the induced signal.

One other factor that effects the choice of the PRF is the range from the sensor to the scene. Enough time for the round-trip of a transmitted pulse to the far range of the scene of interest must elapse before transmitting another pulse, otherwise range ambiguities will occur.

3.5 Pulse Transmission and Range Sampling

Ideally, a pulsed SAR sensor travels along its flight path and transmits pulses at the properly computed PRF rate. If the velocity is held constant and the flight path is linear, then the transmitted pulses occur at equally spaced distances.

After transmitting a pulse, an amount of time called the range gate delay (RGD) elapses before the sensor starts to sample the returned signal. For imaging the ground, it makes sense to wait until at least enough time has gone by to have the signal hit the closest point on the ground (usually nadir) and travel back to the sensor before sampling. Thus, the RGD is

$$\tau_{RGD} \geq \frac{2}{c}h. \tag{3.37}$$

For convenience, let the RGD be an integer multiple of the sampling period, (*i.e.* $\tau_{RGD} = N_d T_s$). After the RGD has elapsed, the SAR sensor samples the complex quadrature demodulated signal every T_s seconds (the sampling rate is f_s). The sampling rate is selected to satisfy the Nyquist sampling theorem for complex signals, which is sampling at a rate that is at least the two-sided bandwidth of the complex baseband signal (the Nyquist sampling rate for complex signals differs from the Nyquist sampling rate for a real signal where you must sample at least twice the highest frequency of the baseband signal).

3.6 Model for the Range Sampled Data

For a moment, assume the antenna is isotropic (the transmitted signal expands spherically from the antenna). Let the sensor be at an altitude of h meters above the ground and let t_0 denote amount of time required for a transmitted pulse to hit the ground. If the ground is flat, then the first spot on the ground where the wavefront will reflect from will be the nadir point. At the time when the wavefront hits nadir, it has been traveling for t_0 seconds and the radius of the spherical wavefront (the range from the sensor) at this point is $R(t_0) = ct_0 = h$ meters. After $t_0 + \Delta t$ seconds, the wavefront has expanded to a sphere of radius $R(t_0 + \Delta t) = c(t_0 + \Delta t)$ meters. The intersection of the wavefront and the

ground will not correspond to a single point anymore, but to a circular contour of radius $R_G(t_0 + \Delta t) = R(t_0 + \Delta t)\sin(\gamma(t_0 + \Delta t))$ about the nadir point (the subscript G indicates the radius on the ground) where $\gamma(t_0 + \Delta t)$ is the incidence angle at time $t = t_0 + \Delta t$. In general the equation for the radius of equal contour on a flat ground is given by

$$R_G(t) = R(t)\sin(\gamma(t)), \quad t \geq t_0. \tag{3.38}$$

An illustration of the intersection of the wavefront with the ground for equal time instants is shown in figure 3.3 where the flight path is parallel to the x-axis and is directed out of the image. In the figure, the bold blue lines represent a two-dimensional slice of the three-dimensional wavefront at equally spaced time instants, the bold red lines represent the intersection of the spherical wavefront with the ground at those time instants, and the bold black lines are the radius of the wavefront from the sensor to the intersection of the wavefront and the ground (the incidence angle is the angle made between the nadir line and the bold black lines with respect to the antenna origin). An important thing to note from figure 3.3 is that if the sensor is above the ground, then the wavefront at equally spaced time intervals *do not* correspond to equally spaced contours on the ground. This becomes important if a focused SAR image needs to be geo-referenced.

Let the isotropic antenna be at the inertial location $\mathbf{x}_0^i$ and assume that the only reflectors on the ground are at the same range, $R(\nu_1)$, from the antenna position. The reflected signal from these reflectors will have the same delay. Let $\mathbf{u}^i$ be the ground coordinates in the inertial frame and denote the reflectivity of these reflectors as $g(\mathbf{u}^i)\delta\left(||\mathbf{x}_0^i - \mathbf{u}^i||_2 - R(\nu_1)\right)$. Let the transmitted signal be denoted as $s(t)$, the reflected signal from these reflectors will show up back at the antenna after $\tau(\nu_1) = 2R(\nu_1)/c$ seconds. Taking into account the two-way propagation loss of the signal, the received signal has the form

$$r(t) = \frac{\mathcal{C}}{R^4(\nu_1)} \left(\oint\limits_{||\mathbf{x}_0^i - \mathbf{u}^i||_2 = R(\nu_1)} g(\mathbf{u}^i) d\mathbf{u}^i \right) s\left(t - \tau(\nu_1)\right), \tag{3.39}$$

where the integral is over the ground plane and the contour is along the intersection of

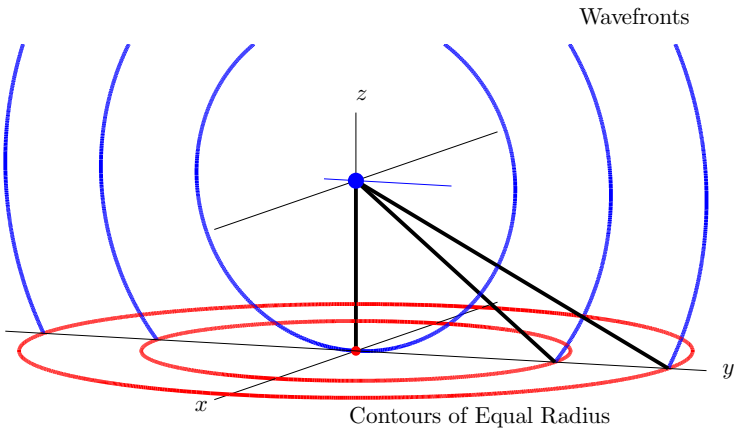

Fig. 3.3: Illustration of the expanding wavefront from a transmitted pulse from an isotropic antenna. The bold blue contours are a two-dimensional slice of the spherical wavefronts and the red lines are the intersection between these wavefronts and the ground.

the sphere of radius $R(\nu_1)$ and the ground plane. This equation says that the signal that shows up on the antenna is a delayed version of the transmitted signal, weighted by the contour integral of the ground reflectivity and the propagation losses. If there were a second set of reflectors on the ground at the range $R(\nu_2)$, then the returned signal would be the superposition of the two. More generally, for a continuum of reflectors, the equation that describes the received signal at the antenna is the convolution integral

$$r(t) = \int \frac{\mathcal{C}}{R^4(\nu)} \left(\oint_{||\mathbf{x}_0^i - \mathbf{u}^i||_2 = R(\nu)} g(\mathbf{u}^i) d\mathbf{u}^i \right) s\left(t - \tau(\nu)\right) d\nu. \tag{3.40}$$

If the effect of the antenna is included, then the contour will be weighted by the power pattern of the antenna. This is illustrated in figure 3.4 for the range contour at a single instant in time on a flat ground. The antenna power pattern is the bold blue line and represents the relative weighting from the reflectors along the equal contour (red line).

The attitude of the vehicle carrying the antenna must also be taken into account to

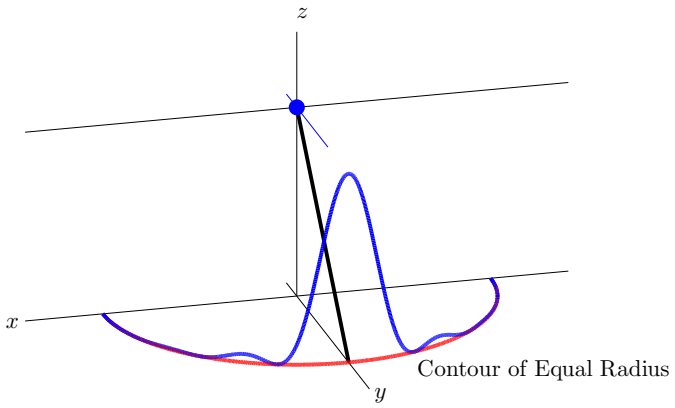

Fig. 3.4: Illustration of the expanding wavefront from a transmitted pulse from a two-dimensional antenna array at a single instant in time. The bold blue line indicates the weighting of the reflectors along the red line.

properly describe the signal that is received at the antenna. The matrix $G_i^a(t)$ in (3.12) transforms the ground coordinates $\mathbf{u}^i$ into the antenna frame so that the attitude can be accounted for. Thus (3.40) becomes

$$r(t) = \int \frac{\mathcal{C}}{R^4(\nu)} \left(\oint_{||\mathbf{x}_0^i - \mathbf{u}^i||_2 = R(\nu)} a\left(\theta(G_i^a \mathbf{u}^i), \phi(G_i^a \mathbf{u}^i)\right) g(\mathbf{u}^i) d\mathbf{u}^i \right) s\left(t - \tau(\nu)\right) d\nu. \tag{3.41}$$

If the sensor is transmitting multiple pulses while traveling along its flight path, then the received signal from each pulse will have the same form, but there will be a displacement in the vehicle's position and there is a possibility that the attitude of the vehicle has changed as well. The general equation for the received signal from the k^{th} pulse is

$$r(k,t) = \int q(k,\nu) s\left(t - \tau(\nu) - kT\right) d\nu, \tag{3.42}$$

where

$$q(k,\nu) = \frac{\mathcal{C}}{R^4(\nu)} \left(\oint_{||\mathbf{x}_k^i - \mathbf{u}^i||_2 = R(\nu)} a\left(\theta(G_i^a(k)\mathbf{u}^i), \phi(G_i^a(k)\mathbf{u}^i)\right) g(\mathbf{u}^i) d\mathbf{u}^i \right). \tag{3.43}$$

Assume that the received signal is quadrature demodulated (denote the quadrature demodulated received signal from the k^{th} pulse as $d(k,t)$), then after the RGD has elapsed (using $\tau_{RGD} = N_d T_s$), N_n samples are taken from the received signal from the k^{th} pulse at $t = (n + N_d)T_s + kT$. Thus, the sampled data has the form

$$d(k,n) = d(k,t)\,\big|_{t=(N_d+n)T_s+kT}\,, \quad 0 \le n \le N_n - 1, \tag{3.44}$$

where $(N_d + N_r - 1)T_s \le T$.

An important observation to note is that the n^{th} sample from the k^{th} pulse contains information not only from all the reflectors along the contour of equal radius from the antenna, but also from the region (due to the convolution integral and the pulse duration) between the the contours of equal radius that are separated in time by $\pm T_p$ seconds in range (or the samples in the range $n - \lceil T_p/T_s \rceil$ to $n + \lfloor T_p/T_s \rfloor$). This is illustrated in figure 3.5 where the red dot on the ground represents the range associated with the n^{th} sample from the k^{th} pulse, the red line represents the contour of equal radius at the sampling instant of the n^{th} sample, and the green region represents all of the ground region that contributes to $d(k,n)$ (the antenna weighting is not shown). As can be seen, the n^{th} sample of the k^{th} pulse contains information about reflectors in quite a large neighborhood about the range that $d(k,n)$ corresponds to.

The collected data from a pulsed SAR sensor forms a two-dimensional array. The $(k,n)^{th}$ entry of this array is $d(k,n)$ where n indexes the range samples from pulse k.

3.7 SAR Image Formation

As was seen in the previous section, the true ground reflectivity, which belongs to $\mathcal{X}$, the Euclidean space of square-integrable functions (*i.e.* $g(\cdot) \in L^2$), is mapped to the

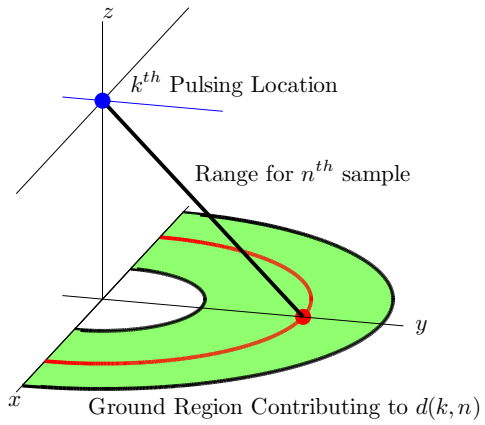

Fig. 3.5: Illustration of all of the ground region that contributes to $d(k,n)$ (the n^{th} sample of the received signal from the k^{th} pulse).

finite dimensional Euclidean space $\mathcal{Y}$ of two-dimensional arrays. Since the equations that describe this mapping are integrals (and sampling) the mapping $\mathcal{L} : \mathcal{X} \rightarrow \mathcal{Y}$ is linear. In SAR image formation, it is important to know how well $g(\cdot)$ can be reconstructed from the data samples. The contents of this section discuss the pulsed SAR system point-spread function, point-spread response, range resolution, and azimuth resolution.

3.7.1 SAR Point-Spread Function

The point-spread function (PSF) of an imaging system is also sometimes called the impulse response [16]. However, the term impulse response is usually reserved for linear time/space invariant systems [6]. Since a SAR system is spatially varying, the term point-spread function will be used to describe a SAR system and the term point-spread response (PSR) will be used to describe the response of the SAR sensor to a particular reflector.

To model the PSR of a generic linear imaging system, an impulse is used as the input to the system PSF and the output is computed. Similarly, a model of the PSR of a SAR sensor is found by placing a single ideal reflector in the scene and computing the output. As

an example, assume there is only a single ideal reflector in the scene being imaged located at the ground location $\mathbf{u}_0^i$, thus the ground reflectivity function is $g(\mathbf{u}^i) = \delta(\mathbf{u}^i - \mathbf{u}_0^i)$. After quadrature demodulation and sampling, (3.42) becomes

$$d(k,n) = f(k,n,\mathbf{u}^i)\big|_{\mathbf{u}^i=\mathbf{u}_0^i} \tag{3.45}$$

$$= q(k,\nu_k)\tilde{s}\left((N_d+n)T_s - \tau(\nu_k)\right), \ \forall k \ s.t. \ \tau(\nu_k) \leq T \tag{3.46}$$

where $f(k,n,\mathbf{u}^i)$ is the PSF of the SAR system, $\tau(\nu_k)$ denotes the round-trip delay to the single ideal reflector on the k^{th} pulse, and $\tilde{s}(\cdot)$ is the sampled and demodulated waveform. The N_n range samples are taken after the RGD where $(N_d + N_n - 1)T_s \leq T$. The range samples from each pulse become the rows of the two-dimensional data array $d(k,n)$. As can be seen from (3.46), it is clear that the PSR varies with the range to the reflector, thus the PSF of SAR sensors is spatially varying. In this example, the collected data can be related to the PSF because of the choice of the ground reflectivity function.

What is *not* modeled by (3.46) is that the true PSR will contain samples of pulses outside of the limit of k defined above. The model above assumes that any pulses outside the limits of k will be too greatly attenuated (between the propagation loss and that the transmission and reception are coming out of sidelobes far from the mainlobe) to matter.

It would be ideal if there were a way to process $d(k,n)$ that would recover $g(\mathbf{u}_0^i) = \delta(\mathbf{u}^i - \mathbf{u}_0^i)$, however because of the mapping of spaces from $\mathcal{X}$ to $\mathcal{Y}$ this is not possible. Even though the focused image (denoted as $\mathbf{g}$) is in $\mathcal{Y}$ space, we desire to have it represent $g(\cdot)$ as closely as possible. The closest a reconstructed image can get to the original is limited by the resolvable limits of the SAR system. The resolvable limits of the SAR system are a function of many different system parameters, two of which are the bandwidth of the system and the antenna beam pattern. It will be shown that traditional methods of processing SAR data lead to inter-pixel interference (IPI) about the reflectors in the image. The model-based algorithms developed in this dissertation account for the IPI and the reconstructed image $\mathbf{g}$ is as "close" to $g(\cdot)$ as possible.

3.7.2 SAR Resolution

As in traditional radar, SAR resolution is defined as the ability to resolve between two closely spaced reflectors. It does not refer to the number of pixels that make up a focused image. To help visualize this, let an $N_a \times N_r$ focused SAR image be up-sampled and interpolated in both the azimuth and range directions. Even though the pixel count of the image has gone up, no new information was gained to help resolve between two reflectors.

The resolution of a SAR image is physically limited by the bandwidth of the range and azimuth signals (algorithms exist to extrapolate the bandwidth and lead to results known as *super-resolution* [17, 18]). The resolution in the range direction is essentially the same as in (2.44) (if a compressible pulse is used), however the azimuth resolution is specific to the SAR modality (*i.e.* spotlight, stripmap, etc.). A discussion on the azimuth resolution for stripmap SAR will be given in the next chapter.

Traditional SAR imaging algorithms (Fourier or time-domain algorithms) leave large "star-like" IPI patterns around the reflectors in the processed image (the stronger the reflector, the more noticeable the IPI). The magnitude of the IPI about a reflector in range for a matched filtered signal is similar to that shown in figure 2.6. Similar IPI will also exists in the azimuth direction because the azimuth processing is also accomplished via matched filtering.

As can be inferred from figure 2.6, if a strong reflector is adjacent to weaker reflectors, then the weaker reflectors could easily be masked by the sidelobes of the IPI from the stronger reflector. If this occurs, the range resolution as defined above does not quite hold, as the two reflectors are no longer resolvable. The imaging methods developed in this dissertation combat this effect and restore the reasonable definition of resolution above.

Chapter 4

Pulsed LFM Stripmap Synthetic Aperture Radar

This chapter introduces the geometry of an ideal flight for stripmap SAR. Based on this geometry, the range dependent length of the synthetic aperture is given. From the length of the synthetic aperture and the velocity of the sensor, the amount of time that a reflector (at a given range) is in the synthetic aperture can be computed. It is also shown that the induced azimuth signal for an ideal flight has the form of a weighted (by the antenna pattern) symmetric LFM signal with time duration given by the computed time the reflectors are in the synthetic aperture. The bandwidth of this induced LFM signal is discussed, and from this the pulse repetition frequency for the system can be obtained. Next, a lower bound on the range and azimuth resolution is derived. The chapter concludes by showing the necessary steps for forming a stripmap SAR image and a short discussion of the image formation algorithms is given.

This chapter provides a theoretical foundation for the forward model presented in Chapter 5 and gives equations that are needed to build a simulator.

4.1 Stripmap Geometry

The ideal flight path in stripmap SAR is a straight line at a constant altitude with no roll, pitch, or yaw. Ideally the sensor transmits pulses at equally spaced intervals (this implies a constant velocity for a fixed PRI). Also, the pointing direction of the antenna is such that the peak of the main lobe of the antenna is perpendicular to the flight track and has a constant grazing angle ψ_0 as shown in figure 4.1. In figure 4.1, the dashed blue and black lines form a plane that is parallel to the ground, the dashed blue line indicates the flight path of the sensor (out of the figure), the solid blue line indicates the antenna pointing direction, and the red ellipse indicates the antenna main lobe footprint on the ground.

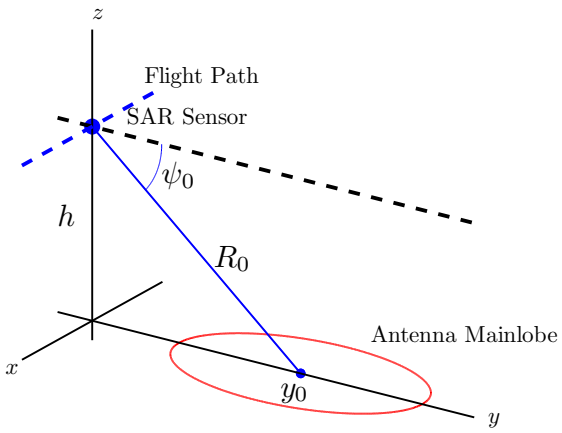

Fig. 4.1: Illustration of stripmap SAR geometry. The sensor, moving with constant velocity in the x-direction, is at an altitude h in the z-direction and the main beam of the antenna makes a grazing angle ψ_0 with the plane containing the SAR sensor in the cross-track (range) y-direction.

For an ideal stripmap flight described by the vector $(vt, 0, h)$ and a single point target at $\mathbf{u}_0 = (0, y_0, 0)$, the equations derived in Chapter 3 for the relative range, relative velocity, relative acceleration, Doppler frequency, and Doppler rate are as follows (note that $R_0^2 = y_0^2 + h^2$):

$$R(t) = \sqrt{(vt)^2 + R_0^2} \tag{4.1}$$

$$v_{REL}(t) = \frac{v^2 t}{\sqrt{(vt)^2 + R_0^2}} \tag{4.2}$$

$$a_{REL}(t) = \frac{v^2 R_0^2}{\left((vt)^2 + R_0^2\right)^{3/2}} \tag{4.3}$$

$$f_D(t) = -\frac{2v^2 t}{\lambda\sqrt{(vt)^2 + R_0^2}} \tag{4.4}$$

$$\dot{f}_D(t) = -\frac{2v^2 R_0^2}{\lambda\left((vt)^2 + R_0^2\right)^{3/2}}. \tag{4.5}$$

Motion compensation algorithms exist and can be used to correct for such things as: non-constant velocity, non-ideal attitude, and deviations from a linear flight path. The

traditional methods for motion compensation will not be covered in this dissertation, but the interested reader may refer to [19, 20].

4.2 Synthetic Aperture for Stripmap SAR

It could be argued that the length of the synthetic aperture is infinite due to the azimuth sidelobes of the antenna. Therefore, in order to have a meaningful discussion of the synthetic aperture for stripmap SAR, some angular threshold must be set in azimuth. In this development, the azimuth angular threshold will be the first nulls on either side of the mainlobe. For the antenna as defined in (3.1), the first-null beamwidth in azimuth is (setting $\phi = 0^\circ$)

$$\vartheta_N = 2 \arcsin\left(\frac{\lambda}{L}\right). \tag{4.6}$$

For the sake of having a reference, the following development assumes an ideal stripmap geometry. Let the length of the synthetic aperture be denoted as L_a and let an ideal reflector be located at $\mathbf{u}_0^i = (0, y_0^i, 0)$ on the ground such that it passes under the boresight of the antenna as the vehicle passes by. Then $R_0 = R(t = 0)$ in (4.1) denotes the closest range from the antenna to the reflector on the ground when the vehicle is passing by. The geometry for computing L_a from ϑ_N is illustrated in figure 4.2. In figure 4.2, the perspective is from above, the red lines represent the antenna first-null beamwidth for the two extreme pulsing locations where the reflector first enters the main lobe of the beam and finally leaves the main lobe of the beam, the blue line represents the closest range from the antenna to the reflector when the vehicle is passing by. From the geometry in figure 4.2, it is seen that the

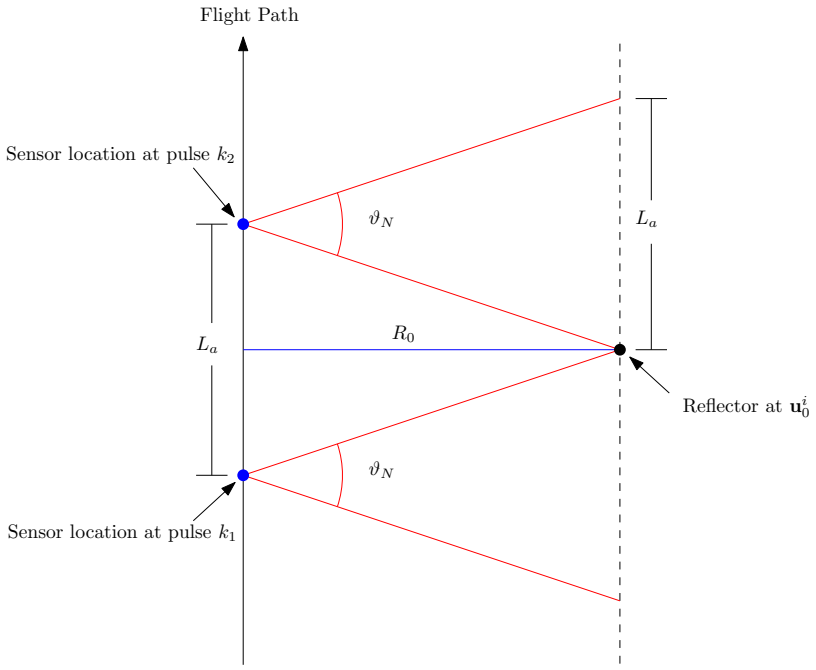

Fig. 4.2: Illustration of the synthetic aperture geometry for stripmap SAR (the perspective is from above).

length of the synthetic aperture is

$$\begin{aligned} L_a &= 2R_0 \tan\left(\frac{\vartheta_N}{2}\right) && (4.7)\\ &= 2R_0 \tan\left(\arcsin\left(\frac{\lambda}{L}\right)\right) && (4.8)\\ &= 2R_0 \left(\frac{\sin\left(\arcsin\left(\frac{\lambda}{L}\right)\right)}{\cos\left(\arcsin\left(\frac{\lambda}{L}\right)\right)}\right) && (4.9)\\ &= \frac{2R_0\lambda}{L\cos\left(\frac{\vartheta_N}{2}\right)}, && (4.10) \end{aligned}$$

where (4.6) is used. Thus, we see that L_a is range dependent; the synthetic aperture is longer for larger ranges. If $\lambda << L$ (*i.e.* a narrow beam in azimuth), then $\cos(\vartheta_N/2) \approx 1$, giving

$$\begin{aligned} L_a &\approx 2R_0\frac{\lambda}{L} && (4.11)\\ &\approx R_0\vartheta_N. && (4.12) \end{aligned}$$

This approximation is used quite often. However for this development, (4.10) will be used; it is still defined in terms of the SAR system parameters. Also, it is important to note that the value of L_a computed here is twice the value commonly found where L_a is defined in terms of ϑ_{3dB}, [13, 15].

It is also important to know how long the reflectors at different ranges are in the antenna beam, as this will relate to the bandwidth of the induced azimuth signal. If it takes the sensor T_a seconds to traverse L_a meters at a constant velocity (denoted as v), then using the same reflector as defined above, the time the reflector is in the antenna beam is

$$T_a = \frac{L_a}{v} \tag{4.13}$$

$$= \frac{2R_0\lambda}{vL\cos\left(\frac{\vartheta_N}{2}\right)}. \tag{4.14}$$

4.3 Induced Azimuth Signal for Stripmap SAR

The induced azimuth signal for an ideal flight is very similar to a symmetric LFM signal, as the following example demonstrates.

In this example, let the ideal flight path be at an altitude h and velocity v given as $\mathbf{x}^i(t) = (vt, 0, h)$, let the stationary reflector be positioned at a location $\mathbf{u}_0^i = (0, y_0, 0)$, and assume an isotropic antenna and no propagation loss. Then $\dot{\mathbf{x}}^i(t) = (v, 0, 0)$ and $(\mathbf{x}^i(t) - \mathbf{u}_0^i) = (vt, -y_0, h)$, giving

$$v_{REL}(t) = \frac{v^2 t}{\sqrt{(vt)^2 + y_0^2 + h^2}}. \tag{4.15}$$

The geometry for this example with $h = 500$ m, $y_0 = 500$ m, and $v = 60$ m/s is illustrated in figure 4.3, where the blue dots indicate samples of the sensor location while it is flying along, the red dot indicates the location of the reflector, and the blue lines connecting the blue and red dots indicate the range between the two. Notice that as the sensor approaches the reflector that the range gets shorter and as it moves away the range starts to increase again. A plot of the relative velocity between the sensor and the reflector is

illustrated in figure 4.4. The Doppler frequency starts at a high frequency and monotonically decreases, as illustrated in figure 4.5.

To illustrate the received signal after quadrature demodulation, let $f_c = 3 \times 10^9$ Hz ($\lambda = 0.1$ m). It is difficult to see upon first glance, but when the received signal from the linear flight path is quadrature demodulated, the baseband signal has a very close resemblance to a symmetric LFM signal. The instantaneous frequency of the baseband signal is given as the time derivative of the phase. In the case of the ideal flight, the instantaneous frequency is

$$\begin{aligned} \frac{d}{dt}\phi(t) &= \frac{d}{dt}\left(-\frac{2}{\lambda}R_0(t)\right) && (4.16) \\ &= -\frac{2v_{REL}(t)}{\lambda} && (4.17) \\ &= f_D(t). && (4.18) \end{aligned}$$

Thus, from figure 4.5, it is seen that the frequency content is approximately linear as the sensor is passing the reflector. The real part of the quadrature demodulated baseband signal for this example is illustrated in figure 4.6 for the time interval $-0.5 \leq t \leq 0.5$ seconds.

A matched filter can be designed for this induced symmetric LFM signal. As will be shown below, with a little extra work, this matched filter can be applied for azimuth compression. It is very important to observe that the induced azimuth signal is range dependent.

4.4 Bandwidth of the Induced Azimuth Signal

If we include the antenna pattern and the propagation loss along with the time limits determined from the time the reflector is in the synthetic aperture, then the induced azimuth signal for a non-pulsed linear flight, which was given in (3.36), becomes

$$r(t) = \frac{\mathcal{C}}{R_0^4(t)} a(\theta(t), \phi) e^{-j\frac{4\pi}{\lambda}R_0(t)}, \quad -\frac{T_a}{2} \leq t \leq \frac{T_a}{2}, \tag{4.19}$$

where $\phi(t)$ is held constant because of the assumption of the ideal flight path.

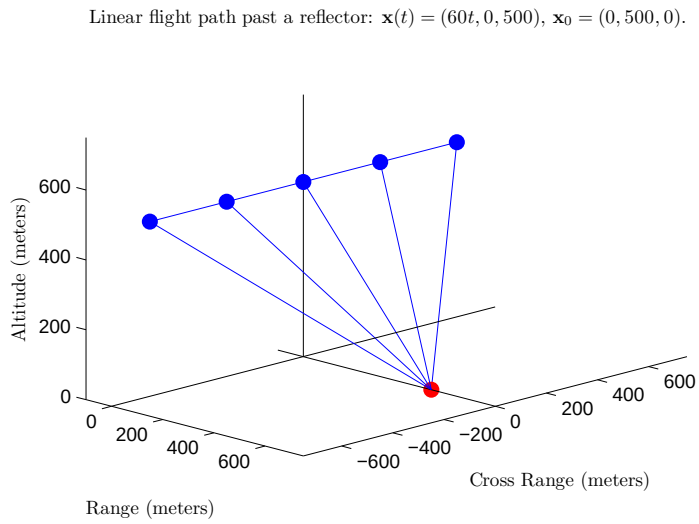

Fig. 4.3: Illustration of the changing range from a linear flight path past a stationary reflector.

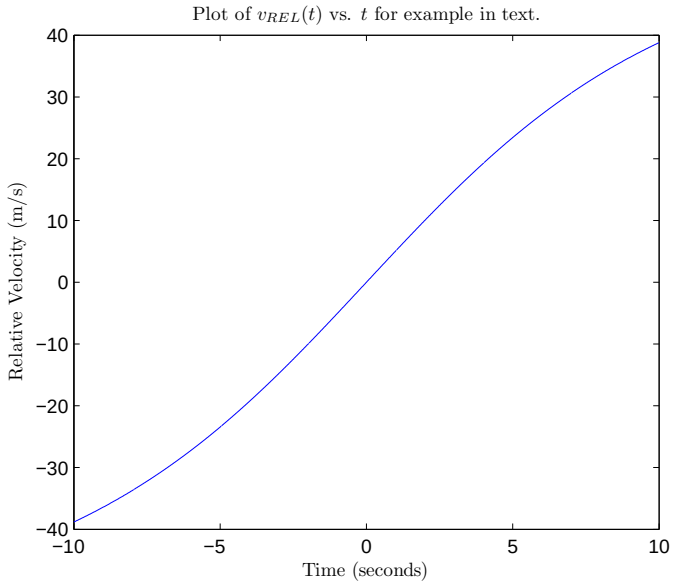

Fig. 4.4: Illustration of the relative velocity between the sensor and the stationary reflector with the parameters as given in the text.

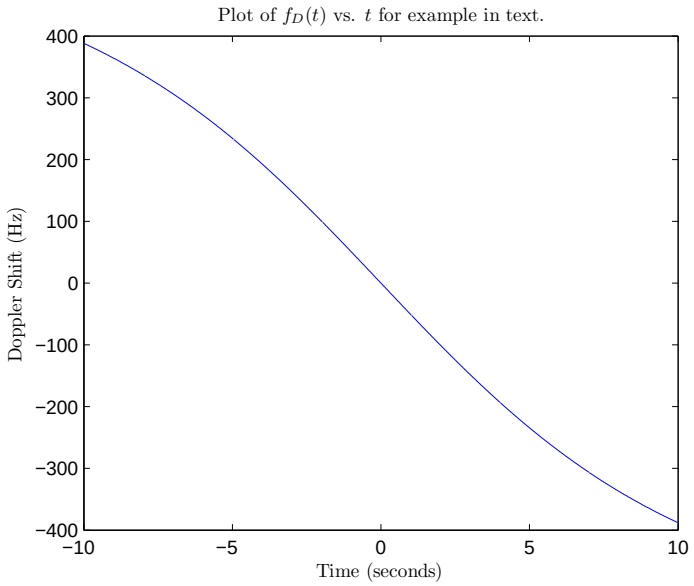

Fig. 4.5: Illustration of the Doppler shift in the received signal with the parameters as given in the text.

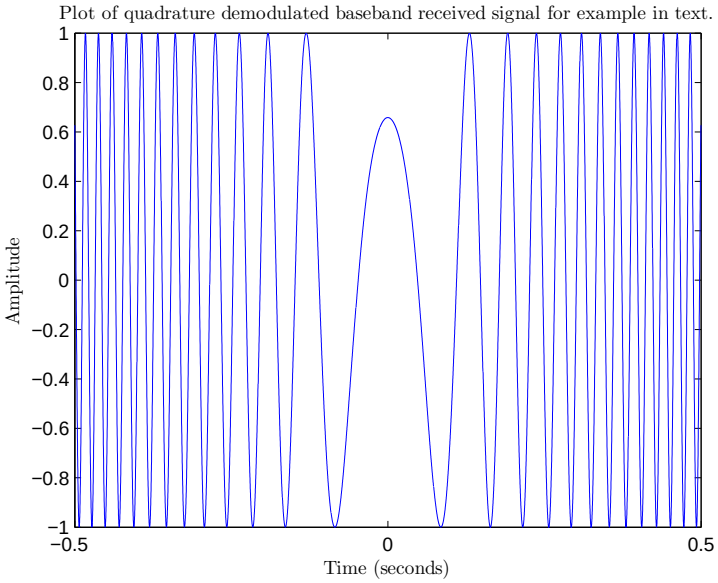

Fig. 4.6: Illustration of the real part of the quadrature demodulated baseband signal with the parameters as given in the text. Note the similar appearance to a symmetric LFM signal.

As the previous section showed, the induced azimuth signal from an isotropic antenna is similar to a symmetric LFM signal when an ideal flight path is flown. Due to the linear relationship between time and frequency

$$f_{D,LFM}(t) = \alpha_a t, \quad -T_a/2 \leq t \leq T_a/2, \tag{4.20}$$

where α_a is the azimuth Doppler rate, the approximate bandwidth of a LFM signal is

$$\begin{aligned} BW_{Az,LFM} &= \left| f_{D,LFM}\left(\frac{T_a}{2}\right) - f_{D,LFM}\left(-\frac{T_a}{2}\right) \right| \\ &= \left|\alpha_a T_a\right|. \end{aligned} \tag{4.21}$$

Most bandwidth derivations for stripmap SAR use the narrow beam approximation so the induced azimuth signal resembles a symmetric LFM signal very closely. In these narrow beam derivations, α_a is found from (4.3) evaluated at $t = 0$ (when the Doppler frequency is approximately linear)

$$\alpha_a = \dot{f}_D(t)\Big|_{t=0} = -\frac{2a_{REL}(t)}{\lambda}\Big|_{t=0} \tag{4.22}$$

$$= -\frac{2}{\lambda}\frac{v^2 R_0^2}{\left((vt)^2 + R_0^2\right)^{3/2}}\Bigg|_{t=0} \tag{4.23}$$

$$= -\frac{2}{\lambda}\frac{v^2}{\sqrt{R_0^2}} \tag{4.24}$$

$$= -\frac{2v^2}{\lambda R_0}. \tag{4.25}$$

At first glance, it may appear that the bandwidth of the symmetric LFM signal is a function of range because α_a is, however, substituting in the definitions of α_a and T_a into (4.21), which gives

$$BW_{Az,LFM} = \left| \left(-\frac{2v^2}{\lambda R_0}\right)\left(\frac{2R_0\lambda}{vL\cos\left(\frac{\vartheta_N}{2}\right)}\right) \right| \tag{4.26}$$

$$= \frac{4v}{L\cos\left(\frac{\vartheta_N}{2}\right)}, \tag{4.27}$$

which shows that the bandwidth of the approximate LFM signal is independent of the range to the reflector.

If the antenna does not have a narrow beam, this definition of bandwidth can greatly overestimate the actual significant bandwidth. The bandwidth for this development will be defined in a similar fashion, however (4.4) will be used instead of (4.20). The bandwidth that will be used in this dissertation is

$$
\begin{aligned}
BW_{Az} &= \left| f_D\left(\frac{T_a}{2}\right) - f_D\left(-\frac{T_a}{2}\right) \right| && (4.28)\\
&= \left| -\frac{2v^2\left(\frac{T_a}{2}\right)}{\lambda\sqrt{(v\left(\frac{T_a}{2}\right))^2 + R_0^2}} + \frac{2v^2\left(-\frac{T_a}{2}\right)}{\lambda\sqrt{(v\left(-\frac{T_a}{2}\right))^2 + R_0^2}} \right| && (4.29)\\
&= \frac{4v^2\left(\frac{T_a}{2}\right)}{\lambda\sqrt{(v\left(\frac{T_a}{2}\right))^2 + R_0^2}} && (4.30)\\
&= \frac{4v^2\left(\frac{\lambda R_0}{vL\cos\left(\frac{\theta_N}{2}\right)}\right)}{\lambda\sqrt{\left(v\left(\frac{\lambda R_0}{vL\cos\left(\frac{\theta_N}{2}\right)}\right)\right)^2 + R_0^2}} && (4.31)\\
&= \frac{4vR_0}{L\cos\left(\frac{\theta_N}{2}\right)\sqrt{\left(\frac{\lambda R_0}{L\cos\left(\frac{\theta_N}{2}\right)}\right)^2 + R_0^2}} && (4.32)\\
&= \frac{4v}{\sqrt{\lambda^2 + L^2\cos^2\left(\frac{\theta_N}{2}\right)}}. && (4.33)
\end{aligned}
$$

Using (4.6) and the identity

$$\cos(\arcsin(x)) = \sqrt{1 - x^2} \tag{4.34}$$

gives

$$BW_{Az} = \frac{4v}{L}. \tag{4.35}$$

The bandwidth as defined in (4.35) is also independent of the range to the reflector

and *only* depends on the antenna length and the velocity of the sensor. This definintion is also twice the value usually found for the azimuth bandwidth. This is because we are using ϑ_N instead of ϑ_{3dB}. It will be shown in an example that if ϑ_{3dB} is used, then noticeable aliasing is more likely to occur.

Using the parameters in the example from the previous section, the following illustrates the induced azimuth signals from an isotropic antenna compared to the antenna defined in (3.1). With the reflector located at $\mathbf{u}_0^i = (0, 500, 0)$, using $v = 60$ m/s, and antenna parameters $L = 0.4$ m, $W = 0.2$ m, and $\lambda = 0.1$ m, we get that the flight path of the sensor is described by $\mathbf{x}(t) = (60t, 0, 500)$, $\vartheta_N = 28.995°$, $L_a = 365.1484$ m, and $T_a = 6.0858$ seconds. From (4.4), the induced Doppler shift is

$$f_D(t) = -\frac{72,000t}{\sqrt{3600t^2 + 250000 + 250000}} \text{ Hz}, \quad -3.029 \leq t \leq 3.029, \tag{4.36}$$

and from (4.5) the Doppler rate for this example is

$$\dot{f}_D(t) = -\frac{3.6 \times 10^{10}}{(3600t^2 + 500000)^{3/2}} \frac{\text{Hz}}{\text{s}}. \tag{4.37}$$

To see the comparison of $f_D(t)$ to $f_{D,LFM}(t)$ for the computed T_a and the given antenna parameters, we can evaluate $\dot{f}_D(t)$ at $t = 0$ which will give the rate of change of the Doppler shift if the signal were an LFM signal. For the parameters in the signal above, we get

$$\alpha_a = -\frac{7.2 \times 10^4}{\sqrt{5 \times 10^5}} = -101.8234 \frac{\text{Hz}}{\text{s}}. \tag{4.38}$$

A plot of the actual Doppler shift compared to the LFM equivalent is illustrated in figure 4.7. In the figure, the dashed red line is the time vs. frequency plot for the LFM signal and the blue line is the time vs. frequency plot for the actual induced signal. From figure 4.7 it is easily seen that with the antenna parameters defined the bandwidth of the induced signal from an isotropic antenna is just slightly less than that of the LFM approximation, thus the bandwidth of the induced signal is upper bounded by the bandwidth of the LFM approximation. However, for wider beamwidths, the difference between $f_D(t)$ and $f_{D,LFM}(t)$

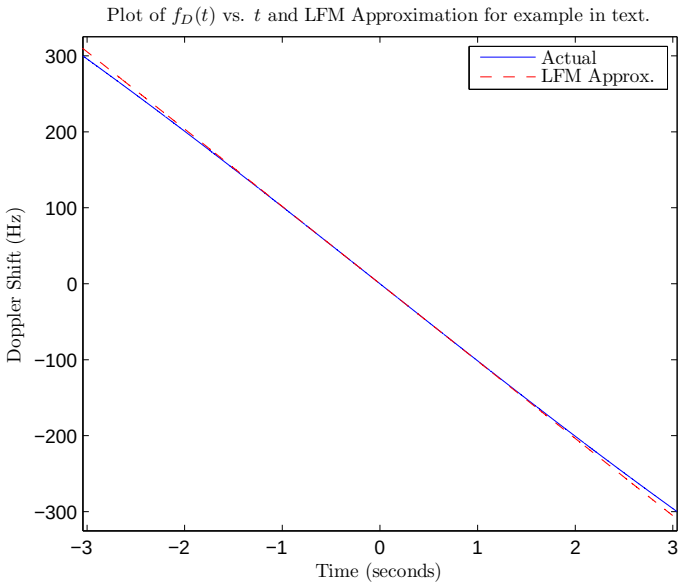

Fig. 4.7: Illustration of the actual induced Doppler shift for the parameters given in the text versus the LFM approximation.

becomes non-trivial. A plot of the induced signal defined in (4.19) compared to the isotropic antenna equivalent (also including propagation loss) for the time duration of the synthetic aperture is illustrated in figure 4.8 and the normalized spectrum of both signals is shown in figure 4.9. The solid red vertical lines in figure 4.9 illustrate the bandwidth as determined by (4.35) and the dashed red lines indicate the bandwidth that is usually derived for the azimuth signal. Note that taking into account the propagation loss does not significantly affect the spectrum (even for large beamwidths) because it varies so slowly.

The typically derived bandwidth is down only -8 dB and aliasing is likely to be more noticeable in a pulsed system that uses this threshold for determining the PRF. To illustrate this, consider the induced signal with the antenna modulation and propagation loss from the example above. Part of the SAR image formation process is to compress the induced azimuth signal using the matched filter derived for it. Figure 4.10 illustrates the output of the matched filter for the derived bandwidth and the traditionally used bandwidth (and the associated PRF rates). Notice that the output of the matched filter for the traditionally used bandwidth has two peaks that are only -24 dB down from the main peak. If this

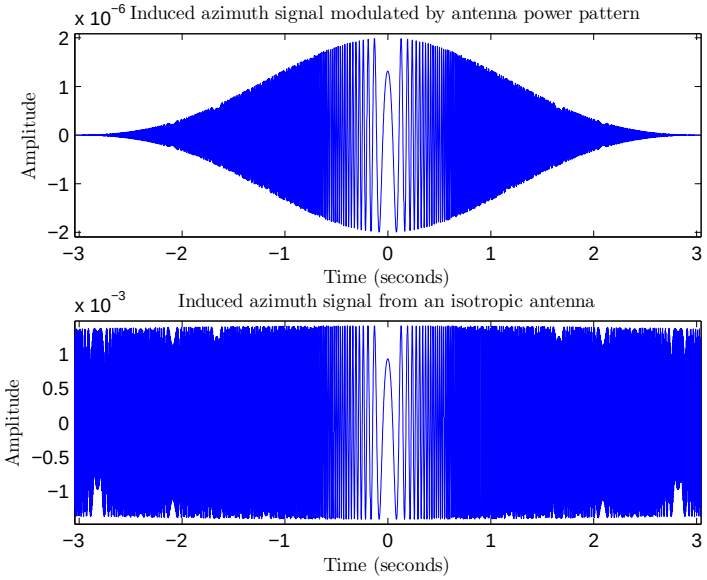

Fig. 4.8: Illustration of the signal induced with the antenna pattern and the signal induced with the isotropic antenna. Both signals include propagation loss.

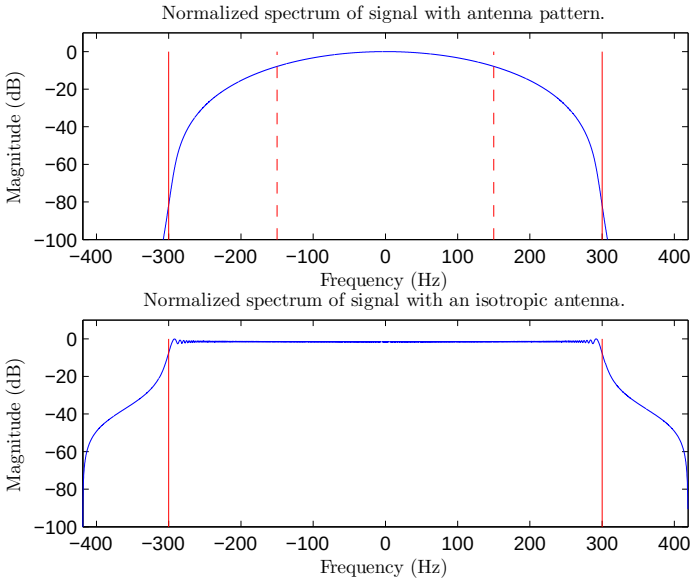

Fig. 4.9: Illustration of the normalized spectrums of the signal induced with the antenna pattern and the signal induced with the isotropic antenna. The solid red vertical lines illustrate the bandwidth as defined in (4.35) and the dashed red lines indicate the traditionally used bandwidth.

were a strong reflector in the image surrounded by weaker reflectors, these two aliased side peaks would be noticeable.

4.5 Induced Discrete Doppler Signal for Pulsed LFM Stripmap SAR

As mentioned in the previous chapter, the PRF rate is related to the bandwidth of the induced azimuth signal, which in turn, is related to the azimuth beamwidth of the antenna. The PRF rate is also limited by the furthest range that is to be imaged; all the samples from a transmitted pulse must be collected before another pulse is transmitted in order to avoid range ambiguities.

Assume that the round trip delay to the furthest range is less than the PRI, then the PRF can be selected as the bandwidth of the induced azimuth signal. To be explicit, setting the PRF rate equal to the bandwidth gives

$$PRF = \frac{4v}{L}. \tag{4.39}$$

The reciprocal of the PRF is the PRI, which is also denoted as T; thus,

$$T = PRI = \frac{L}{4v}. \tag{4.40}$$

Using this, the k^{th} pulsing location for an ideal stripmap flight path is

$$\mathbf{x}(kT) = (v(kT), 0, h). \tag{4.41}$$

It can be seen from this equation that the spacing between pulses is $vT = L/4$.

Let the transmitted signal be the pulsed LFM signal as defined in (2.7). Let there be only a single ideal reflector located at $\mathbf{u}_0^i = (0, y_0^i, 0)$ and let τ_k denote the round-trip delay from the k^{th} pulse to the reflector. Then, modifying (3.46) for a pulsed LFM stripmap SAR

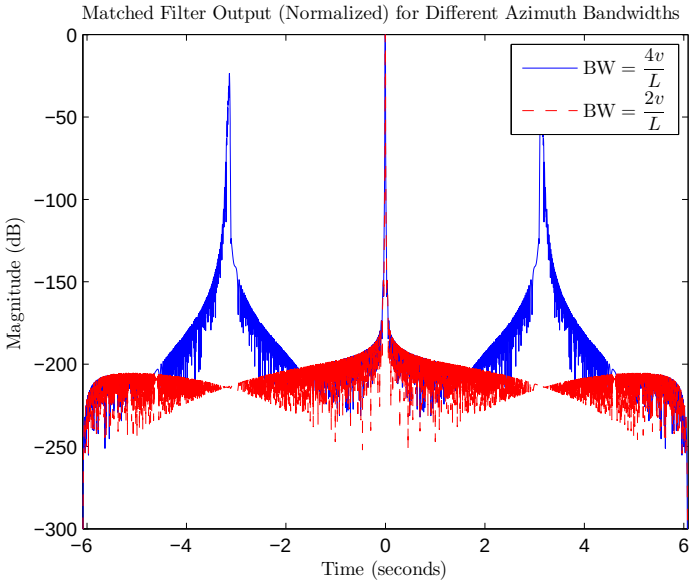

Fig. 4.10: Illustration of the matched filter outputs for the derived bandwidth and the traditionally used bandwidth. Notice that the matched filter output of the traditionally used bandwidth has two aliased peaks that are only -24 dB down from the main peak.

system and including propagation loss gives

$$r_C(t) = \sum_k \frac{\mathcal{C}}{R^4(kT)} a(\theta(kT), \phi(kT)) e^{-j2\pi f_c \tau_k} \left(w(t - kT - \tau_k) e^{j\pi\alpha(t-kT-\tau_k)^2} \right). \tag{4.42}$$

Equation (4.42) can be dissected into two parts; the first is a scaling and phase term that only depends on k and the second is the transmitted signal displaced in range, which depends on both k and t. If we denote the first term as $\tilde{r}(k)$, we can rewrite (4.42) as

$$r_C(t) = \sum_k \tilde{r}(k) \left(w(t - kT - \tau_k) e^{j\pi\alpha(t-kT-\tau_k)^2} \right), \tag{4.43}$$

where (to be explicit)

$$\tilde{r}(k) = \frac{\mathcal{C}}{R^4(kT)} a(\theta(kT), \phi(kT)) e^{j2\pi f_c \tau_k} \tag{4.44}$$

$$= \frac{\mathcal{C}}{R^4(kT)} a(\theta(kT), \phi(kT)) e^{-j\frac{4\pi}{\lambda} R_0(kT)}. \tag{4.45}$$

Notice that (4.45) is just a sampled version of (4.19). Thus, the induced azimuth signal for a pulsed LFM stripmap SAR system is a discrete signal, hence the importance of ensuring the PRF is determined carefully.

4.6 Resolution Limits

It was briefly mentioned in section 2.5 that two reflectors were resolvable in range if they are separated in time by T_p' seconds, where T_p' is the time duration of the first zero-crossings on either side of the mainlobe of the compressed pulse. Using this definition of T_p' leads to a conservative estimate of the resolution. As a lower bound on the range resolution, it is often found in other SAR developments that T_p' is defined from the 3-dB points on either side of the mainlobe of the compressed pulse [6, 13, 15]. Using the lower bound on the range resolution, T_p' is defined as

$$T_p' \approx \frac{1}{BW_r}, \tag{4.46}$$

where BW_r is the bandwidth of the transmitted pulse. If we sample at the bandwidth, $T_s = 1/BW_r$, and using the definition of T_p' in (2.44), the range resolution is computed as

$$\begin{aligned} \Delta R_r &= \frac{c}{2BW_r} \\ &= \frac{cT_s}{2}. \end{aligned} \tag{4.47}$$

With the stated assumptions, (4.47) says that every range sample corresponds to a resolvable reflector in range.

An important thing to note is that (4.47) is the resolution in *range*, which is equally spaced, not the resolution on the ground. The range resolution, ΔR_r, is a small interval in range and to get the equivalent ground resolution, each endpoint of ΔR_r must be mapped to the ground. The ground ranges from the n^{th} sample and the $(n+1)^{th}$ sample are computed

from (3.38). Thus, the n^{th} ground resolution cell is

$$\begin{aligned} \Delta R_g(n) &= R_g(n+1) - R_g(n) && (4.48)\\ &= R_{n+1}\sin(\gamma_{n+1}) - R_n\sin(\gamma_n) && (4.49)\\ &= \frac{c}{2}\left((n+1)T_s\sin(\gamma_{n+1}) - nT_s\sin(\gamma_n)\right), && (4.50) \end{aligned}$$

where γ_i is the incidence angle that corresponds to the i^{th} range sample. From (4.50) it is evident that the ground resolution is not equally spaced. It is interesting to note that if $R_g \to \infty$, then $\Delta R_g \to \Delta R_r$. In other words, the ground resolution asymptotically approaches the range resolution for large ground ranges. A common approximation that is found in the literature for stripmap SAR is

$$\Delta R_g = \frac{\Delta R_r}{\sin(\gamma_n)}. \tag{4.51}$$

The geometry for determining the ground range resolution is illustrated in figure 4.11.

Equation (4.47) gives a fairly good estimate for the range resolution. However, to get a more realistic lower bound on the azimuth resolution, we should define T_a' using half the bandwidth of the induced azimuth signal (it was necessary to define the azimuth bandwidth as we did for the sake of avoiding aliasing, but for defining a realistic lower bound on the azimuth resolution, half the bandwidth should be used). Using half the azimuth bandwidth gives

$$\begin{aligned} T_a' &\approx \frac{2}{BW_{Az}} && (4.52)\\ &\approx \frac{2L}{4v} && (4.53)\\ &\approx \frac{L}{2v}. && (4.54) \end{aligned}$$

From this definition of T_a', the approximation to the azimuth resolution becomes

$$\Delta R_a = vT_a' \tag{4.55}$$

$$= \frac{L}{2}. \tag{4.56}$$

Equation (4.56) is the definition of the azimuth resolution (for a sensor mounted to an airplane) that is found in most of the literature on SAR [13, 15].

4.7 Basic Steps for Image Formation

At a high level only three steps are needed in order to produce a focused stripmap SAR image: range compression, data alignment, and azimuth compression. Range compression has already been discussed and hints have been made about azimuth compression, but there is a necessary step called range cell migration correction (RCMC) that needs to be performed before azimuth compression. These processing steps are best illustrated in an example where the processing is done on the PSR of a single ideal reflector.

In this example the antenna beam pattern and the propagation loss will be neglected to simplify the expressions. Also, assume there is only a single ideal reflector in the scene

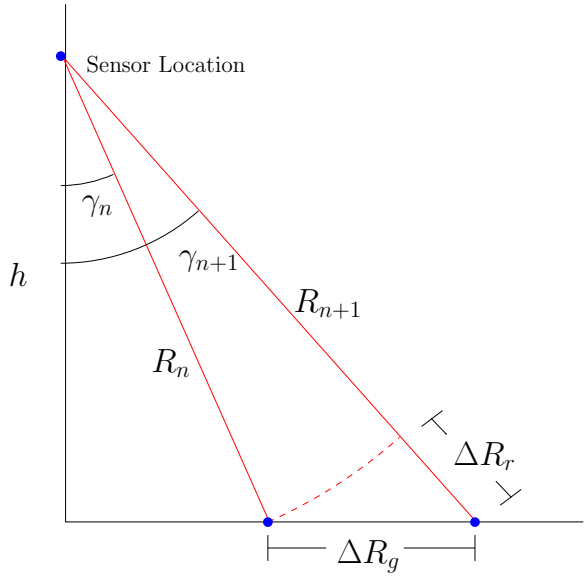

Fig. 4.11: Illustration of the geometry for finding the ground range resolution from the slant range resolution.

that the SAR sensor is imaging. Let the k^{th} transmitted pulse be given by (2.7), which is repeated here for convenience,

$$s(k,t) = w(t-kT)\cos\left(2\pi f_c(t-kT) + \pi\alpha(t-kT)^2 + \psi_k\right). \tag{4.57}$$

The quadrature demodulated reflected signal from this reflector for the k^{th} transmitted pulse is given by (2.21) (which is repeated here for convenience)

$$r(k,t) = w(t-kT-\tau_k)e^{-j2\pi f_c\tau_k}e^{j\pi\alpha(t-kT-\tau_k)^2}. \tag{4.58}$$

The received signal is sampled at $t = (N_dT_s + nT_s + kT_p)$ for $0 \leq n \leq N_n - 1$, giving

$$d(k,n) = w((N_d+n)T_s - \tau_k)e^{-j2\pi f_c\tau_k}e^{j\pi\alpha((N_d+n)T_s-\tau_k)^2}. \tag{4.59}$$

The sampled received signal for the k^{th} pulse can be interpreted as the k^{th} row of the two-dimensional array which contains the samples of the PSR of the single ideal reflector. The real part of the PSR of the single reflector is illustrated in figure 4.12 for several pulses.

The data after being range compressed with the causal matched filter

$$h(n) = w(T_p - nT_s)e^{j\pi\alpha(T_p-nT_s)^2} \tag{4.60}$$

has the form

$$\bar{d}(k,n) = e^{-j2\pi f_c\tau_k}e^{-j\pi\alpha T_p((N_d+n)T_s-\tau_k)}\frac{\sin(\pi\alpha((N_d+n)T_s-\tau_k)(T_p-|(N_d+n)T_s-\tau_k|))}{\pi\alpha((N_d+n)T_s-\tau_k)}. \tag{4.61}$$

The (zoomed-in) real part of the range compression step is illustrated in figure 4.13.

The range compressed data has a hyperbolic curvature in the data array. This curvature must be accounted for in order to properly focus the data in azimuth. One technique is to perform an interpolation (RCMC) in order to properly align the data in azimuth so

the azimuth processing can be accomplished down the columns of the data array. The (zoomed-in) data after RCMC is illustrated in figure 4.14.

The first phase term in (4.61) is a sampling of (3.34) and is what defines the induced azimuth signal. An azimuth matched filter is constructed from this signal, then the data is azimuth compressed to produce the (zoomed-in) focused image in figure 4.15. There is some "smearing" around the reflector in the image reconstruction. This smearing is the IPI and is inherent in the most commonly-used SAR processing algorithms.

This was an example for a single reflector under the illumination of the antenna. An actual SAR image is the superposition of all such reflectors under the illumination of the antenna, but the essence of the processing remains the same.

4.8 Image Formation Algorithms

Several algorithms exist to process SAR data. There are three main classes of algorithms: frequency domain methods, time-domain methods, and "inverse problems" methods.

There are many different frequency-domain algorithms for forming stripmap SAR images, such as the range-doppler algorithm (RDA) [13, 15], the ω-k algorithm [15], and the chirp-scaling algorithm (CSA) [15, 21, 22]. The frequency-domain algorithms have low computational complexity because they utilize the efficient FFT algorithms. The frequency domain algorithms primarily differ in how the RCMC is accomplished. Some of the approximations, such as having a narrow beam in azimuth or the range to the scene, will determine which frequency domain algorithm will be better suited for a data set. A couple assumptions and limitations of the frequency-domain algorithms are that the vehicle is traveling at a constant velocity and pulses are transmitted at equally spaced intervals (this justifies the use of the FFT) and that the vehicle follows a perfectly straight flight path so that no uncompensated motion is present. A drawback to the frequency domain methods is that all the processing is done globally. This makes motion error along the flight path difficult to account for and hence the focusing in some areas might not be as good as in others. The frequency-domain algorithms do not explicitly account for noise in the system.

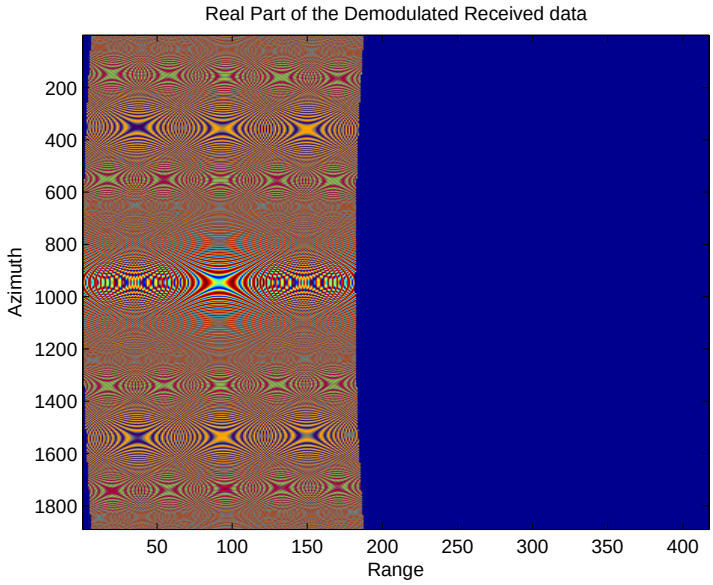

Fig. 4.12: Illustration of the real part of the PSR from a single ideal point reflector.

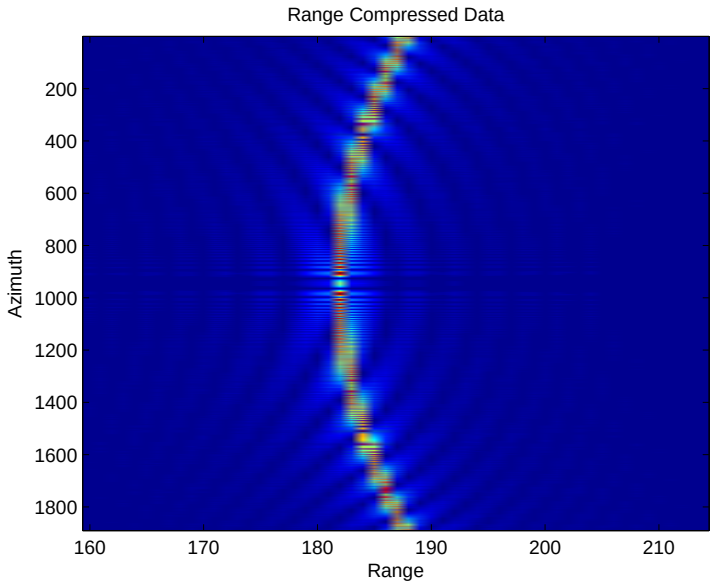

Fig. 4.13: Illustration of the (zoomed-in) real part of the data after being range compressed.

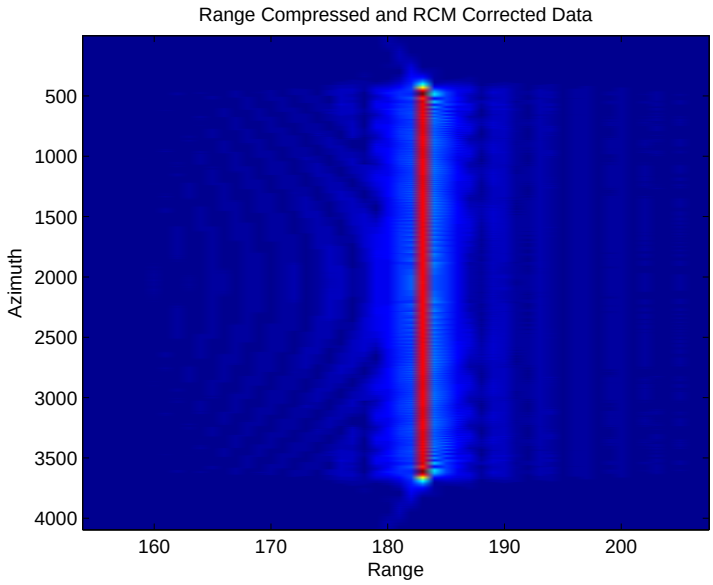

Fig. 4.14: Illustration of "aligning" the data for azimuth compression.

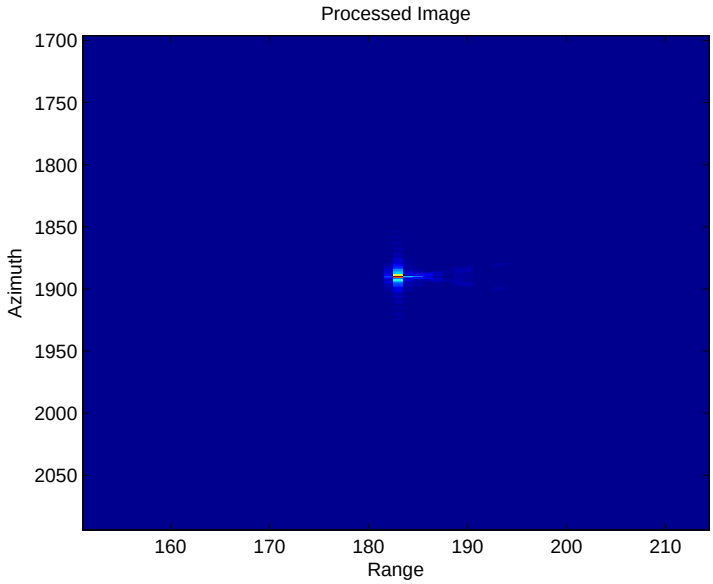

Fig. 4.15: Illustration of the focused reconstruction of the ideal point reflector.

There are also many different time-domain algorithms for forming stripmap SAR images, such as the range-stacking algorithm [23], time-domain correlation algorithm [23], and convolution back-projection (CBP) [23–25]. The advantages of using a time-domain algorithm is that such things as unequally spaced pulsing intervals and compensating for motion is easily handled, also a digital elevation model (DEM) can be used to improve focusing. The trade-off is that the computational complexity is increased. A lot of effort has gone into reducing the computational complexity of time-domain algorithms and algorithms such as fast-factorized CBP have emerged [26, 27]. While these are faster, they still have trade-offs of their own. It seems that in order to get the most focused image, you must be willing to accept the computational complexity.

A common result from both the frequency and the time domain methods is the considerable IPI that is noticeable around bright reflectors. This IPI manifests itself as a large "star-like" pattern around the bright reflectors. The IPI can mask other reflectors that are nearby and typically makes urban scenes, where there are a lot of bright reflectors, very difficult to analyze. The IPI can often be reduced by windowing the data, however, this has the effect of reducing the resolution of the image.

The final class of imaging algorithms are the "inverse-problems" methods. Most of the work in this area has been done for spotlight SAR [10, 11, 28]. These approaches are model-based, that is they model the data acquisition of the SAR sensor, then they invert the model to recover the ground reflectivity. These methods allow for the explicit modeling of everything that is known about the data acquisition such as GPS data, digital elevation models (DEM), and the nature of the scene being imaged (sand, grass, etc.). Hence, these are not just turn-the-crank processing algorithms. In fact, these are ground reflectivity estimation methods where the reflectivity is being estimated in the presence of noise and where prior information on the scene can be explicitly accounted for. These methods offer the best image quality of all classes of algorithms because the model accounts for the IPI, thus the IPI can be removed. This makes such things as automatic target recognition (ATR) much easier [10]. However, these methods are very computationally complex.

Chapter 5

Forward Model for Pulsed LFM Stripmap SAR

The contribution in this chapter is the development of a forward model for stripmap SAR, which models the baseband quadrature demodulated data that is collected from the SAR sensor and assumes the reflected signal is sampled in the presence of circularly symmetric additive white Gaussian noise (AWGN). It is also shown that this model can be written as a set of equations that is linear in the parameters describing the ground reflectivity. This linear forward model forms the basis for all other research in this dissertation.

It is also shown that the forward model has a signal component and a noise component. Based on these signal components, a discussion on the signal-to-noise ratio (SNR) is given.

Finally, it is shown that the forward model can be used for arbitrary ground regions of interest (ROI). It is also discussed that a larger enclosing region, called the region of interest closure (ROIC), is needed to form an unbiased image of the ROI.

5.1 Forward Model for Stripmap SAR

The forward model for stripmap SAR models the baseband quadrature demodulated data that is collected from the SAR sensor. The PSR illustrated in figure 4.12 is a simple example of the forward model of a single ideal unit point reflector. An actual SAR data set is the superposition of the PSRs from all reflectors, weighted by the antenna beam pattern and the complex reflectivity of the reflectors under the illumination of the antenna. A more accurate equation for the forward model of a single ideal reflector with arbitrary complex reflectivity $g(\mathbf{u}_0^i)$ at ground location $\mathbf{u}_0^i = (x_0^i, y_0^i, z_0^i)$ is given by sampling (4.42)

at $t = (n + N_d)T_s + kT$, which is (neglecting noise)

$$\begin{aligned} \tilde{d}(k, n, \mathbf{u}_0^i) &= b(k, \mathbf{u}_0^i) e^{-j2\pi f_c \tau_{k,0}} \left(w((N_d + n)T_s - \tau_{k,0}) e^{j\pi\alpha((N_d+n)T_s - \tau_{k,0})^2} \right) g(\mathbf{u}_0^i) \quad (5.1) \\ &= f(k, n, \mathbf{u}_0^i) g(\mathbf{u}_0^i), \quad (5.2) \end{aligned}$$

where

$$b(k, \mathbf{u}_0^i) = \mathcal{C} \frac{a(\theta(kT), \phi(kT))}{R_0^4(kT)}. \quad (5.3)$$

Equation (5.2) factors nicely into two parts; the ground reflectivity g and a function f that contains the sampled transmitted signal, weighted by the propagation loss and the antenna, and the sampled azimuth signal.

Equations (4.47) and (4.56) give lower bounds on the obtainable azimuth and range resolution for a SAR system. It is natural to define an $(N_a \times N_r)$ reconstruction array, with cell sizes given by the resolution in each direction that the formed image will occupy, where N_a is the number of rows in the array and corresponds to the azimuth direction and N_r is the number of columns in the array and corresponds to the range direction. It is not necessary to define the reconstruction grid in this manner; equation (3.42) shows that information on all the reflectors under the illumination of the antenna is available in the data. Thus, as will be shown in a later section, an arbitrary ground patch can be reconstructed. However, for the current development, let the reconstruction grid be rectangular. If $\mathbf{u}_{a,r}^i = (x_{a,r}^i, y_{a,r}^i, z_{a,r}^i)$ where $0 \leq a \leq N_a - 1$ and $0 \leq r \leq N_r - 1$ denotes the location of the center of the $(a, r)^{th}$ reconstruction cell, then $g(\mathbf{u}_{a,r}^i)$ denotes the ground reflectivity for the cell at $\mathbf{u}_{a,r}^i$. Notice that the definition of $\mathbf{u}_{a,r}^i$ does not assume a flat earth model; but it does assume that the coordinates are known (*i.e.* from a DEM).

The forward model, based on the reconstruction array, is the superposition of all the PSRs of the ground locations that the reconstruction array cells represent. Thus, the

forward model is

$$d(k,n) = \sum_{a,r} \tilde{d}(k,n,\mathbf{u}^i_{a,r}) \tag{5.4}$$

$$= \sum_{a,r} f(k,n,\mathbf{u}^i_{a,r}) g(\mathbf{u}^i_{a,r}), \tag{5.5}$$

where $0 \leq a \leq N_a - 1$ and $0 \leq r \leq N_r - 1$ index the rows and columns of the array.

Let N_k denote the number of pulses transmitted and let N_n denote the number of samples taken from each pulse. The two-dimensional array $d(k,n)$ can be rewritten as a single $(N_k N_n \times 1)$ vector by linearizing the indexing of the elements as $\mathbf{d}_i = d(k_0, n_0)$ where $i = k_0 N_n + n_0$ for the given ranges of n and k. The mathematical operation for this is

$$\mathbf{d} = \text{vec}(d(k,n)^T). \tag{5.6}$$

A similar operation can be done with the indexing of the two-dimensional reconstruction array giving $\mathbf{g}_j = g(\mathbf{u}_{a_0,r_0})$ where $j = a_0 N_r + r_0$ and yields the vectors $\mathbf{g}$. Similarly, the four-dimensional structure $f(k,n,\mathbf{u}_{a,r})$ can be written as the matrix whose $(i,j)^{th}$ entry is

$$[\mathcal{F}]_{i,j} = f(k_0, n_0, \mathbf{u}^i_{a_0,r_0}), \tag{5.7}$$

where the indexing for i and j is the same as above. Combining these results, (5.5) can be written as

$$\mathbf{d} = \mathcal{F}\mathbf{g}. \tag{5.8}$$

Taking a closer look at the structure of the data matrix $\mathcal{F}$ shows the j^{th} column is

$$[\mathcal{F}]_{:,j} = \text{vec}(f(k,n,\mathbf{u}^i_{a_0,r_0})^T), \tag{5.9}$$

which is the linearized index of the two-dimensional PSR of the reflector located at $\mathbf{u}^i_{a_0,r_0}$. Thus, (5.8) states that the collected quadrature demodulated data is a linear combination

of the PSRs.

Another way to view the data matrix is to view it as the stack of N_k $(N_n \times N_a N_r)$ submatrices

$$\mathcal{F} = \left[\begin{array}{c} \mathcal{F}_1 \\ \hline \vdots \\ \hline \mathcal{F}_{N_k} \end{array}\right], \tag{5.10}$$

where the columns of the k^{th} submatrix, $\mathcal{F}_k$, model the demodulated reflected signals from all reflectors in the reconstruction array from the k^{th} transmitted pulse.

Note that selecting the size of $\mathbf{g}$ to be the same size as $\mathbf{d}$ (*i.e.* $N_a = N_k$ and $N_r = N_n$) implies that $\mathcal{F}$ is a square matrix. If $\mathbf{g}$ is made larger than $\mathbf{d}$, then $\mathcal{F}$ is wide and has a nontrivial null-space. The implication of this is that the reconstruction grid cannot be made finer than the collected data will support.

It is important to note some of the assumptions for the model in (5.8). It is assumed that the reflectors for each cell are ideal, that is that the reflectivity does not change with the aspect angle. It is also assumed that the reflectors are not correlated with each other. In actuality, there are many reflectors in a given cell and the changing aspect angle gives rise to a Rayleigh fading effect due to the constructive/destructive interference of the many reflectors contributing to a cell. This effect becomes less important the higher the bandwidth is in azimuth and range. While the assumptions that the reflectors are ideal and are not correlated are bold assumptions to make, they are common to the other SAR processing algorithms and modeling such phenomena would greatly increase the complexity of the model. Models with higher fidelity can be very useful to have, however they are not always the most practical to implement.

5.1.1 Circularly Symmetric Additive White Gaussian Noise

So far, the fact has been neglected that the received signal is sampled in the presence of noise. There are two major sources of noise, thermal noise and clutter noise. It is safe to

assume that the thermal noise is additive white Gaussian noise (AWGN). The clutter noise represents returns that have not been modeled. In general the clutter noise is correlated; however deriving the proper model for the distribution of the clutter noise is beyond the scope of this dissertation. In this chapter it will be assumed that the clutter is AWGN and independent of the thermal noise; thus it can be lumped with the thermal noise.

Figure 5.1 illustrates the power spectral density of a white noise processes through the quadrature demodulator. (Figure 5.1 is a compact version of figure 2.3.) The autocorrelation function of the white noise process is

$$R_\eta(\tau) = \frac{N_0}{2}\delta(\tau), \tag{5.11}$$

where τ represents the time lag. The noise process at point (d) is at baseband and the real and imaginary parts of the signal are the baseband process scaled by the sine and cosine mixers (assuming ideal filters and mixers); therefore the signal at (d) is circularly symmetric. The autocorrelation function at (e) is computed from the inverse discrete-time Fourier transform of the spectrum

$$\begin{aligned} R_\eta(k) &= \int_{-\frac{BW}{2f_s}}^{\frac{BW}{2f_s}} \frac{N_0}{T_s} e^{j2\pi f k} df & (5.12) \\ &= BW N_0 \operatorname{sinc}\left(\frac{\pi BW}{f_s} k\right). & (5.13) \end{aligned}$$

Notice that if $BW = f_s$ in (5.13), then the autocorrelation function becomes

$$R_\eta(k) = \frac{N_0}{T_s}\delta(k), \tag{5.14}$$

where k is the lag (in samples). Thus, with the bandwidth of the bandpass filter equal the sampling frequency, the sampled process is white as well. If we select the bandwidth of the bandpass filter equal to the sampling rate, then the model for the noise is circularly

symmetric AWGN and the linear model for the SAR data is

$$d(k,n) = \sum_{a,r} g(\mathbf{u}^i_{a,r}) f(k,n,\mathbf{u}^i_{a,r}) + \eta(k,n), \tag{5.15}$$

which can also be written as

$$\mathbf{d} = \mathcal{F}\mathbf{g} + \boldsymbol{\eta}. \tag{5.16}$$

5.1.2 Signal-to-Noise Ratio

The model for the SAR data in (5.16) has a signal component and a noise component. To be specific, the components are

$$\mathbf{d} = \underbrace{\mathcal{F}\mathbf{g}}_{\text{signal}} + \underbrace{\boldsymbol{\eta}}_{\text{noise}}. \tag{5.17}$$

Using these components of the data, the signal-to-noise ratio (SNR) is computed as

$$SNR = \frac{E\left\{\mathbf{g}^H \mathcal{F}^H \mathcal{F}\mathbf{g}\right\}}{E\left\{\boldsymbol{\eta}^H \boldsymbol{\eta}\right\}}, \tag{5.18}$$

where $E\{\cdot\}$ is the expectation operator. Using that the ground reflectivity is uncorrelated, that $\mathcal{F}$ is deterministic, and that $\mathbf{x}^H\mathbf{x} = \mathrm{tr}(\mathbf{x}\mathbf{x}^H)$ where $\mathrm{tr}(\cdot)$ is the trace of a matrix (the sum of the diagonal elements), (5.18) becomes

$$SNR = \frac{\mathrm{tr}\left(\mathcal{F}E\left\{\mathbf{g}\mathbf{g}^H\right\}\mathcal{F}^H\right)}{\mathrm{tr}\left(E\left\{\boldsymbol{\eta}\boldsymbol{\eta}^H\right\}\right)} \tag{5.19}$$

$$= \frac{T_s \mathrm{tr}\left(\sigma_g^2 \mathcal{F}\mathcal{F}^H\right)}{\mathrm{tr}(N_0 I)}. \tag{5.20}$$

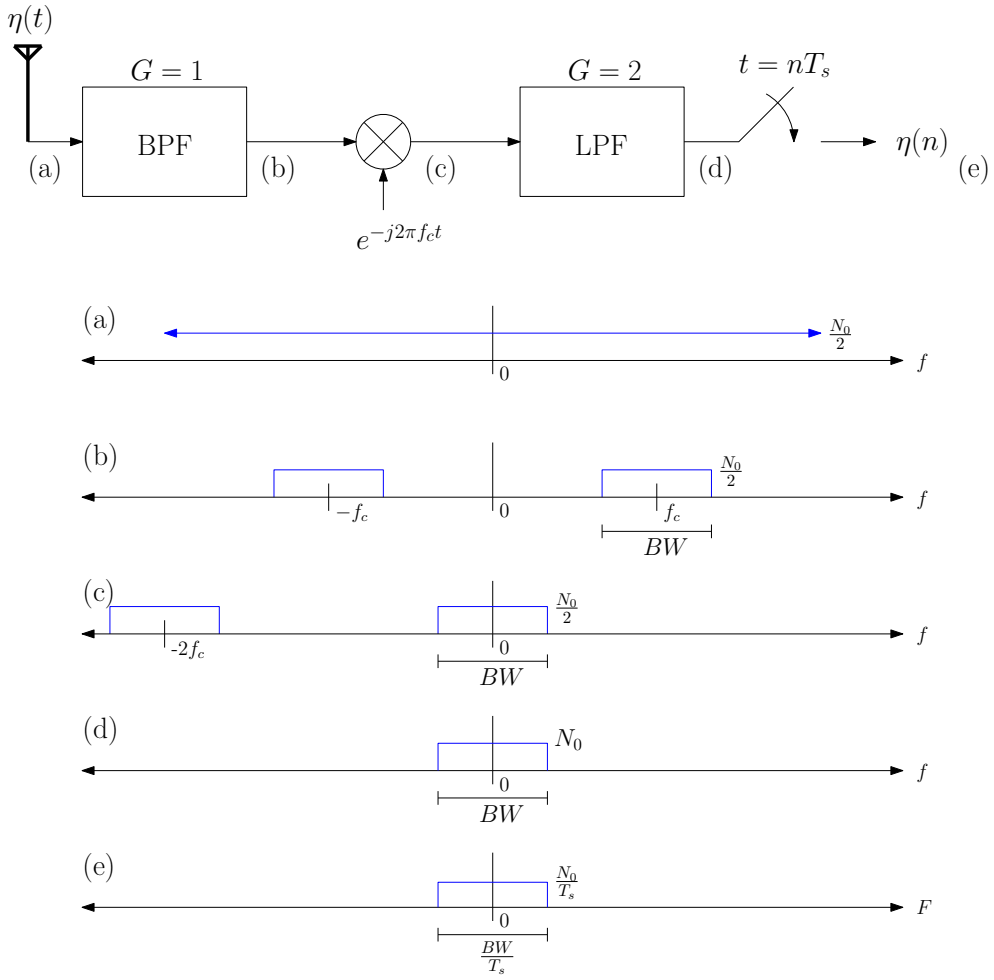

Fig. 5.1: Illustration of the power spectral density of a white noise process through each stage of the quadrature demodulator (including the A/D converter).

Using that the arguments of the trace of a matrix are cyclic invariant, that

$$\sigma_\eta^2 = \frac{N_0}{T_s}, \tag{5.21}$$

and that the size of the identity matrix is $N_n N_k \times N_n N_k$, (5.20) becomes

$$SNR = \frac{\sigma_g^2 ||\mathcal{F}||_F^2}{\sigma_\eta^2 N_n N_k}, \tag{5.22}$$

where $||\cdot||_F$ is the Frobenius norm of a matrix.

From (5.22), the variance of the additive Gaussian noise in (5.15) for a given SNR (expressed in dB) is computed as

$$\sigma_\eta^2 = \frac{\sigma_g^2 ||\mathcal{F}||_F^2}{10^{\frac{SNR_{dB}}{10}} N_n N_k}. \tag{5.23}$$

5.2 Region of Interest

As previously mentioned, the reconstruction grid for the image can be chosen arbitrarily. The reconstruction area can be the entire image or a smaller region of interest (ROI), denoted as $\mathcal{R}$. If a ROI is chosen that is less than the entire image, then it is necessary to identify all of the data of interest (DOI), denoted as $\mathcal{D}$, that corresponds to the ROI. The data selected in $\mathcal{D}$ also contains returns from the neighbors of the ROI (as is illustrated for a single data sample in figure 3.5 and is stated in (5.15)). In order to form the best possible, unbiased, image (based on algorithms that use the forward model) for the ROI, it is necessary to identify all of the ground points that contribute to $\mathcal{D}$. This set is the region of interest closure (ROIC), denoted by $\bar{\mathcal{R}}$ and knowing it will give the values of a and r for the summations in (5.15). An illustration of the ROI, DOI, and ROIC is given in figure 5.2.

In order to properly form the ROIC, the pulse duration of the transmitted signal must be known and the antenna threshold must be defined; for this development, let us continue to use ϑ_N. Then for each location the sensor transmits a pulse (accounting for the attitude of the vehicle), check to see if any part of the ROI is within the antenna beam by comparing the

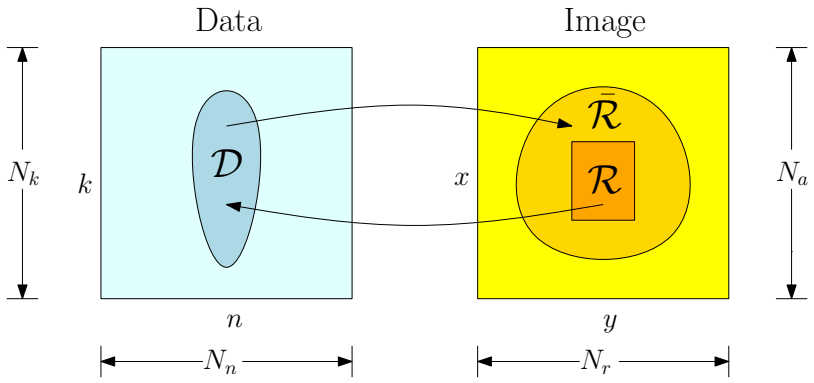

Fig. 5.2: Illustration of the concept of ROI, DOI, and ROIC for an arbitrary reconstruction grid. The ROI gives rise to the DOI, the DOI also contains data from the ROIC.

output of (3.16) with the antenna threshold. If no part of the ROI is under the illumination of the antenna beam (for the given threshold), then there is no contribution to the ROIC from that pulse. However, if any part of the ROI is under the illumination of the antenna beam, then every cell within the portion of the annulus illustrated in figure 3.5 for the given antenna threshold will contribute to the ROIC. All of the cells that are in the ROIC will form the vector $\mathbf{g}$.

5.3 Summary

The forward model for pulsed stripmap SAR was developed in this chapter. It was shown that this model is linear in the ground reflectivity parameters. It was also shown that the thermal AWGN at the front-end of the receiver becomes circularly symmetric AWGN after passing through the quadrature demodulator. Based on the circularly symmetric AWGN, the forward model has the interpretation of the linear statistical model. It is also shown that the signal-to-noise ratio can be expressed in terms of the forward model. Finally, it was shown that the forward model can be defined for an arbitrary region of interest.

Chapter 6

Maximum Likelihood Image Formation

The contribution to SAR in this chapter is the maximum likelihood (ML) imaging method derived from the forward model for stripmap SAR. It is also shown that the convolution back-projection algorithm is the first of two steps involved in the ML image formation. A demonstration of the ML imaging method on simulated data is also shown in this chapter. Also, a short discussion is also provided on the Cramér-Rao lower bound. Finally, the chapter concludes with some insights that the ML imaging method provides for system design.

6.1 Likelihood Function

If the assumption is made that the ground reflectivity is deterministic (but unknown) and the noise is circularly symmetric AWGN, then (5.16) has a statistical interpretation. If the noise is distributed as

$$\boldsymbol{\eta} \sim \mathcal{N}\left(0, \frac{N_0}{T_s} I\right), \tag{6.1}$$

then the model for the collected data has the distribution

$$\mathbf{d} \sim \mathcal{N}\left(\mathcal{F}\mathbf{g}, \frac{N_0}{T_s} I\right). \tag{6.2}$$

If the ground reflectivity vector $\mathbf{g}$ is thought of as a parameter vector, then a likelihood function can be written for the observed data vector [29]

$$\ell(\mathbf{g}, \mathbf{d}) = f_{\mathbf{D}|\mathbf{G}}(\mathbf{d}|\mathbf{g}). \tag{6.3}$$

The distribution of $\mathbf{d}$ given $\mathbf{g}$ is in the exponential family, therefore it is more fitting to work with the log-likelihood function

$$\begin{aligned} \Lambda(\mathbf{g}, \mathbf{d}) &= \ln(f_{\mathbf{D}|\mathbf{G}}(\mathbf{d}|\mathbf{g})) && (6.4) \\ &= \ln(C) - \frac{T_s}{N_0}||\mathbf{d} - \mathcal{F}\mathbf{g}||_2^2, && (6.5) \end{aligned}$$

where C is the normalizing constant which makes $f_{\mathbf{D}|\mathbf{G}}(\mathbf{d}|\mathbf{g})$ a distribution.

The maximum likelihood (ML) estimate of the ground reflectivity is given by the vector $\mathbf{g}_{\mathrm{ML}}$ which maximizes the likelihood function (or log-likelihood function since log is monotonic). Maximizing (6.5) is equivalent to minimizing

$$J = ||\mathbf{d} - \mathcal{F}\mathbf{g}||_2^2. \tag{6.6}$$

The maximum likelihood estimate for the ground reflectivity $\mathbf{g}$ is obtained as

$$\mathbf{g}_{\mathrm{ML}} = \arg\min_{\mathbf{g}} ||\mathbf{d} - \mathcal{F}\mathbf{g}||_2. \tag{6.7}$$

This is a least-squares problem and the solution is the vector $\mathbf{g}_{\mathrm{ML}}$ that solves the so-called normal equations

$$\mathcal{F}^H\mathcal{F}\mathbf{g}_{\mathrm{ML}} = \mathcal{F}^H\mathbf{d}. \tag{6.8}$$

In order for $\mathcal{F}^H\mathcal{F}$ to be invertible, $\mathcal{F}$ must either be square or tall and have full column rank. Unless there are two reflectors with identical PSRs in the collected data (*i.e.* two linearly dependent columns of $\mathcal{F}$), $\mathcal{F}$ will have full column rank. The conditioning of $\mathcal{F}^H\mathcal{F}$ is controlled by the system parameters such as the bandwidth of the transmitted signal, the antenna beam pattern, the resolution of the reconstruction array, etc. If the system is designed such that $\mathcal{F}^H\mathcal{F}$ is well conditioned, then the ML ground reflectivity estimate is

$$\mathbf{g}_{\mathrm{ML}} = (\mathcal{F}^H\mathcal{F})^{-1}\mathcal{F}^H\mathbf{d}. \tag{6.9}$$

Forming the normal equations in (6.8) is one of the two critical steps in the ML image formation. The p^{th} element of the cross-correlation vector in (6.8) (which corresponds to the partial reconstruction of the image in the $(a_0, r_0)^{th}$ element of the reconstruction array) is given by

$$\begin{aligned} [\mathcal{F}^H \mathbf{d}]_p &= \sum_k \sum_n f^*(k, n, \mathbf{u}_p) d(k, n) && (6.10) \\ &= \sum_k b(k, \mathbf{u}_p) e^{j2\pi f_c \tau_{p,k}} \bar{d}(p, k), && (6.11) \end{aligned}$$

where

$$\bar{d}(p, k) = \sum_n w((N_d + n)T_s - \tau_{p,k}) e^{-j\pi\alpha((N_d+n)T_s - \tau_{p,k})^2} d(k, n). \quad (6.12)$$

It is worth examining the processing in (6.12) a little closer. Let $\tau_{p,k} = \gamma_{p,k} T_s$, where $\gamma_{p,k} > 0$ expresses the round-trip delay from the sensor to $\mathbf{u}_p$ for the k^{th} pulse, in terms of the sample rate. This gives

$$\bar{d}(p, k) = \sum_n w((N_d + n - \gamma_{p,k})T_s) e^{-j\pi\alpha((N_d+n-\gamma_{p,k})T_s)^2} d(k, n). \quad (6.13)$$

Let $L = \lfloor T_p/T_s \rfloor + 1$ (where $\lfloor \cdot \rfloor$ is the floor function that rounds down to the nearest integer). Thus the window function $w(nT_s)$ has support for L samples. Using the limits of the window function and the range of the indexing of the data, gives

$$\bar{d}(p, k) = \sum_{n=\max(0, \lfloor \gamma_{p,k} \rfloor - N_d)}^{\min(N_n - 1, \lfloor \gamma_{p,k} \rfloor - N_d + L - 1)} e^{-j\pi\alpha((n + N_d - \gamma_{p,k})T_s)^2} d(k, n). \quad (6.14)$$

Performing the change of variables $q = n + N_d - \gamma_{p,k}$, gives

$$\bar{d}(p, k) = \sum_{q=\max(0, N_d - \lfloor \gamma_{p,k} \rfloor)}^{\min(L-1, N_n - 1 + N_d - \lfloor \gamma_{p,k} \rfloor)} e^{-j\pi\alpha T_s^2 (q)^2} d(k, q - N_d + \lfloor \gamma_{p,k} \rfloor). \quad (6.15)$$

Now, let $\bar{n} = N_d - \lfloor \gamma_{p,k} \rfloor$, then (6.15) becomes

$$\bar{d}(p,k) = \sum_{q=\max(0,\bar{n})}^{\min(L-1,N_n-1+\bar{n})} e^{-j\pi\alpha T_s^2 (q)^2} d(k, q-\bar{n}). \tag{6.16}$$

Let $m = q - \bar{n}$ substituting in this change of variables and using $t^2 = (-t)^2$ gives

$$\bar{d}(p,k) = \sum_{m=\max(0,-\bar{n})}^{\min(L-1-\bar{n},N_n-1)} e^{-j\pi\alpha T_s^2 (-\bar{n}-m)^2} d(k,m). \tag{6.17}$$

Equation (6.17) has the form of a convolution sum

$$\bar{d}(p,k,\bar{n})\big|_{\bar{n}=N_d-\lfloor\gamma_{p,k}\rfloor} = h_r(\bar{n}) * d(k,\bar{n})|_{\bar{n}=N_d-\lfloor\gamma_{p,k}\rfloor}\,, \tag{6.18}$$

where

$$h_r(\bar{n}) = w(\bar{n}) e^{-j\pi\alpha T_s^2 (-\bar{n})^2}, \tag{6.19}$$

is the system that the data is passed through. Equation (6.19) is actually a time-reversed and conjugated baseband version of the signal that is transmitted; thus $h_r(\bar{n})$ is the matched filter to the baseband version of the transmitted signal.

The output of the matched filter that is actually wanted is $\bar{n} = N_d - \gamma_{p,k}$, which can be obtained by interpolating. To be explicit, the *interpolated* matched filter output is

$$\bar{d}(p,k) = \bar{d}(p,k,\bar{n})\big|_{\bar{n}=N_d-\gamma_{p,k}} \tag{6.20}$$

$$= \sum_{m=\max(0,-\bar{n})}^{\min(L-1-\bar{n},N_n-1)} e^{-j\pi\alpha T_s^2 (-\bar{n}-m)^2} d(k,m)\Bigg|_{\bar{n}=N_d-\gamma_{p,k}}. \tag{6.21}$$

This processing accomplishes range matched filtering and also accomplishes the RCMC processing by windowing the data for each p and for each k.

Similarly, it can be shown that (6.11) is the output of the data passed through the system

$$h_a(\bar{k}) = w_a(\bar{k}) b(\bar{k}, \mathbf{u}_p) e^{j2\pi f_c \tau_{p,\bar{k}}}, \tag{6.22}$$

which is a filter matched to the induced azimuth signal. The limits of the window $w_a(\bar{k})$ depend on the azimuth beamwidth of the antenna and range to the reflector at p.

Thus, the product $\mathcal{F}^H \mathbf{d}$ accomplishes range matched filtering, interpolation, and azimuth matched filter; these are exactly the steps of CBP. Hence, CBP is one of the steps in the ML image formation. This is actually not too surprising, since CBP is a two-dimensional correlation algorithm.

The two-dimensional matched filter in (6.10) does not isolate the collected data for the ground reflector at $\mathbf{u}^i_{a_0,r_0}$. The matched filtered data still contains reflections from the neighboring reflectors of $\mathbf{u}^i_{a_0,r_0}$. If the processing stopped and the image formed after computing $\mathcal{F}^H \mathbf{d}$, there would still be noticeable IPI about each reflector (more noticeable about the strong reflectors in the scene) indicating that correlation still exists between reflectors (as in traditional SAR processing).

Solving the normal equations for $\mathbf{g}_{\text{ML}}$ in (6.9) is the other critical step in the ML image formation. Recall the residual blurring (IPI) that was evident in the focused image in figure 4.15. The grammian matrix in (6.9) models that IPI; the off-diagonal entries explain the IPI between pixels that is observed in traditionally focused SAR images. The inversion of the grammian removes the IPI and the resulting image is the optimal image that can be formed under the stated assumptions of the model.

Solving the normal equations is the bulk of the work in the ML estimation algorithm and requires great care because $\mathcal{F}^H \mathcal{F}$ can be ill-conditioned. The size of $(\mathcal{F}^H \mathcal{F})^{-1}$ is the number of elements in $\mathbf{g}$ squared. Matrix inversion is $\mathcal{O}(n^3)$, and in this case n may be *very* large, thus due to limitations on the available amount of memory on any machine that processes SAR images, along with direct matrix inversion stability issues, computing $(\mathcal{F}^H \mathcal{F})^{-1}$ is not done directly on problems of appreciable size. An efficient alternative

method for computing a regularized inverse will be discussed in Chapter 7.

6.2 Simulated Results

This section demonstrates the ML estimation method on simulated ideal point reflectors for various SNR levels. The simulation is parameterized by the size and location of the scene to be imaged, the range and azimuth resolution, the width of the antenna, the altitude of the sensor, the carrier frequency, and the SNR (in dB). All the other parameters for the simulation are derived from these user defined variables.

In these simulations, an ideal flight path is flown (although considering how the data matrix $\mathcal{F}$ is constructed, a non-ideal flight path could easily be simulated, too). The scene to be imaged is 30 meters by 30 meters, the center of the scene is located 155 meters from the nadir track and consists of five reflectors with location and reflectivity: $g(146.5, -8.5, 0) = 10$, $g(161.5, -2.5, 0) = 100$, $g(146.5, -0.5, 0) = 100$, $g(154.5, -0.5, 0) = 0.1$, and $g(161.5, 6.5, 0) = 1$. The rest of the user defined parameters are as follows: $R_a = 1$ meter, $R_r = 1$ meter, $W = 1$ meter, $h = 500$ meters, and $f_c = 10$ GHz. Based on these parameters, $L = 2$ meters, $\lambda = 0.03$ meters, $\vartheta_N = 1.719°$, $N_k = 91$ pulses, and $N_n = 509$ samples. An illustration of the antenna beam pattern overlaying the ground to be imaged for the center pulse is shown in figure 6.1. In figure 6.1, the antenna is shown in a dB scale and the scene is outlined with bold black lines. Due to the short range to the scene and the desired resolution, the PRF rate and the velocity of the sensor are unrealistically high. However, the altitude and resolution were selected so the simulated data set will be small enough for a desktop computer to process.

In the first simulation the SNR $= \infty$. Figure 6.2 shows the magnitude of the baseband SAR data array, figure 6.3 shows the CBP image reconstruction, and figure 6.4 shows the ML image reconstruction. Notice that all of the reflectors are easily distinguished in the ML reconstruction (and their scales recovered), but only the strong reflectors are distinguishable in the CBP reconstruction.

The following SNR levels were also simulated 0 dB, 20 dB, and 40 dB and the ML image reconstructions are illustrated in figures 6.5, 6.6, and 6.7, respectively. Notice the

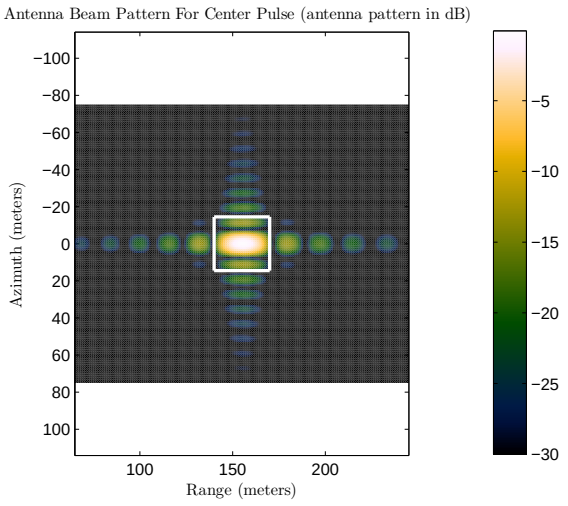

Fig. 6.1: Illustration of the antenna beam pattern overlaying the image for the center pulse location.

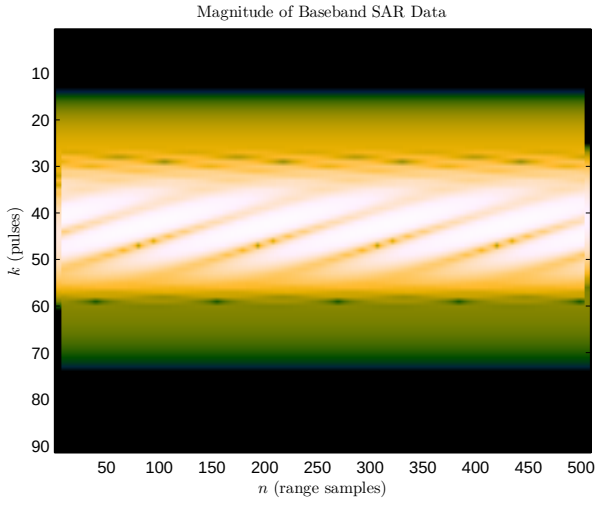

Fig. 6.2: Illustration of the magnitude of the baseband SAR data array for SNR $= \infty$ dB.

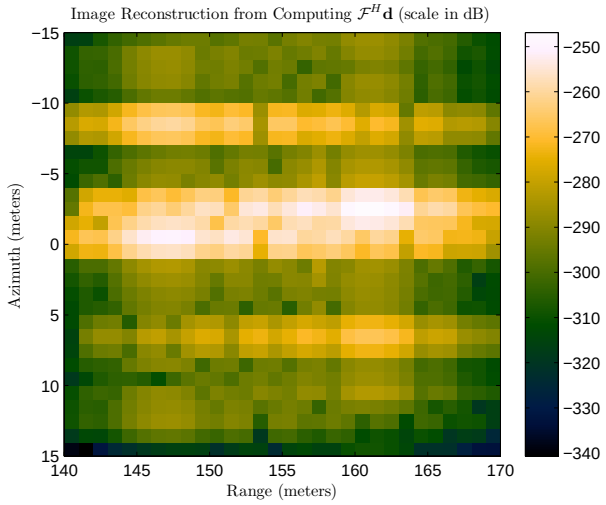

Fig. 6.3: Illustration of the CBP image reconstruction for SNR $= \infty$ dB.

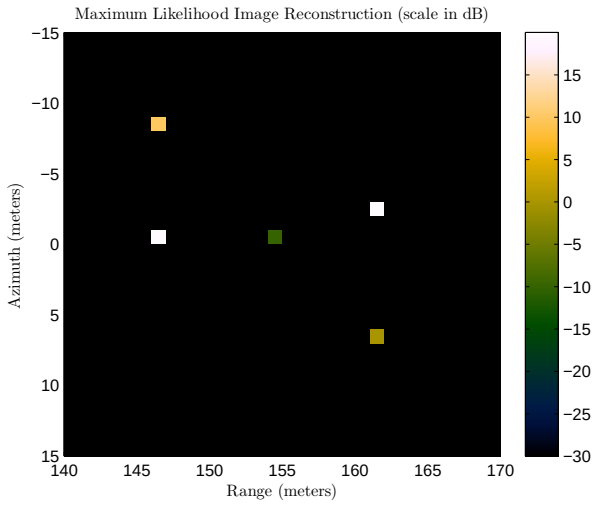

Fig. 6.4: Illustration of the ML image reconstruction for SNR $= \infty$ dB.

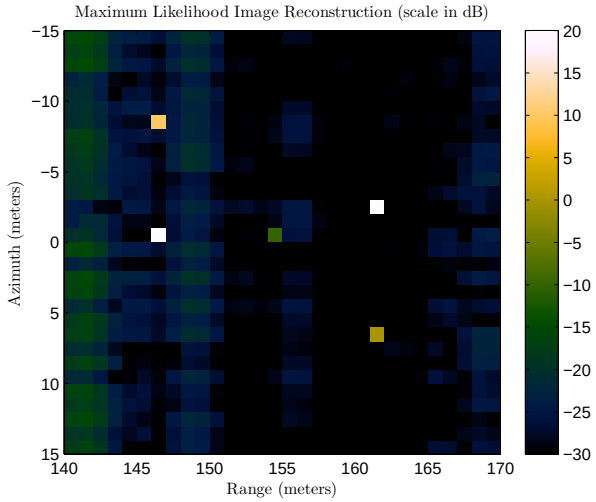

Fig. 6.5: Illustration of the ML image reconstruction for SNR = 0 dB.

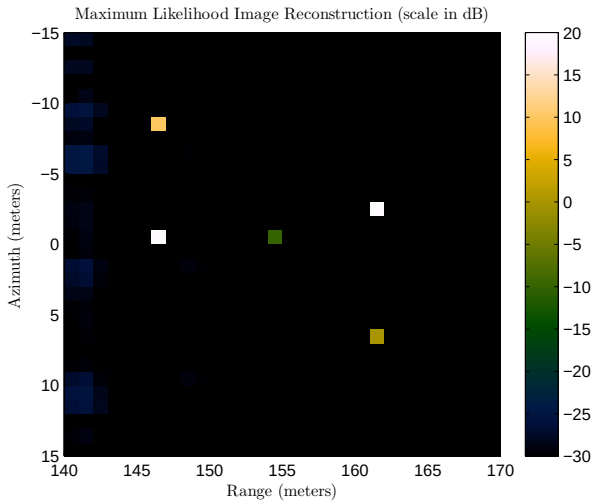

Fig. 6.6: Illustration of the ML image reconstruction for SNR = 20 dB.

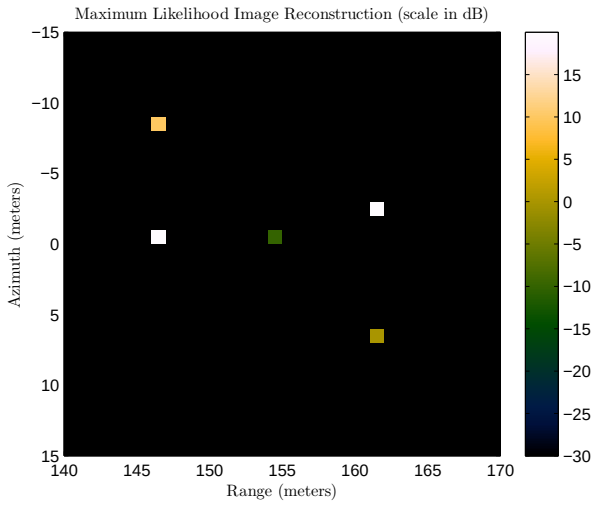

Fig. 6.7: Illustration of the ML image reconstruction for SNR = 40 dB.

stronger reflectors are easy to pick out. However at lower SNR levels, the weaker reflectors are not easily distinguished.

From the simulation results, it is clear the IPI from each reflector is gone; multiplying $\mathcal{F}^H\mathbf{d}$ by $(\mathcal{F}^H\mathcal{F})^{-1}$ has decorrelated the image. At the higher SNR levels the reflectivity of the reflectors has also been recovered. Another important thing to note in these simulations is that the reconstruction array was made to be uniform on the ground. Therefore, the ML image was formed to this reconstruction array and is a uniformly spaced image in the ground range; no extra post-processing interpolation was necessary to convert from the slant-range to the ground range.

6.3 Cramér-Rao Lower Bound Analysis

It is well known that the ML estimate of the parameter vector of the linear statistical model is unbiased and efficient [29]. In the ML estimation of the ground reflectivity, $\mathbf{g}$ is the parameter vector. Since the data are collected in the presence of circularly symmetric AWGN, the Fisher information matrix is

$$J = \frac{T_s}{N_0}\mathcal{F}^H\mathcal{F}. \tag{6.23}$$

The inverse of the Fisher information matrix is the Cramér-Rao lower bound (CRLB). The CRLB provides a lower bound for the covariance of any unbiased estimate of the parameter vector [29]. For the ground reflectivity estimates, the CRLB is

$$CRLB = \frac{N_0}{T_s}(\mathcal{F}^H\mathcal{F})^{-1}. \tag{6.24}$$

Using that $\sigma_\eta^2 = N_0/Ts$, this can also be written as

$$CRLB = \sigma_\eta^2(\mathcal{F}^H\mathcal{F})^{-1}. \tag{6.25}$$

Thus, the CRLB scales with the variance of the AWGN. The diagonal elements of the CRLB matrix give the lower bound on the variance of the parameter vector estimates.

The grammian matrix for stripmap SAR is a function of many different system and imaging parameters, thus so is the CRLB. The dependence of the CRLB on the system and imaging parameters will not be explored in this dissertation. The diagonal entries of the CRLB for the simulation as stated above for SNR = 40 dB are illustrated in figure 6.8. The diagonal entries have been reordered and illustrated in a two-dimensional array so that they correspond to the actual ground locations. The scale in 6.8 is in dB; note that the estimates of left and right edges have have higher variance than the center of the image. This is due to the antenna pattern (in range) as it sweeps across the scene (compare the antenna pattern in figure 6.1 and note the similarities between the antenna beam pattern nulls (in range) and the CRLB illustrated in figure 6.8).

Since an ideal flight was simulated in the simulation, it is worth looking at the average variance bounds for each range (the average is computed along azimuth). Figure 6.9 shows the average variance bounds for each range for the simulation.

6.4 Insights into the ML Estimation Method

The most computational part of the ML algorithm is the inversion of the grammian matrix. Figure 6.10 shows the magnitude of grammian matrix, $\mathcal{F}^H\mathcal{F}$. The structure of this

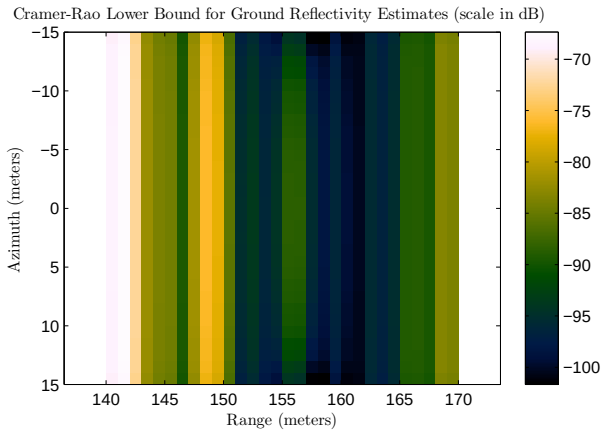

Fig. 6.8: Illustration of the CRLB for the simulation as stated above for SNR = 40 dB.

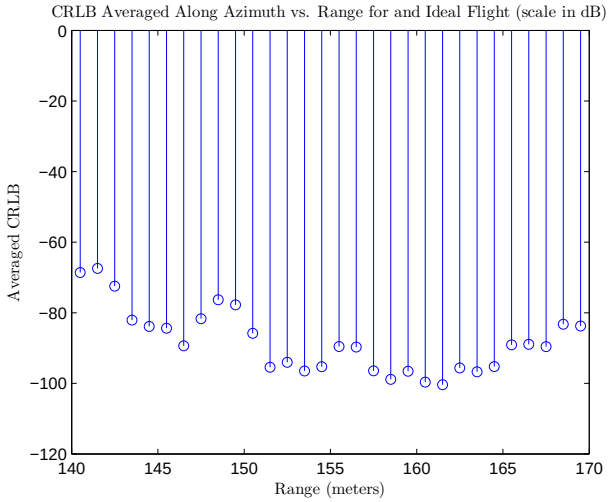

Fig. 6.9: Illustration of the averaged (along azimuth) CRLB for each range for the ideal flight simulation as stated above for SNR = 40 dB.

matrix is very interesting. The $(l,m)^{th}$ entry of $\mathcal{F}^H\mathcal{F}$ is

$$\left[\mathcal{F}^H\mathcal{F}\right]_{ij} = \left\langle \mathbf{f}(k,n,\mathbf{u}_l^i), \mathbf{f}(k,n,\mathbf{u}_m^i) \right\rangle . \tag{6.26}$$

Thus, the $(l,m)^{th}$ entry of $\mathcal{F}^H\mathcal{F}$ is the inner-product of the PSRs of the reflectors at $\mathbf{u}_l^i$ and $\mathbf{u}_m^i$. The inversion of this matrix would be simplified if system parameters could be set to enforce more structure in the matrix, such as being a banded block matrix, being sparse, or being diagonally dominant. Thus, if the correlation of the neighboring reflectors could be reduced, then more effective ways of inverting $\mathcal{F}^H\mathcal{F}$ would become possible. Another factor that affects the structure of $\mathcal{F}^H\mathcal{F}$ is the selection of the reconstruction array. If the reconstruction array is too close to (or includes) nadir and is uniformly spaced, a "fan-shaped" pattern becomes apparent in each block of the grammian matrix. If the image is formed in the slant-range (which is natural to the SAR data) or if the image is a far distance from nadir (so the ground range resolution is approximately the same as the slant range resolution), then the "fan-shape" diminishes and the matrix becomes more diagonally dominant and better conditioned. In an extreme case, if the grammian matrix can be made diagonal, possibly by waveform selection and careful beam pattern selection, then inversion of the grammian matrix is just a scaling of the CBP solution.

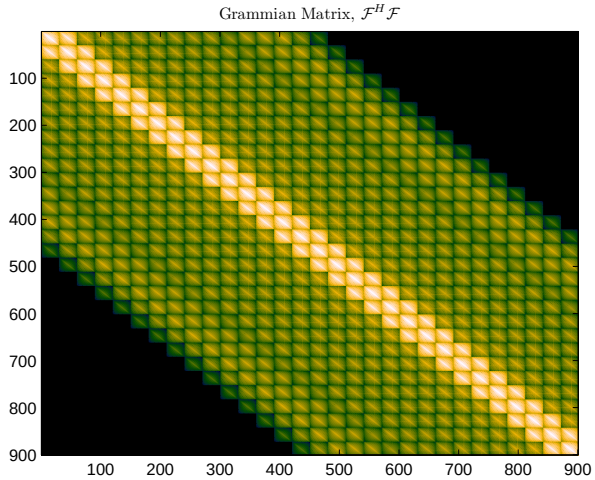

Fig. 6.10: Illustration of the absolute value of the elements of the grammian matrix.

6.5 Summary

Based on the interpretation of the forward model as a linear statistical model, the ML estimation of the ground reflectivity is derived. The ML image formation method has two steps; it was shown that the first step is equivalent to CBP processing and the second step removes the IPI. A demonstration of the ML imaging method was given in this chapter. Finally, a discussion on the Cramér-Rao lower bound is given along with some insights that the ML image formation method gives on system design.

Chapter 7

Maximum *A Posteriori* Image Formation

The contributions to stripmap SAR in this chapter are two maximum *a posteriori* (MAP) image formation algorithms. It is shown that if the prior distribution is Gaussian, then the MAP image formation has a close connection to Tikhonov regularization. Both algorithms in this chapter assume a Gaussian prior. The first algorithm forms the MAP image by solving the regularized least squares problem via the block recursive least squares (BRLS) algorithm where the priors enter into the algorithm as the initialization of the coefficient vector and the covariance matrix. The second algorithm uses the fact that if an ideal flight path is flown, the flat earth model holds, and the priors are also independent and identically distributed (*iid*), then there is block shift structure in the data matrix. Based on this matrix structure, the second (and more efficient) algorithm forms the MAP image via the block fast array RLS (BFARLS) algorithm, where the algorithm is initialized the same way as the BRLS algorithm. Simulated results are demonstrated for both algorithms and the chapter concludes with a comparison of the two methods.

7.1 *A Posteriori* Distribution

In the ML image formation, the ground reflectivity is assumed to be deterministic, but unknown. There is no way to incorporate any information about the scene reflectivity into the objective function in (6.6). Often it is known ahead of time what type of terrain is going to be imaged by the SAR sensor, such as grassy or forest areas (or both). The maximum *a posteriori* (MAP) estimation framework allows such prior information to be incorporated. MAP is more general than ML, in fact ML estimation can be derived from MAP estimation.

MAP estimation maximizes the *a posteriori* probability

$$f_{\mathbf{G}|\mathbf{D}}(\mathbf{g}|\mathbf{d}) = \frac{f_{\mathbf{D}|\mathbf{G}}(\mathbf{d}|\mathbf{g}) f_{\mathbf{G}}(\mathbf{g})}{f_{\mathbf{D}}(\mathbf{d})} \tag{7.1}$$

with respect to the coefficient vector $\mathbf{g}$. The distribution $f_{\mathbf{D}}(\mathbf{d})$ does not affect the maximization of the *a posteriori*, thus the MAP estimate is obtained from

$$\mathbf{g}_{\text{MAP}} = \arg\max_{\mathbf{g}} f_{\mathbf{D}|\mathbf{G}}(\mathbf{d}|\mathbf{g}) f_{\mathbf{G}}(\mathbf{g}), \tag{7.2}$$

which is the product of the likelihood function and the *a priori* density. In the case that the *a priori* density is uniformly distributed then $\mathbf{g}_{\text{ML}} = \mathbf{g}_{\text{MAP}}$ (the *a posteriori* density is proportional to the likelihood function and proportionality constants do not affect the optimization).

7.2 A More General Cost Function

If the ground reflectivity is assumed to be independent and identically distributed (*iid*) zero-mean Gaussian with variance σ_g^2, then the optimization in (7.2) can be written as minimizing

$$J(\mathbf{g}) = ||\mathbf{d} - \mathcal{F}\mathbf{g}||_2^2 + \mu ||\mathbf{g}||_2^2, \tag{7.3}$$

with respect to $\mathbf{g}$, where $\mu = \sigma_\eta^2 / \sigma_g^2$.

If the parameter μ is allowed to vary in the interval $\mu > 0$, then (7.3) also has the interpretation of being a regularized solution (in the Tikhonov sense) [16]. If $\mu = 0$, then the ML solution is obtained.

In the more general case where the distribution of the ground reflectivity is not modeled by *iid* Gaussian random variables (or even by Gaussian random variables at all), the minimization of the objective function

$$\tilde{J}(\mathbf{g}, \mu) = ||\mathbf{d} - \mathcal{F}\mathbf{g}||_2^2 + \mu ||\mathcal{T}\mathbf{g}||, \tag{7.4}$$

(with other possible constraints) where the norm type is intentionally left off the second term, may not have an analytic solution and other methods may be needed to obtain a solution. The matrix $\mathcal{T}$ can be any matrix, but is usually the identity matrix or a discretized differential operator [10]. If μ is allowed to vary, then the emphasis of the two norms can be changed. If $\mathcal{T}$ is the identity matrix, it can be seen that making μ large will place more emphasis on minimizing the energy in the solution. If $\mathcal{T}$ is the first discretized derivative, then making μ large places more emphasis on a smooth solution. In this chapter, we will let $\mathcal{T}$ be the identity matrix, consider μ as a regularization parameter, and assume that the *a priori* distribution is Gaussian. To be explicit, we will be using the cost function

$$J(\mathbf{g}, \mu) = ||\mathbf{d} - \mathcal{F}\mathbf{g}||_2^2 + \mu||\mathbf{g}||_2^2, \quad \mu > 0. \tag{7.5}$$

The solution to (7.5) is found by taking the gradient (with respect to $\mathbf{g}$), equating it to zero, and solving for $\mathbf{g}_{\text{MAP}}$. The computations for this lead to the regularized normal equations

$$\begin{aligned} \nabla_{J_{\mathbf{g}}} &= 0 && (7.6)\\ -\mathcal{F}^H\mathbf{d} + \mathcal{F}^H\mathcal{F}\mathbf{g} + \mu\mathbf{g}_{\text{MAP}} &= 0 && (7.7)\\ \left(\mathcal{F}^H\mathcal{F} + \mu I\right)\mathbf{g}_{\text{MAP}} &= \mathcal{F}^H\mathbf{d}. && (7.8) \end{aligned}$$

From this point on, let the MAP estimate be denoted as $\mathbf{g}_\mu$ to reflect the regularization parameter. The solution of (7.8) is

$$\mathbf{g}_\mu = \left(\mathcal{F}^H\mathcal{F} + \mu I\right)^{-1}\mathcal{F}^H\mathbf{d}. \tag{7.9}$$

Equation (7.8) is very revealing. First, note that if λ is an eigenvalue of $\mathcal{F}^H\mathcal{F}$, then $\lambda + \mu$ is an eigenvalue of $(\mathcal{F}^H\mathcal{F} + \mu I)$. It is clear that if $\mathcal{F}$ does not have full column rank then $\mathcal{F}^H\mathcal{F}$ is not invertible (*i.e.* has eigenvalues equal to zero). In such a case, the ML solution, $\mathbf{g}_{\mu=0}$ does not exist, unless $\mathcal{F}^H\mathbf{d}$ is in the range of $\mathcal{F}^H\mathcal{F}$. However, the general

MAP solution $\mathbf{g}_\mu$ for $\mu > 0$, *always* exists and it can be shown that the minimizing solution is unique for any selection of μ [16].

The value of μ that is chosen affects the condition number of the matrix $(\mathcal{F}^H\mathcal{F} + \mu I)$. The condition number is defined as the ratio of the square-root of the largest eigenvalue to the square-root of the smallest eigenvalue [29]

$$\kappa = \frac{\sqrt{\lambda_{\max} + \mu}}{\sqrt{\lambda_{\min} + \mu}}, \tag{7.10}$$

where $\lambda_{\max}$ is the largest eigenvalue of $\mathcal{F}^H\mathcal{F}$ and $\lambda_{\min}$ is the smallest. A high condition number gives rise to an unstable inverse. As can be seen, if $\mu \to \infty$, then $\kappa \to 1$, however the resulting matrix is "far" from the desired inverse. One possible selection for μ is to let $\mu < \lambda_{\min}$, this will give a solution that is "close" to the ML solution. However, the condition number may still be too high. Another approach is to select an "acceptable" value of the condition number and solve for the value of μ. Selecting a value of the condition number, $\kappa = \kappa_0$, then solving for μ gives

$$\mu = \frac{\lambda_{\max} - \kappa_0^2\lambda_{\min}}{\kappa_0^2 - 1}. \tag{7.11}$$

Of course the challenge of finding an "acceptable" condition number still exists. This chapter is not concerned with finding an optimal value of μ for general stripmap SAR, but some examples will be given that will illustrate the effect of different values of μ.

Another very important effect that μ has is its effect on the solution in the presence of noise. Substituting $\mathbf{d}$ from (5.16) into (7.9) yields

$$\begin{aligned} \mathbf{g}_\mu &= \left(\mathcal{F}^H\mathcal{F} + \mu I\right)^{-1}\mathcal{F}^H\left(\mathcal{F}\mathbf{g} + \boldsymbol{\eta}\right) && (7.12)\\ &= \left(\mathcal{F}^H\mathcal{F} + \mu I\right)^{-1}\mathcal{F}^H\mathcal{F}\mathbf{g} + \left(\mathcal{F}^H\mathcal{F} + \mu I\right)^{-1}\mathcal{F}^H\boldsymbol{\eta}. && (7.13)\end{aligned}$$

If $\mu = 0$, (*i.e.* there is no regularization) then the solution becomes the sum of the true solution and the pseudo-inverse of the data matrix times the noise vector

$$\mathbf{g}_0 = \mathbf{g} + \left(\mathcal{F}^H\mathcal{F}\right)^{-1}\mathcal{F}^H\boldsymbol{\eta}. \tag{7.14}$$

For an ill-conditioned grammian matrix, the inverse of the grammian matrix may amplify the noise, thereby making the solution meaningless. Increasing the value of μ pulls the solution away from the true solution, but reduces the effect of the noise. This suggests that an optimal value of μ should exist that minimizes (7.5). This property is called the semi-convergence property [16].

To illustrate the effect of the regularization parameter, consider the simulation parameters in section 6.2. Define the error between the true image and the regularized image as

$$\begin{aligned} e_\mu &= E\left\{||\mathbf{g} - \mathbf{g}_\mu||_2^2\right\} && (7.15)\\ &= E\left\{||\mathbf{g} - (\mathcal{F}^H\mathcal{F} + \mu I)^{-1}\mathcal{F}^H\mathcal{F}\mathbf{g} + (\mathcal{F}^H\mathcal{F} + \mu I)^{-1}\mathcal{F}^H\boldsymbol{\eta}||_2^2\right\} && (7.16)\\ &= E\left\{||(I - (\mathcal{F}^H\mathcal{F} + \mu I)^{-1}\mathcal{F}^H\mathcal{F})\mathbf{g} + (\mathcal{F}^H\mathcal{F} + \mu I)^{-1}\mathcal{F}^H\boldsymbol{\eta}||_2^2\right\}. && (7.17) \end{aligned}$$

Notice that with $\mu = 0$

$$\begin{aligned} e_0 &= E\left\{||(\mathcal{F}^H\mathcal{F})^{-1}\mathcal{F}^H\boldsymbol{\eta}||_2^2\right\} && (7.18)\\ &= E\left\{\boldsymbol{\eta}^H\mathcal{F}(\mathcal{F}^H\mathcal{F})^{-H}(\mathcal{F}^H\mathcal{F})^{-1}\mathcal{F}^H\boldsymbol{\eta}\right\} && (7.19)\\ &= E\left\{\mathrm{tr}(\mathcal{F}(\mathcal{F}^H\mathcal{F})^{-H}(\mathcal{F}^H\mathcal{F})^{-1}\mathcal{F}^H\boldsymbol{\eta}\boldsymbol{\eta}^H)\right\} && (7.20)\\ &= \mathrm{tr}(\mathcal{F}(\mathcal{F}^H\mathcal{F})^{-H}(\mathcal{F}^H\mathcal{F})^{-1}\mathcal{F}^H E\left\{\boldsymbol{\eta}\boldsymbol{\eta}^H\right\}) && (7.21)\\ &= \mathrm{tr}(\mathcal{F}(\mathcal{F}^H\mathcal{F})^{-H}(\mathcal{F}^H\mathcal{F})^{-1}\mathcal{F}^H(\sigma_\eta^2 I)) && (7.22)\\ &= \sigma_\eta^2\mathrm{tr}((\mathcal{F}^H\mathcal{F})^{-1}). && (7.23) \end{aligned}$$

Also, notice that as $\mu \to \infty$

$$e_\infty = E\left\{||\mathbf{g}||_2^2\right\}. \tag{7.24}$$

For the first example, let the $SNR = \infty$ dB. Figure 7.1 shows the error (in dB) versus μ. Notice that with no noise, $e \to 0$ as $\mu \to 0$ as expected. For the parameters given, (7.24) gives $e_\infty = 19,836 \approx 43$ dB. It is clear that for this example the optimal value of μ is zero.

In the next example, let the $SNR = 2$ dB. Figure 7.2 shows the error (in dB) versus μ. The semi-convergence property is evident and a non-zero optimal value of μ exists; the error decreases as μ starts to increase because μ is decreasing the effect of the noise, but after the optimal value of μ, the error starts to increase because μ is pulling the solution further from the true solution. For the parameters given, (7.23) gives $e_0 = 43.4 \approx 16.3$ dB and (7.24) gives $e_\infty = 19,836 \approx 43$ dB.

7.3 Stripmap SAR Data Matrix

In section 5.1 the stripmap SAR data matrix was explained and the following notation was given: N_n is the number of samples taken from a single transmitted pulse, N_k is the number of pulses transmitted during the data collection process, N_a is the number of azimuth pixels in the reconstruction array, and N_r is the number of range pixels in the reconstruction array. Another quantity that is needed in this section is

$$s = \Delta R_a / vT, \tag{7.25}$$

where ΔR_a is the azimuth resolution and vT is the distance traveled between pulsing intervals (assumed equally spaced). Thus, s is the number of pulses that are transmitted while the sensor travels ΔR_a meters. Equivalently, s is the number of pulses until the $(a+1)^{st}$ azimuth cell enters the antenna beam just after the a^{th} azimuth cell has entered the antenna beam, for a fixed range cell r.

The data matrix $\mathcal{F}$ has block structure with $(sN_n \times N_r)$ blocks. To see this, let the

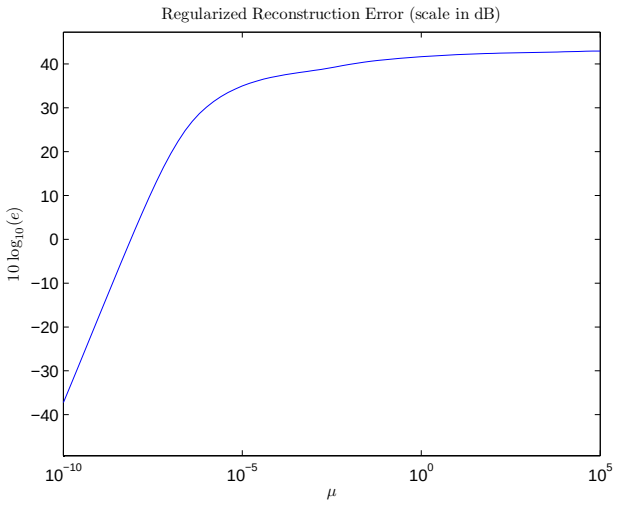

Fig. 7.1: Illustration of the error (in dB) versus μ for $SNR = \infty$ dB.

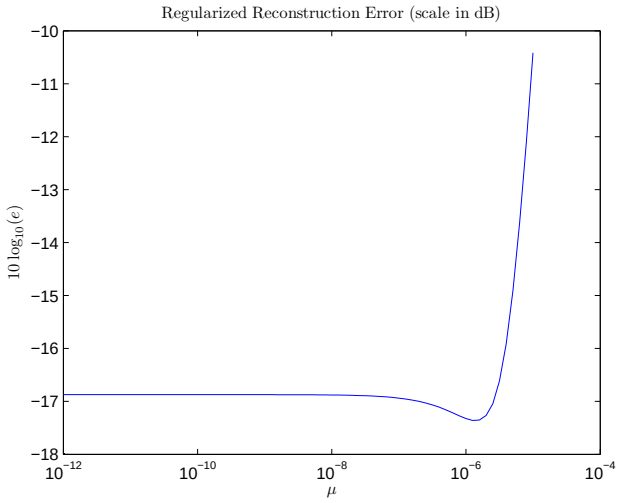

Fig. 7.2: Illustration of the error (in dB) versus μ for $SNR = 2$ dB. Notice the semi-convergence property.

indexing pair (k,n) denote the n^{th} sample from the k^{th} pulse in the collected data. Note that $((k+1),n)$ is N_n samples from (k,n) in the collected data. More generally, $((k+s),n)$ is sN_n samples from (k,n) in the collected data. Due to the construction of the data matrix, the first N_r columns of $\mathcal{F}$ are the PSRs associated with the first row of the reconstruction array, the next N_r columns are the PSRs associated with the second row, and so on. Since the response to the a^{th} row of the reconstruction array is separated by sN_n samples in the data from the response of the $(a+1)^{st}$ row, the block row size is sN_n. Thus, the matrix $\mathcal{F}$ can be written as

$$\mathcal{F} = \begin{bmatrix} \tilde{U}_{0,0} & \tilde{U}_{0,1} & \cdots & \tilde{U}_{0,N_a-1} \\ \tilde{U}_{1,0} & \tilde{U}_{1,1} & \cdots & \tilde{U}_{1,N_a-1} \\ \vdots & \vdots & \ddots & \vdots \\ \tilde{U}_{L-1,0} & \tilde{U}_{L-1,1} & \cdots & \tilde{U}_{L-1,N_a-1} \end{bmatrix}, \tag{7.26}$$

where $L = N_k/s$ and the submatrices $\tilde{U}_{l,r}$ are each $(sN_n \times N_r)$. The matrix $\mathcal{F}$ can also be written in terms of block rows

$$\mathcal{F} = \left[\begin{array}{c} \tilde{U}_0 \\ \hline \tilde{U}_1 \\ \hline \vdots \\ \hline \tilde{U}_{L-1} \end{array}\right], \tag{7.27}$$

where the block rows $\tilde{U}_l$ are each $(sN_n \times N_a N_r)$. If $s = 1$, then this representation is the same as in (5.10), otherwise the relationship between $\tilde{U}_l$ and $\mathcal{F}_k$ is

$$\tilde{U}_l = \left[\begin{array}{c} \mathcal{F}_{sl+1} \\ \hline \vdots \\ \hline \mathcal{F}_{s(l+1)} \end{array}\right], \tag{7.28}$$

where $0 \leq l \leq L-1$. Finally, define the $(N_a N_r \times sN_n)$ matrices

$$U_l = \tilde{U}_l^H, \tag{7.29}$$

which we will use as regressors in the algorithms derived in this chapter.

7.4 Block Recursive Least-Squares Algorithm for Stripmap SAR

It is well known that the recursive least-squares (RLS) algorithm recursively solves the equation

$$(\Pi + \mathcal{A}^H \mathcal{A})\mathbf{x} = \mathcal{A}^H \mathbf{b} + \Pi \bar{\mathbf{x}}, \tag{7.30}$$

as additional vectors of data are added to the rows of the data matrix [30], where $\mathcal{A}$ is the data matrix, $\mathbf{x}$ is the solution vector, $\mathbf{b}$ is the vector of observations, Π is a positive definite regularizing matrix, and $\bar{\mathbf{x}}$ represents a nominal solution. This is exactly (7.8) where $\mathcal{F} = \mathcal{A}$, $\mathbf{g} = \mathbf{x}$, $\mathbf{d} = \mathbf{b}$, $\Pi = \mu I$, and $\bar{\mathbf{x}} = \mathbf{0}$. Thus, the regularized normal equations in (7.8) can be solved recursively using the RLS algorithm where the regressors are the Hermitian transpose of the rows of $\mathcal{F}$.

The regularized normal equations can not only be solved using the scalar RLS algorithm, but they can also be solved by using the block RLS algorithm. The derivation of the scalar RLS algorithm can be found in [29, 30]; the derivation of the block-RLS is a natural extension to the derivation of the scalar RLS algorithm (a summary of the block RLS equations can be found on page 552 of [30]).

7.4.1 Block RLS Algorithm Derivation

Some preliminaries that are needed for the block RLS algorithm are the the matrix inversion lemma, which states

$$(A + XRY)^{-1} = A^{-1} - A^{-1}X(R^{-1} + YA^{-1}X)^{-1}YA^{-1}, \tag{7.31}$$

where A and R are invertible matrices, the fact that we can write the grammian matrix $\mathcal{F}^H\mathcal{F}$ as

$$\mathcal{F}^H\mathcal{F} = \sum_{l=0}^{L-1} U_l U_l^H, \tag{7.32}$$

and the fact that the correlation vector $\mathcal{F}^H\mathbf{d}$ may be written as

$$\mathcal{F}^H\mathbf{d} = \sum_{l=0}^{L-1} U_l \mathbf{d}_l. \tag{7.33}$$

Define the partial sums of (7.32) and (7.33) as

$$\begin{aligned} R_t &= \sum_{l=0}^{t} U_l U_l^H & (7.34)\\ &= \sum_{l=0}^{t-1} U_l U_l^H + U_t U_t^H & (7.35)\\ &= R_{t-1} + U_t U_t^H, & (7.36) \end{aligned}$$

and

$$\begin{aligned} \mathbf{p}_t &= \sum_{l=0}^{t} U_l \mathbf{d}_l & (7.37)\\ &= \sum_{l=0}^{t-1} U_l^H \mathbf{d}_l + U_t \mathbf{d}_t & (7.38)\\ &= \mathbf{p}_{t-1} + U_t \mathbf{d}_t. & (7.39) \end{aligned}$$

The normal equations at time t can be written as

$$R_t \mathbf{g}_t = \mathbf{p}_t, \tag{7.40}$$

and the solution at time t (assuming that R_t is invertible) is

$$\begin{aligned}
\mathbf{g}_t &= R_t^{-1}\mathbf{p}_t && (7.41)\\
&= (R_{t-1} + U_t U_t^H)^{-1}\mathbf{p}_t && (7.42)\\
&= (R_{t-1}^{-1} - R_{t-1}^{-1}U_t(I + U_t^H R_{t-1}^{-1}U_t)^{-1}U_t^H R_{t-1}^{-1})\mathbf{p}_t, && (7.43)
\end{aligned}$$

where the matrix inversion lemma has been used to obtain the last equation. If we make the change of notation, $P_l = R_l^{-1}$ for some integer l, then (7.43) can be written as

$$\mathbf{g}_t = (P_{t-1} - P_{t-1}U_t(I + U_t^H P_{t-1}U_t)^{-1}U_t^H P_{t-1})\mathbf{p}_t. \quad (7.44)$$

Notice that the update to the inverse of the grammian matrix can be computed recursively

$$P_t = P_{t-1} - P_{t-1}U_t(I + U_t^H P_{t-1}U_t)^{-1}U_t^H P_{t-1}. \quad (7.45)$$

Substituting (7.39) into (7.44) gives

$$\begin{aligned}
\mathbf{g}_t &= (P_{t-1} - P_{t-1}U_t(I + U_t^H P_{t-1}U_t)^{-1}U_t^H P_{t-1})(\mathbf{p}_{t-1} + U_t\mathbf{d}_t) && (7.46)\\
&= P_{t-1}\mathbf{p}_{t-1} - P_{t-1}U_t(I + U_t^H P_{t-1}U_t)^{-1}U_t^H P_{t-1}\mathbf{p}_{t-1} && (7.47)\\
&\quad + (P_{t-1}U_t - P_{t-1}U_t(I + U_t^H P_{t-1}U_t)^{-1}U_t^H P_{t-1}U_t)\mathbf{d}_t. && (7.48)
\end{aligned}$$

Using that $\mathbf{g}_{t-1} = P_{t-1}\mathbf{p}_{t-1}$ (by definition), (7.48) can be written recursively

$$\begin{aligned}
\mathbf{g}_t &= \mathbf{g}_{t-1} - P_{t-1}U_t(I + U_t^H P_{t-1}U_t)^{-1}U_t^H\mathbf{g}_{t-1} && (7.49)\\
&\quad + (P_{t-1}U_t - P_{t-1}U_t(I + U_t^H P_{t-1}U_t)^{-1}U_t^H P_{t-1}U_t)\mathbf{d}_t && (7.50)\\
&= \mathbf{g}_{t-1} - P_{t-1}U_t(I + U_t^H P_{t-1}U_t)^{-1}U_t^H\mathbf{g}_{t-1} && (7.51)\\
&\quad + (P_{t-1}U_t(I + U_t^H P_{t-1}U_t)^{-1}((I + U_t^H P_{t-1}U_t) - U_t^H P_{t-1}U_t)\mathbf{d}_t && (7.52)\\
&= \mathbf{g}_{t-1} - P_{t-1}U_t(I + U_t^H P_{t-1}U_t)^{-1}U_t^H\mathbf{g}_{t-1} + P_{t-1}U_t(I + U_t^H P_{t-1}U_t)^{-1}\mathbf{d}_t. && (7.53)
\end{aligned}$$

Define

$$\Gamma_t = (I + U_t^H P_{t-1} U_t)^{-1}, \tag{7.54}$$

then (7.53) can be written as

$$\mathbf{g}_t = \mathbf{g}_{t-1} - P_{t-1} U_t \Gamma_t U_t^H \mathbf{g}_{t-1} + P_{t-1} U_t \Gamma_t \mathbf{d}_t. \tag{7.55}$$

Finally, define

$$G_t = P_{t-1} U_t \Gamma_t, \tag{7.56}$$

then the coefficient update becomes

$$\mathbf{g}_t = \mathbf{g}_{t-1} - G_t(\mathbf{d}_t - U_t^H \mathbf{g}_{t-1}). \tag{7.57}$$

The important equations for the block RLS algorithm are the inverse grammian update in (7.45), the conversion factor in (7.54), the gain in (7.56), and the coefficient update in (7.57).

It is clear from the iterations that both $\mathbf{g}_{-1}$ and P_{-1} are needed. The coefficient vector $\mathbf{g}_{-1}$ can be initialized to the zero vector (this is equivalent to letting $\bar{\mathbf{x}} = \mathbf{0}$ in (7.30)) and implies that the *a priori* distribution on $\mathbf{g}$ has zero mean. Another good choice is to initialize $\mathbf{g}_{-1} = \mathcal{F}^H \mathbf{d}$ (the CBP solution) which is "close" to the true solution in the sense that it incorporates some knowledge of the image to the algorithm. The initialization of the inverse grammian matrix can be obtained from (7.8) and is $P_{-1} = (1/\mu)I$ (this is equivalent to letting $\Pi = (1/\mu)I$ in (7.30)); this implies that the elements of $\mathbf{g}$ in the *a priori* distribution have the same variance and are uncorrelated. The algorithm for solving the block RLS algorithm is given in Algorithm (7.1).

Algorithm 7.1 Block RLS Algorithm for Stripmap SAR

Initialize:

$P_{-1} = \frac{1}{\mu} I_{N_a N_r \times N_a N_r}$,
$\mathbf{g}_{-1} = \mathbf{0}$ or $\mathbf{g}_{-1} = \mathcal{F}^H \mathbf{d}$

Iterate:

$\Gamma_i = (I + U_i^H P_{i-1} U_i)^{-1}$ (conversion factor, $(sN_n \times sN_n)$)
$G_i = P_{i-1} U_i \Gamma_i$ (gain matrix, $(N_a N_r \times sN_n)$)
$P_i = P_{i-1} - G_i U_i^H P_{i-1}$ (covariance update, $(N_a N_r \times N_a N_r)$)
$\mathbf{g}_i = \mathbf{g}_{i-1} + G_i(\mathbf{d}_i - U_i^H \mathbf{g}_{i-1})$ (coefficient update, $(N_a N_r \times 1)$)

7.4.2 Block RLS Algorithm Results

To demonstrate the block RLS algorithm, consider the simulation parameters in section 6.2. The optimal μ value is found by selecting a SNR level and numerically finding the value of μ that corresponds to the minimum value of e_μ.

In the first example, the $SNR = 2$ dB and $\mu_{opt} = 1.0000 \times 10^{-8}$. The ML image is illustrated in figure 7.3 and the block RLS image is illustrated in figure 7.4. The error in the block RLS image is 13.05 dB and the error in the ML image is 13.39 dB. As an interesting side note, the smallest eigenvalue of the grammian matrix is $\lambda_{min} = 3.1551 \times 10^{-8}$.

In the next example, the $SNR = 20$ dB and $\mu_{opt} = 1.0000 \times 10^{-9}$. The ML image is illustrated in figure 7.5 and the block RLS image is illustrated in figure 7.6. The error in the block RLS image is -6.3096 dB and the error in the ML image is -6.0813 dB. Since the simulation has not changed (only the SNR), the smallest eigenvalue of the grammian matrix is still $\lambda_{min} = 3.1551 \times 10^{-8}$.

As can be seen, the block RLS image formation (with a properly selected value of μ) has lower error than the ML image formation in the presence of noise. When no noise is present, the ML will give an exact solution, however the block RLS algorithm will not because a non-zero value of μ must be chosen to initialize the algorithm.

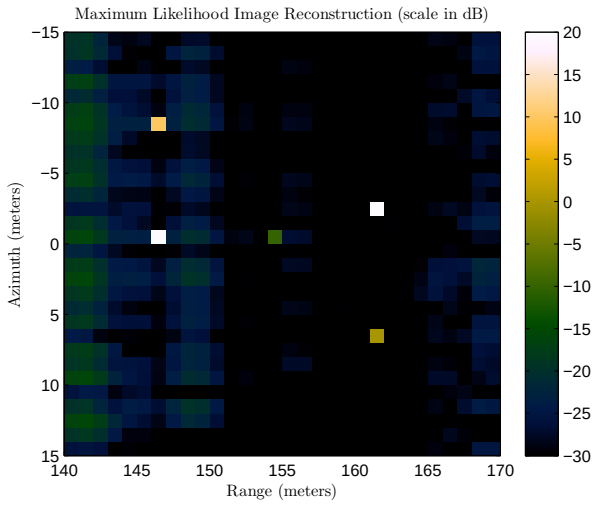

Fig. 7.3: Illustration of the ML image reconstruction (for comparison with the block RLS image reconstruction) for $SNR = 2$ dB.

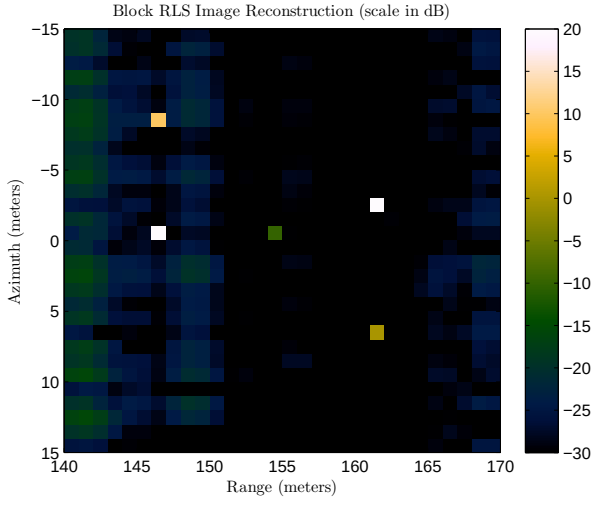

Fig. 7.4: Illustration of the block RLS image reconstruction for $SNR = 2$ dB.

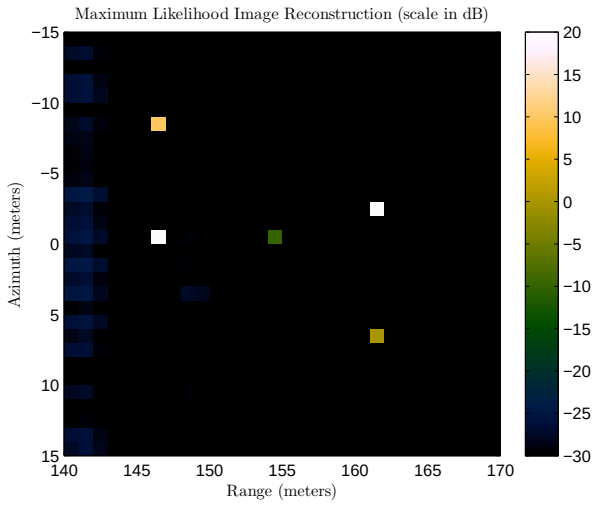

Fig. 7.5: Illustration of the ML image reconstruction (for comparison with the block RLS image reconstruction) for $SNR = 20$ dB.

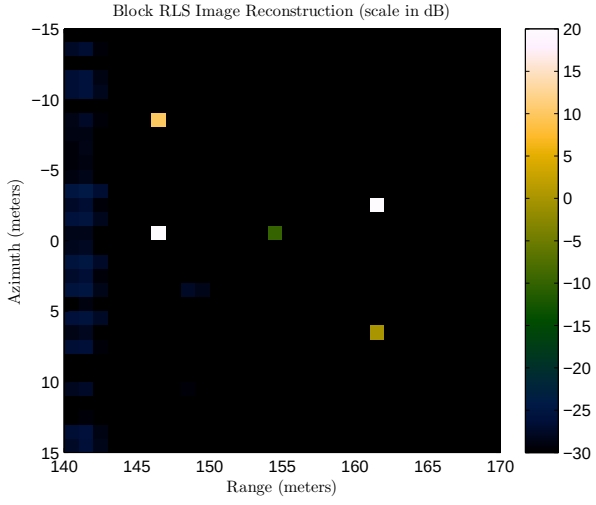

Fig. 7.6: Illustration of the block RLS image reconstruction for $SNR = 20$ dB.

7.5 Block Fast Array RLS Algorithm for Stripmap SAR

If the flat earth assumption holds, a uniformly spaced $N_a \times N_r$ rectangular reconstruction array is defined, and an ideal flight is flown, then $\mathcal{F}$ has block toeplitz structure

$$\mathcal{F} = \begin{bmatrix} \tilde{U}_0 & 0 & \cdots & 0 & 0 \\ \vdots & \tilde{U}_0 & \ddots & \vdots & \vdots \\ \tilde{U}_{L-1} & \vdots & \ddots & \tilde{U}_0 & 0 \\ 0 & \tilde{U}_{L-1} & \ddots & \vdots & \tilde{U}_0 \\ \vdots & \vdots & \ddots & \tilde{U}_{L-1} & \vdots \\ 0 & 0 & \cdots & 0 & \tilde{U}_{L-1} \end{bmatrix}. \tag{7.58}$$

The l^{th} and $(l+1)^{th}$ regressors are

$$U_l = \begin{bmatrix} \tilde{U}_l^H \\ \tilde{U}_{l-1}^H \\ \vdots \\ \tilde{U}_{l-N_a-1}^H \end{bmatrix}, \qquad U_{l+1} = \begin{bmatrix} \tilde{U}_{l+1}^H \\ \tilde{U}_l^H \\ \vdots \\ \tilde{U}_{l-N_a}^H \end{bmatrix}. \tag{7.59}$$

It is clear that the regressors have block shifted form.

In the last section, the block nature of $\mathcal{F}$ led to the block RLS algorithm, but another more efficient algorithm can be developed that takes advantage of the block shifted structure. In the case of scalar shift structure, the fast array RLS (FARLS) algorithm solves the regularized normal equations [30, 31]. In this section the scalar FARLS is extended, and a block FARLS algorithm is developed to solve the regularized normal equations by exploiting the block shift structure.

In the scalar FARLS both circular and hyperbolic rotations are needed to transform the pre-array into the post-array. In the block FARLS, the circular rotations can be accomplished the same way as in the scalar FARLS, however a block hyperbolic rotation is needed. The block hyperbolic that is used is derived in the Appendix.

7.5.1 Block FARLS Algorithm Derivation

The goal of fast array algorithms is to find an efficient way to update the coefficient vector. If an efficient way to update the gain matrix existed for the block case, then the goal could be realized. With this goal in mind, consider the updates for the gain matrix (from the block RLS equations in Algorithm 7.1) for two successive time instants

$$G_k = \Gamma_k^H U_k^H P_{k-1} \quad \text{and} \quad G_{k+1} = \Gamma_{k+1}^H U_{k+1}^H P_k. \tag{7.60}$$

These successive gain matrix updates can be manipulated to obtain efficient update.

From (7.59), notice that the following extended block matrix can be written due to the block shift structure of the data matrix

$$\begin{bmatrix} \tilde{U}_{k+1}^H \\ \tilde{U}_k^H \\ \vdots \\ \tilde{U}_{k-N_a}^H \\ \tilde{U}_{k-N_a-1}^H \end{bmatrix} = \begin{bmatrix} U_{k+1} \\ \tilde{U}_{k-N_a-1}^H \end{bmatrix} = \begin{bmatrix} \tilde{U}_{k+1}^H \\ U_k \end{bmatrix}, \tag{7.61}$$

where this extended matrix has dimension $((N_a+1)N_r \times sN_n)$. Also, consider the extended matrices (using the relationship in (7.61))

$$\begin{bmatrix} P_k U_{k+1} \\ 0_d \end{bmatrix} = \begin{bmatrix} P_k & 0_a \\ 0_b & 0_c \end{bmatrix} \begin{bmatrix} U_{k+1} \\ \tilde{U}_{k-N_a-1}^H \end{bmatrix} = \begin{bmatrix} P_k & 0_a \\ 0_b & 0_c \end{bmatrix} \begin{bmatrix} \tilde{U}_{k+1}^H \\ U_k \end{bmatrix}, \tag{7.62}$$

and

$$\begin{bmatrix} 0_d \\ P_{k-1} U_k \end{bmatrix} = \begin{bmatrix} 0_c & 0_b \\ 0_a & P_{k-1} \end{bmatrix} \begin{bmatrix} \tilde{U}_{k+1}^H \\ U_k \end{bmatrix}. \tag{7.63}$$

The dimensions of the zero matrices are: 0_a is $(N_a N_r \times N_r)$, 0_b is $(N_r \times N_a N_r)$, 0_c is $(N_r \times N_r)$, and 0_d is $(N_r \times sN_n)$. Subtracting (7.63) from (7.62) gives

$$\begin{bmatrix} P_k U_{k+1} \\ 0_d \end{bmatrix} - \begin{bmatrix} 0_d \\ P_{k-1} U_k \end{bmatrix} = \left(\begin{bmatrix} P_k & 0_a \\ 0_b & 0_c \end{bmatrix} - \begin{bmatrix} 0_c & 0_b \\ 0_a & P_{k-1} \end{bmatrix} \right) \begin{bmatrix} \tilde{U}_{k+1}^H \\ U_k \end{bmatrix}. \tag{7.64}$$

Let δP_k denote the difference

$$\delta P_k = \begin{bmatrix} P_k & 0_a \\ 0_b & 0_c \end{bmatrix} - \begin{bmatrix} 0_c & 0_b \\ 0_a & P_{k-1} \end{bmatrix}, \tag{7.65}$$

then rewriting (7.64) using (7.65) gives

$$\begin{bmatrix} P_k U_{k+1} \\ 0_d \end{bmatrix} = \begin{bmatrix} 0_d \\ P_{k-1} U_k \end{bmatrix} + \delta P_k \begin{bmatrix} \tilde{U}_{k+1}^H \\ U_k \end{bmatrix}. \tag{7.66}$$

Taking the Hermitian transpose and extending the gain matrices (in a way such that (7.66) may be used), two successive time instants of the gain update may be written as

$$\begin{bmatrix} 0_d \\ G_k^H \end{bmatrix} = \begin{bmatrix} 0_d \\ P_{k-1} U_k \end{bmatrix} \Gamma_k \quad \Rightarrow \quad \begin{bmatrix} 0_d \\ G_k^H \Gamma_k^{-1} \end{bmatrix} = \begin{bmatrix} 0_d \\ P_{k-1} U_k \end{bmatrix}, \tag{7.67}$$

and

$$\begin{bmatrix} G_{k+1}^H \\ 0_d \end{bmatrix} = \begin{bmatrix} P_k U_{k+1} \\ 0_d \end{bmatrix} \Gamma_{k+1} \quad \Rightarrow \quad \begin{bmatrix} G_{k+1}^H \Gamma_{k+1}^{-1} \\ 0_d \end{bmatrix} = \begin{bmatrix} P_k U_{k+1} \\ 0_d \end{bmatrix}. \tag{7.68}$$

Now, using (7.66) and (7.67), (7.68) may be written

$$\begin{bmatrix} G_{k+1}^H \Gamma_{k+1}^{-1} \\ 0_d \end{bmatrix} = \begin{bmatrix} 0_d \\ G_k \Gamma_k^{-1} \end{bmatrix} + \delta P_k \begin{bmatrix} \tilde{U}_{k+1}^H \\ U_k \end{bmatrix}. \tag{7.69}$$

What is really needed is the gain matrix, not the product of the gain matrix and the inverse

of the conversion factor. Consider the inverse of the conversion factor update from the block RLS equations for two successive time instants

$$\Gamma_k^{-1} = (I + U_k^H P_{k-1} U_k) \quad \text{and} \quad \Gamma_{k+1}^{-1} = (I + U_{k+1}^H P_k U_{k+1}). \tag{7.70}$$

Subtracting the equations in (7.70) gives

$$\Gamma_{k+1}^{-1} - \Gamma_k^{-1} = U_{k+1}^H P_k U_{k+1} - U_k^H P_{k-1} U_k. \tag{7.71}$$

With some manipulation, the right-hand side of (7.71) can be written

$$U_{k+1}^H P_k U_{k+1} - U_k^H P_{k-1} U_k = \begin{bmatrix} \tilde{U}_{k+1} & U_k^H \end{bmatrix} \delta P_k \begin{bmatrix} \tilde{U}_{k+1}^H \\ U_k \end{bmatrix}. \tag{7.72}$$

Putting the pieces together, (7.71) can be written

$$\Gamma_{k+1}^{-1} = \Gamma_k^{-1} + \begin{bmatrix} \tilde{U}_{k+1} & U_k^H \end{bmatrix} \delta P_k \begin{bmatrix} \tilde{U}_{k+1}^H \\ U_k \end{bmatrix}, \tag{7.73}$$

thus giving an update for the inverse of the conversion factor.

In the development up to this point, we have not accomplished the goal of an efficient update of the gain matrix (in fact it has become more computational due to the δP_k term). Before proceeding, consider how this algorithm up to this point would be initialized. The initial conditions would be: $G_{-1} = 0_{(sN_n \times N_a N_r)}$, $\Gamma_{-1}^{-1} = I_{(sN_n \times sN_n)}$, $P_{-2} = P_{-1} = (1/\mu) I_{(N_a N_r \times N_a N_r)}$, and $\delta P_{-1} = (1/\mu)\text{BlockDiag}(I_{(N_r \times N_r)}\, 0_{((N_a-1)N_r \times (N_a-1)N_r)}\, -I_{(N_r \times N_r)})$, where μ is the regularization parameter. The key to an efficient algorithm lies in the rank of δP_k. Notice that δP_{-1} has rank $2N_r$. Due to the block shift structure of the regressors, algebraically δP_k maintains rank $2N_r$ for all k (numerically, the rank may change, this indicates that instability is setting in). The matrix δP_{-1} can be factored as

$$\delta P_{-1} = L_{-1} S L_{-1}^H, \tag{7.74}$$

where

$$S = \begin{bmatrix} I_{(N_r \times N_r)} & 0_{(N_r \times N_r)} \\ 0_{(N_r \times N_r)} & -I_{(N_r \times N_r)} \end{bmatrix}, \tag{7.75}$$

and

$$L_{-1} = \sqrt{1/\mu} \begin{bmatrix} I_{(N_r \times N_r)} & 0_{(N_r \times N_r)} \\ 0_{((N_a-1)N_r \times N_r)} & 0_{((N_a-1)N_r \times N_r)} \\ 0_{(N_r \times N_r)} & I_{(N_r \times N_r)} \end{bmatrix}. \tag{7.76}$$

Using this decomposition of δP_k, (7.69) can be written

$$\begin{bmatrix} G_{k+1}^H \Gamma_{k+1}^{-1} \\ 0_d \end{bmatrix} = \begin{bmatrix} 0_d \\ G_k \Gamma_k^{-1} \end{bmatrix} + L_k S L_k^H \begin{bmatrix} \tilde{U}_{k+1}^H \\ U_k \end{bmatrix}, \tag{7.77}$$

and (7.73) can be written

$$\Gamma_{k+1}^{-1} = \Gamma_k^{-1} + \begin{bmatrix} \tilde{U}_{k-N_a} & U_k^H \end{bmatrix} L_k S L_k^H \begin{bmatrix} \tilde{U}_{k+1}^H \\ U_k \end{bmatrix}. \tag{7.78}$$

Let Γ_k^{-1} have the "square-root" factorization (this can be accomplished by a Cholesky decomposition or an eigen-decomposition)

$$\Gamma_k^{-1} = \Gamma_k^{-1/2} \Gamma_k^{-H/2}. \tag{7.79}$$

With this factorization (7.77) and (7.78) can be written

$$\begin{bmatrix} G_{k+1}^H \Gamma_{k+1}^{-1/2} \\ 0_d \end{bmatrix} \Gamma_{k+1}^{-H/2} = \begin{bmatrix} 0_d \\ G_k^H \Gamma_k^{-1/2} \end{bmatrix} \Gamma_k^{-H/2} + L_k S L_k^H \begin{bmatrix} \tilde{U}_{k+1}^H \\ U_k \end{bmatrix} \tag{7.80}$$

$$\Gamma_{k+1}^{-1/2} \Gamma_{k+1}^{-H/2} = \Gamma_k^{-1/2} \Gamma_k^{-H/2} + \begin{bmatrix} \tilde{U}_{k+1} & U_k^H \end{bmatrix} L_k S L_k^H \begin{bmatrix} \tilde{U}_{k+1}^H \\ U_k \end{bmatrix} \tag{7.81}$$

Notice that these equations have the form

$$F^H C = D^H A + E^H S B \tag{7.82}$$

$$C^H C = A^H A + B^H S B, \tag{7.83}$$

where

$$\begin{array}{lll} A = \Gamma_k^{-H/2} & B = L_k^H \begin{bmatrix} \tilde{U}_{k+1}^H \\ U_k \end{bmatrix} & C = \Gamma_{k+1}^{-H/2} \\ D = \begin{bmatrix} 0_d^H & \Gamma_k^{-H/2} G_k \end{bmatrix} & E = L_k^H & F = \begin{bmatrix} \Gamma_{k+1}^{-H/2} G_{k+1} & 0_d^H \end{bmatrix}. \end{array} \tag{7.84}$$

In these equations, A, B, D, and E are known and C and F are updated quantities that we wish to obtain. To solve these equations for C and F, form the pre-array

$$\Psi = \begin{bmatrix} A & D \\ B & E \end{bmatrix}, \tag{7.85}$$

then find a J-unitary matrix ($\Theta^H J \Theta = \Theta J \Theta^H = J$, where J is a matrix with ± 1 on the diagonal) such that

$$\Theta \begin{bmatrix} A & D \\ B & E \end{bmatrix} = \begin{bmatrix} X & Y \\ 0 & Z \end{bmatrix}. \tag{7.86}$$

For these equations, the J matrix is given by

$$J = \begin{bmatrix} I_{(sN_n \times sN_n)} & 0 \\ 0 & S \end{bmatrix}. \tag{7.87}$$

If (7.86) is "squared" based on the geometry of the space as given by J, the following equation is obtained

$$\begin{bmatrix} A^H & B^H \\ D^H & E^H \end{bmatrix} \underbrace{\Theta^H J \Theta}_{J} \begin{bmatrix} A & D \\ B & E \end{bmatrix} = \begin{bmatrix} X^H & 0^H \\ Y^H & Z^H \end{bmatrix} J \begin{bmatrix} X & Y \\ 0 & Z \end{bmatrix}. \tag{7.88}$$

By the J-unitary property (and substituting in for J),

$$\begin{bmatrix} A^H & B^H \\ D^H & E^H \end{bmatrix} \begin{bmatrix} I & 0 \\ 0 & S \end{bmatrix} \begin{bmatrix} A & D \\ B & E \end{bmatrix} = \begin{bmatrix} X^H & 0^H \\ Y^H & Z^H \end{bmatrix} \begin{bmatrix} I & 0 \\ 0 & S \end{bmatrix} \begin{bmatrix} X & Y \\ 0 & Z \end{bmatrix}. \tag{7.89}$$

Performing the matrix multiplications,

$$\begin{bmatrix} A^H A + B^H S B & A^H D + B^H S E \\ D^H A + E^H S B & D^H D + E^H S E \end{bmatrix} = \begin{bmatrix} X^H X & X^H Y \\ Y^H X & Y^H Y + Z^H S Z \end{bmatrix}, \tag{7.90}$$

and because Θ is J-norm preserving, it is easily established that $C = X$, $F = Y$, and with a little more work that $Z = L_{k+1}^H$. The updated gain matrix can be obtained from the product $C^{-1}F$. The block FARLS is summarized in Algorithm 7.2 (the Appendix shows how to find the J-unitary matrix Θ for the block FARLS).

7.5.2 Block FARLS Algorithm Results

It is well known that the scalar FARLS algorithm has stability issues. Often it is the hyperbolic rotations or the non-stationarity of the signal that is blamed for this instability (especially if the "forgetting factor" $\lambda < 1$). The block FARLS is subject to these same stability issues due to the fact that it is based on these same reflections and there is not any guarantee on the stationarity of the input.

Despite the stability issues of the FARLS algorithms, our purpose is to solve the normal equations, not to track a changing coefficient vector. Simulations show that the image is formed before any instability of the algorithms presents itself.

To demonstrate the block FARLS algorithm, consider the simulation parameters in

Algorithm 7.2 Block FARLS Algorithm for Stripmap SAR

Initialize:

$U_{-1} = 0_{((N_a+1)N_r \times sN_n)}$
$A_{-1} = I_{(sN_n \times sN_n)}$,
$D_{-1} = 0_{(sN_n \times (N_a+1)N_r)}$,
$$E_{-1} = \sqrt{1/\mu} \begin{bmatrix} I_{(N_r \times N_r)} & 0_{(N_r \times (N_a-1)N_r)} & 0_{(N_r \times N_r)} \\ 0_{(N_r \times N_r)} & 0_{(N_r \times (N_a-1)N_r)} & I_{(N_r \times N_r)} \end{bmatrix},$$
$B_{-1} = E_{-1}U_{-1}$,
$\mathbf{g}_{-1} = 0_{(N_aN_r \times 1)}$ or $\mathbf{g}_{-1} = \mathcal{F}^H\mathbf{d}$

Iterate:

Update the regressors $U_i \rightarrow U_{i+1}$,
$B = EU_{i+1}$,
$$\begin{bmatrix} C & F \\ 0 & Z \end{bmatrix} = \Theta \begin{bmatrix} A & D \\ B & E \end{bmatrix},$$
$G_i = C^{-1}F$,
$\mathbf{g}_i = \mathbf{g}_{i-1} + G_i(\mathbf{d}_i - U_i^H\mathbf{g}_{i-1})$,
Identify the updates for forming the next pre-array:
F (properly shifted) $\rightarrow D$,
$Z \rightarrow E$,
$C \rightarrow A$.

section 6.2. The optimal value of μ is found by selecting a SNR level and numerically finding the value of μ that corresponds to the minimum value of e_μ (as in the simulations for the block RLS).

In the first example, the $SNR = 2$ dB and $\mu_{opt} = 2.5119 \times 10^{-7}$. The ML image is illustrated in figure 7.7 and the image produced by the block FARLS is illustrated in figure 7.8. A visualization of the magnitude (in dB) of the pre-array and the post-array are illustrated for the 35^{th} iteration in figure 7.9 and figure 7.10, respectively. Notice that that the blocks of zeros in F submatrix in the post-array appear where they should.

In the next example, the $SNR = 20$ dB and $\mu_{opt} = 1 \times 10^{-7}$. The ML image is illustrated in figure 7.11 and the image produced by the block FARLS is illustrated in figure 7.12.

7.6 Comparison Between the BRLS and FARLS Methods

In stripmap SAR, usually $N_a >> N_r$ (there are many more azimuth cells than range

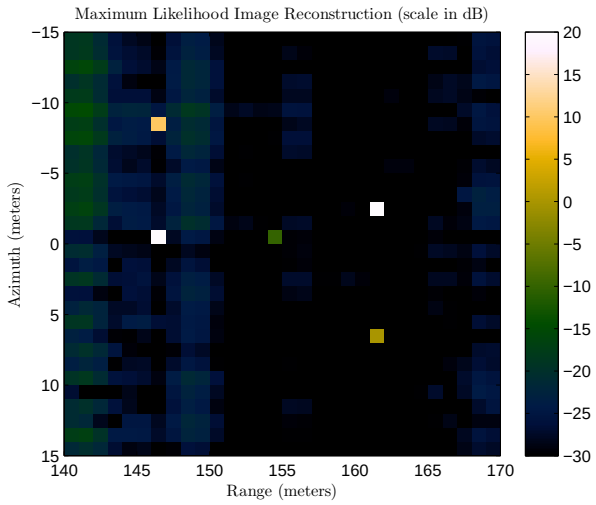

Fig. 7.7: Illustration of the ML image reconstruction (for comparison with the block FARLS image reconstruction) for $SNR = 2$ dB.

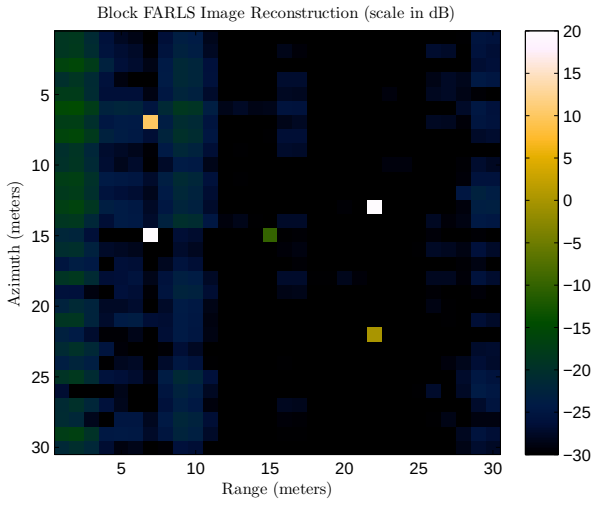

Fig. 7.8: Illustration of the image reconstruction using the block FARLS for $SNR = 2$ dB.

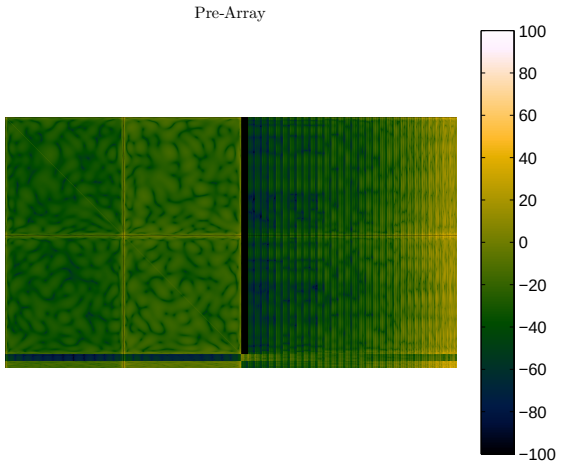

Fig. 7.9: Illustration of the pre-array on iteration 35.

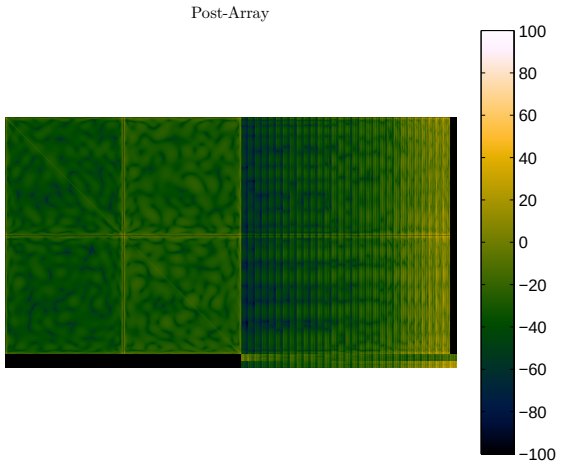

Fig. 7.10: Illustration of the post-array on iteration 35.

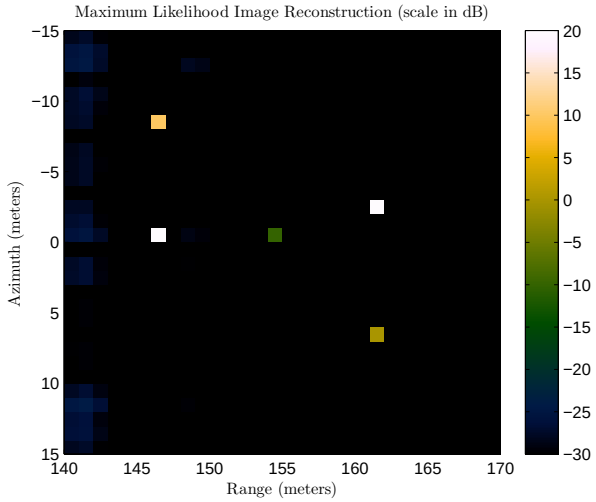

Fig. 7.11: Illustration of the ML image reconstruction (for comparison with the block FARLS image reconstruction) for $SNR = 20$ dB.

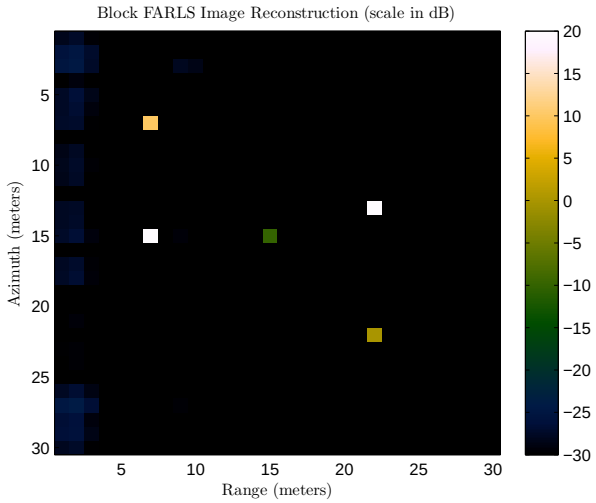

Fig. 7.12: Illustration of the image reconstruction using the block FARLS for $SNR = 20$ dB.

cells in the reconstruction array) and $N_a \leq N_n$ (not every sample in range necessarily constitutes a range cell in the reconstructed image). As an example, let the $PRF = 1000$ Hz, $vT = L/2$ (then N_a is equal to the number of pulses), let $N_n = 2000$ and assume the sampling rate is such that $N_r = N_n$, if SAR data is collected for 20 seconds (a fairly short collection time), then $N_a = 20,000$. It is easy to see how N_a can be much larger than N_r.

The most computational step in the BRLS algorithm is the computation of the matrix product $U_i^H P_{i-1} U_i$ which requires $(N_a N_r)^2 s N_n + (s N_n)^2 N_a N_r$ multiplies on each iteration of the algorithm, thus the computational complexity for the BRLS is $\mathcal{O}((N_a N_r)^2 s N_n)$. The storage requirements for the matrix P can be quite large. If we use the parameters in the example above, then P has dimensions $40,000,000 \times 40,000,000$.

The most computational step in the block FARLS is applying the $2N_r$ transformations to the pre-array to transform it into the post-array. This step in the algorithm is on the order of $\mathcal{O}(N_a N_r^2 s N_n)$. Using the parameters above, the array has dimensions $6,000 \times 40,004,000$.

As can be seen, the computational complexity of the block FARLS is a factor of N_a lower than the BRLS, which is a significant savings. Also, storing the array in the block FARLS requires much less memory than storing the inverse covariance matrix in the BRLS algorithm. Thus, if the assumptions on the data acquisition hold, then a significant savings can be gained by using the block FARLS algorithm.

7.7 Summary

It was shown in this chapter that information on the reflectivity of the scene can be included in the form of prior probabilities and the resulting ground reflectivity estimates are MAP estimates. It was shown that if the prior probabilities are assumed Gaussian, then the MAP estimates can be formed by regularized least-squares algorithms. This chapter developed two algorithms for forming MAP estimates; the first is a new application of the BRLS algorithm and the second uses the structure of the data matrix for an ideal flight and a flat earth model to develop a new block FARLS algorithm. Finally, the two algorithms were compared and it was shown that for an ideal flight and a flat earth model, the block FARLS offers a significant savings (both computational and in memory) over the BRLS.

Chapter 8

Model-Based Stripmap Autofocus

Many autofocus algorithms exist for correcting uncompensated residual phase errors in SAR images. The processing in these algorithms depends on the SAR modality (*e.g.* spotlight, stripmap, etc.). In this chapter a model-based phase error estimation method is developed. It is shown that these phase error estimates can be applied to correct phase errors in stripmap SAR images. The proposed phase estimation method uses classical subspace fitting techniques which are well known in the array processing literature. The novelty in this approach is how the autofocus method is derived from the linear forward model. It is shown that an estimate of the phase error may be obtained without having to form the image. It is also shown that the proposed method is non-iterative in the sense that iterations between the image domain and the range compressed domain are not necessary to obtain the phase error estimates.

8.1 Background

Despite the best efforts to have a SAR sensor follow a predetermined nominal trajectory, phase errors still exist in the collected data that corrupt the azimuth compression of the collected data. It is well known that these phase errors come mainly from two sources, [4, 32, 33]. A low frequency phase error will exist for uncompensated platform deviations from the nominal flight path, which has the effect of broadening the main-lobe of the azimuth compressed signals. Most of the gross platform errors are accounted for via motion compensation algorithms which use available navigational data. However, navigational data has limited accuracy and is corrupted by noise as well. The other source of phase error stems from signal propagation effects. These phase errors tend to be high frequency phase errors and the effect they have is not so much broadening the main lobe of the azimuth

compressed pulse as raising the side-lobes, which lowers the contrast of the image and masks less reflective objects in the image. Autofocus algorithms are data driven algorithms that estimate and correct these phase errors.

Several autofocus algorithms exist, most of which are specific to the particular SAR modality being used (stripmap, spotlight, etc.). Each approach can be further classified as parametric, non-parametric, or metric based. The parametric approaches (such as map-drift) model the phase error as a polynomial or as sinusoidal and use the data to estimate the coefficients (parameters) [4, 33–35]. Because they use the data to estimate the coefficients, they are limited to only reliably estimating a small number of coefficients. Hence, these approaches perform well if the phase error is low frequency, but they fail to model the presence of high frequency phase error. The non-parametric approaches make the assumption that all of the range data collected from a single pulse is corrupted by the same phase error [4, 36, 37]. If this holds, non-parametric techniques are able to estimate both low and high frequency phase errors. Finally, the metric based methods generally assume that the phase error has low frequencies and that it comes from a sensor velocity error. However, they can also be combined with non-parametric methods to produce good results [38, 39]. They utilize a cost function, such as image intensity or neg-entropy, to correct the azimuth matched filter that is applied to azimuth compress the data.

What all these methods have in common is that they must step back in the processing chain (usually azimuth decompression) to where the individual phase errors from each pulse exist to apply the phase compensation. For spotlight SAR, this amounts to computing an azimuth FFT to decompress the azimuth pulses, applying the phase compensation, then re-compressing in azimuth via an inverse FFT. For stripmap SAR, azimuth decompression is not quite so straightforward. The azimuth compression is accomplished by matched filtering. Deconvolving the azimuth matched filter to decompress the image to get back to the range compressed data is an ill-posed problem. Thus the range compressed data must be saved; this is the domain where phase error compensation must take place.

There are a variety of ways in which autofocus is implemented for stripmap SAR. The

development in this chapter is a novel, model-based, non-parametric autofocus algorithm explicitly for stripmap SAR.

8.2 Phase Error Model Development

In the CBP and the ML algorithms, the image is reconstructed to a predetermined reconstruction grid that has N_r range bins and N_a azimuth bins. Usually there is a digital elevation model (DEM) that accompanies the collected SAR and navigational data so the radial distance from the sensor location to each reconstruction point can be determined. Motion compensation due to gross sensor position deviations from the nominal trajectory are easily accounted for in the CBP and ML algorithms, but unknown phase errors due to sensor location uncertainty, DEM errors, and signal propagation errors typically are not. This section derives a model for the phase errors. The development begins by recalling the linear forward model for stripmap SAR that was derived in Chapter 5.

8.2.1 Phase Error Free Model

In Chapter 5 the linear forward model was developed that was used for maximum likelihood (ML) image formation. It was also shown that CBP is the first step in the ML image formation. Here, the same model will be used for phase estimation.

The following is the linear model that was presented in (5.16):

$$\mathbf{d} = \mathcal{F}\mathbf{g} + \boldsymbol{\eta}. \tag{8.1}$$

In (8.1), $\mathcal{F}$ is an $N_nN_k \times N_aN_r$ matrix, $\mathbf{d}$ is an $(N_kN_n \times 1)$ vector, $\mathbf{g}$ is an $(N_aN_r \times 1)$ vector, and $\boldsymbol{\eta}$ is an $N_nN_k \times 1$ vector, where N_k is the number of transmitted pulses, N_n is the number of samples taken from each pulse, N_a is the number of rows in the reconstruction array, and N_r is the number of columns in the reconstruction array.

It was shown in (5.10) that the matrix $\mathcal{F}$ can be decomposed into a vertical stack of N_k $(N_n \times N_a N_r)$ submatrices

$$\mathcal{F} = \left[\begin{array}{c} \mathcal{F}_1 \\ \hline \vdots \\ \hline \mathcal{F}_{N_k} \end{array}\right], \tag{8.2}$$

where the submatrix $\mathcal{F}_k$ is the model of the demodulated sampled returns from the ground locations under the illumination of the antenna based on all navigational data from the k^{th} pulse.

It was also shown in Chapter 5 that the CBP image (in terms of (8.1)) is computed from the matrix/vector product

$$\begin{aligned} \mathbf{g}_{\text{CBP}} &= \mathcal{F}^H \mathbf{d} && (8.3) \\ &= [\mathcal{F}_1^H \mathbf{d}_1 \cdots \mathcal{F}_{N_k}^H \mathbf{d}_{N_k}]\mathbf{1} && (8.4) \\ &= \mathcal{G}\mathbf{1}, && (8.5) \end{aligned}$$

where $\mathbf{d}_k$ is the $N_n \times 1$ vector of collected data from the k^{th} pulse and $\mathbf{1}$ is the vector of all ones.

If the $\mathbf{1}$ vector is replaced by a vector $\boldsymbol{\beta}$, where $\beta_i = e^{j\phi_i}$,

$$\mathbf{g}_{\text{CBP}}(\boldsymbol{\beta}) = \mathcal{G}\boldsymbol{\beta}, \tag{8.6}$$

then if phase errors did exist in the data, then the vector $\boldsymbol{\beta}$ could be found that corrects for the phase error, while simultaneously forming the CBP image.

8.2.2 Phase Error Model

With the assumption that the incidence angle does not vary too much over the region being imaged, and that the uncompensated phase error is not too large, the model for uncompensated phase error in the k^{th} pulse manifests itself as a constant phase multiplier

for all the samples collected from the k^{th} pulse. (If the first assumption does not hold, data from a narrow strip (in range) of the reconstruction grid can be used so that the assumption does hold.) The model for the uncompensated phase error is

$$\mathcal{F}_k(\beta_k) = \Lambda_{\beta_k}\mathcal{F}_k, \tag{8.7}$$

where $\Lambda_{\beta_k} = \beta_k I$ and $\beta_k = e^{j\phi_k}$ is the unknown phase term. Making the assumption that a residual phase error may exist for each pulse, the resulting model becomes

$$\mathcal{F}(\boldsymbol{\beta}) = \Lambda_{\boldsymbol{\beta}}\mathcal{F}, \tag{8.8}$$

where

$$\begin{aligned} \Lambda_{\boldsymbol{\beta}} &= \text{BlockDiag}(\Lambda_{\beta_1}, \cdots \Lambda_{\beta_{N_k}}) && (8.9)\\ &= \text{Diag}(\boldsymbol{\beta}) \otimes I, && (8.10) \end{aligned}$$

where $\otimes$ is the Kronecker product [29]. Multiplying $\mathcal{F}$ on the left by $\Lambda_{\boldsymbol{\beta}}$ in (8.8) changes the range space of $\mathcal{F}$; if $\Lambda_{\boldsymbol{\beta}}$ were multiplying $\mathcal{F}$ on the right, the range space would stay the same (provided $\Lambda_{\boldsymbol{\beta}}$ is full-rank).

Using (8.8) in (8.1), the altered forward model which includes phase errors is

$$\mathbf{d} = \mathcal{F}(\boldsymbol{\beta})\mathbf{g} + \boldsymbol{\eta}. \tag{8.11}$$

In the absence of noise, (8.11) states that $\mathbf{d}$ is contained in the range of $\mathcal{F}(\boldsymbol{\beta})$.

8.3 Subspace Fitting Autofocus

If the residual phase is not compensated for, the resulting formed image will not be in focus and will have poor contrast. The proposed method provides a vector $\hat{\boldsymbol{\beta}}$ of phase correction terms such that $[\hat{\boldsymbol{\beta}}]_i = \hat{\beta}_i$, which is an estimate of β_i. The proposed method for estimating $\boldsymbol{\beta}$ uses subspace fitting principles that are well known in array processing

literature [40].

8.3.1 Subspace Fitting Autofocus Derivation

In Chapter 6, the ML image estimation reduces to the problem

$$\text{minimize } J(\mathbf{g}) = ||\mathcal{F}\mathbf{g} - \mathbf{d}||_2^2. \tag{8.12}$$

Using (8.11), (8.12) can be altered to include the phase errors

$$\text{min. } J(\mathbf{g}, \boldsymbol{\beta}) = ||\mathcal{F}(\boldsymbol{\beta})\mathbf{g} - \mathbf{d}||_2^2 \quad \text{subject to} \quad |\beta_i| = 1. \tag{8.13}$$

Equation (8.13) can be minimized with respect to $\mathbf{g}$ and $\boldsymbol{\beta}$ separately. Minimizing first over $\mathbf{g}$, the estimate for the coefficient vector is the least-squares solution

$$\hat{\mathbf{g}} = (\mathcal{F}^H(\boldsymbol{\beta})\mathcal{F}(\boldsymbol{\beta}))^{-1}\mathcal{F}^H(\boldsymbol{\beta})\mathbf{d}. \tag{8.14}$$

Substituting (8.14) into (8.13), the problem becomes

$$\text{min. } J(\boldsymbol{\beta}) = ||(I - P_{\mathcal{F}(\boldsymbol{\beta})})\mathbf{d}||_2^2 \quad \text{s.t.} \quad |\beta_i| = 1, \tag{8.15}$$

where

$$P_{\mathcal{F}(\boldsymbol{\beta})} = \mathcal{F}(\boldsymbol{\beta})(\mathcal{F}^H(\boldsymbol{\beta})\mathcal{F}(\boldsymbol{\beta}))^{-1}\mathcal{F}^H(\boldsymbol{\beta}) \tag{8.16}$$

is the orthogonal projection matrix constructed from $\mathcal{F}(\boldsymbol{\beta})$. In (8.15) the concept of subspace fitting is apparent: it measures the projection of $\mathbf{d}$ onto the subspace orthogonal to the range space of $\mathcal{F}(\boldsymbol{\beta})$ for a given $\boldsymbol{\beta}$. By the model in (8.11), $\mathbf{d}$ is in the range of $\mathcal{F}(\boldsymbol{\beta})$ for the true $\boldsymbol{\beta}$, so the norm in (8.15) should be small. The minimization problem in (8.15) is to find the vector $\boldsymbol{\beta}$ that brings the subspace closest to $\mathbf{d}$ by minimizing the out-of-subspace distance.

Expanding the norm gives

$$\text{min. } J(\boldsymbol{\beta}) = \mathbf{d}^H\mathbf{d} - \mathbf{d}^H P^H_{\mathcal{F}(\boldsymbol{\beta})}\mathbf{d} - \mathbf{d}^H P_{\mathcal{F}(\boldsymbol{\beta})}\mathbf{d} + \mathbf{d}^H P^H_{\mathcal{F}(\boldsymbol{\beta})} P_{\mathcal{F}(\boldsymbol{\beta})}\mathbf{d} \quad \text{s.t.} \quad |\beta_i| = 1. \tag{8.17}$$

Using the following properties of projection matrices, $P^H_{\mathcal{F}(\boldsymbol{\beta})} = P_{\mathcal{F}(\boldsymbol{\beta})}$ and $P^2_{\mathcal{F}(\boldsymbol{\beta})} = P_{\mathcal{F}(\boldsymbol{\beta})}$, this reduces to

$$\text{min. } J(\boldsymbol{\beta}) = \mathbf{d}^H\mathbf{d} - \mathbf{d}^H P_{\mathcal{F}(\boldsymbol{\beta})}\mathbf{d} \quad \text{s.t.} \quad |\beta_i| = 1. \tag{8.18}$$

The first term in (8.18) does not depend on $\boldsymbol{\beta}$ and by changing the sign of the second term, the minimization can be restated as the following maximization problem

$$\hat{\boldsymbol{\beta}} = \arg\max_{\boldsymbol{\beta}} \mathbf{d}^H P_{\mathcal{F}(\boldsymbol{\beta})}\mathbf{d} \quad \text{s.t.} \quad |\beta_i| = 1. \tag{8.19}$$

To move beyond this point, it is necessary to look at the structure of $P_{\mathcal{F}(\boldsymbol{\beta})}$. Using the definition of $\mathcal{F}(\boldsymbol{\beta})$ in (8.8)

$$\begin{aligned} P_{\mathcal{F}(\boldsymbol{\beta})} &= \mathcal{F}(\boldsymbol{\beta})(\mathcal{F}^H(\boldsymbol{\beta})\mathcal{F}(\boldsymbol{\beta}))^{-1}\mathcal{F}^H(\boldsymbol{\beta}) && (8.20)\\ &= \Lambda_{\boldsymbol{\beta}}\mathcal{F}(\mathcal{F}^H\Lambda^H_{\boldsymbol{\beta}}\Lambda_{\boldsymbol{\beta}}\mathcal{F})^{-1}\mathcal{F}^H\Lambda^H_{\boldsymbol{\beta}} && (8.21)\\ &= \Lambda_{\boldsymbol{\beta}}\mathcal{F}(\mathcal{F}^H\mathcal{F})^{-1}\mathcal{F}^H\Lambda^H_{\boldsymbol{\beta}}, && (8.22) \end{aligned}$$

where, due to its construction, $\Lambda^H_{\boldsymbol{\beta}}\Lambda_{\boldsymbol{\beta}} = I$. Thus, (8.19) becomes

$$\hat{\boldsymbol{\beta}} = \arg\max_{\boldsymbol{\beta}} \mathbf{d}^H\Lambda_{\boldsymbol{\beta}}\mathcal{F}(\mathcal{F}^H\mathcal{F})^{-1}\mathcal{F}^H\Lambda^H_{\boldsymbol{\beta}}\mathbf{d} \quad \text{s.t.} \quad |\beta_i| = 1. \tag{8.23}$$

Because $\Lambda_{\boldsymbol{\beta}}$ is a diagonal matrix, its diagonal and $\mathbf{d}$ can be swapped

$$\Lambda^H_{\boldsymbol{\beta}}\mathbf{d} = \Lambda_{\mathbf{d}} I_{\mathbf{1}}\boldsymbol{\beta}^*, \tag{8.24}$$

where $I_{\mathbf{1}} = I \otimes \mathbf{1}$. Using the structure of $\mathbf{d}$ in (8.5), the product of $\Lambda_{\mathbf{d}} I_{\mathbf{1}}$ is

$$\Lambda_{\mathbf{d}} I_{\mathbf{1}} = \text{BlockDiag}(\mathbf{d}_1, \ldots, \mathbf{d}_{N_k}). \tag{8.25}$$

Substituting this result into (8.23) and using (8.2) and (8.5) gives

$$\begin{aligned} \hat{\boldsymbol{\beta}} &= \arg\max_{\boldsymbol{\beta}} \boldsymbol{\beta}^T \left[\mathcal{G}^H (\mathcal{F}^H \mathcal{F})^{-1} \mathcal{G}\right] \boldsymbol{\beta}^* \quad \text{s.t.} \quad |\beta_i| = 1 && (8.26) \\ &= \arg\max_{\boldsymbol{\beta}} \boldsymbol{\beta}^T \mathcal{M} \boldsymbol{\beta}^* \quad \text{s.t.} \quad |\beta_i| = 1, && (8.27) \end{aligned}$$

where $\mathcal{G}$ is defined in (8.5) and $\mathcal{M} = \mathcal{G}^H (\mathcal{F}^H \mathcal{F})^{-1} \mathcal{G}$. From (8.27) it is apparent that the image does not need to be formed to estimate $\boldsymbol{\beta}$.

8.3.2 Subspace Fitting Autofocus Optimization Strategy

At first glance, optimizing (8.27) may seem like an eigenvector problem, but it is important to note that the optimization in (8.27) is not as simple as finding the eigenvector associated with the largest eigenvalue of $\mathcal{M}$, because this method does not capture the constraint $|\beta_i| = 1$.

Recall that $\beta_i = e^{j\phi_i}$, using this, the constrained problem in (8.27) may be equivalently written as the unconstrained problem

$$\hat{\boldsymbol{\phi}} = \arg\max_{\boldsymbol{\phi}} e^{j\boldsymbol{\phi}^T} \mathcal{M} e^{-j\boldsymbol{\phi}}, \tag{8.28}$$

where $[e^{\pm j\boldsymbol{\phi}}]_i = e^{\pm j\phi_i}$. Equation (8.28) can be maximized by a number of different methods. The optimization methods that will be explored in this chapter are gradient ascent, a regularized Newton's method, and a method that uses the convexity of the linearization of (8.27).

Optimization by Gradient Ascent

Let the objective function to be maximized be denoted as

$$J(\boldsymbol{\phi}) = e^{j\boldsymbol{\phi}^T}\mathcal{M}e^{-j\boldsymbol{\phi}} \tag{8.29}$$

$$= \mathbf{u}(\boldsymbol{\phi})^T\mathcal{M}\mathbf{v}(\boldsymbol{\phi}). \tag{8.30}$$

Using the chain-rule, the gradient of (8.29) is (note that $\mathcal{M}^H = \mathcal{M}$ thus $\mathcal{M}^T = \mathcal{M}^*$)

$$\frac{\partial J}{\partial \boldsymbol{\phi}} = \frac{\partial \mathbf{u}^T}{\partial \boldsymbol{\phi}}\left.\frac{\partial J}{\partial \mathbf{u}}\right|_{\mathbf{u}=e^{j\boldsymbol{\phi}}} + \frac{\partial \mathbf{v}^T}{\partial \boldsymbol{\phi}}\left.\frac{\partial J}{\partial \mathbf{v}}\right|_{\mathbf{v}=e^{-j\boldsymbol{\phi}}} \tag{8.31}$$

$$= j\text{Diag}\left(e^{j\boldsymbol{\phi}}\right)\mathcal{M}e^{-j\boldsymbol{\phi}} - j\text{Diag}\left(e^{-j\boldsymbol{\phi}}\right)\mathcal{M}^*e^{j\boldsymbol{\phi}} \tag{8.32}$$

$$= 2\Re\left\{j\text{Diag}(e^{j\boldsymbol{\phi}})\mathcal{M}e^{-j\boldsymbol{\phi}}\right\}. \tag{8.33}$$

Thus, the update rule for the gradient ascent method is

$$\boldsymbol{\phi}_{n+1} = \boldsymbol{\phi}_n + \mu 2\Re\left\{j\text{Diag}(e^{j\boldsymbol{\phi}_n})\mathcal{M}e^{-j\boldsymbol{\phi}_n}\right\}, \tag{8.34}$$

where $\boldsymbol{\phi}_0 = \mathbf{0}$ (assume no phase error) and μ is a step-size parameter.

The step size μ in the gradient can be a fixed value, or it can be found by a line search method [41]. Fixing a value of μ is the least computational, however it may require more iterations to reach the maximum value than computing a line search.

Optimization by Newton's Method

Newton's method requires the Hessian matrix, which is the matrix of second partial derivatives. Using the linearity properties of partial derivatives and $\Re\{\cdot\}$ and the results

from (8.33), the i^{th} column of the Hessian is

$$\begin{aligned} H_{(:,i)} &= \frac{\partial^2 J}{\partial \boldsymbol{\phi} \partial \phi_i} && (8.35)\\ &= 2\Re\left\{ j \frac{\partial}{\partial \phi_i} \mathrm{Diag}(e^{j\boldsymbol{\phi}}) \mathcal{M} e^{-j\boldsymbol{\phi}} \right\} && (8.36)\\ &= 2\Re\left\{ j \left(j e^{j\phi_i} \mathcal{E}_{ii} \mathcal{M} e^{-j\boldsymbol{\phi}} - j e^{-j\phi_i} \mathrm{Diag}(e^{j\boldsymbol{\phi}}) \mathcal{M} \mathbf{e}_i \right) \right\} && (8.37)\\ &= 2\Re\left\{ e^{-j\phi_i} \mathrm{Diag}(e^{j\boldsymbol{\phi}}) \mathcal{M} \mathbf{e}_i - e^{j\phi_i} \mathcal{E}_{ii} \mathcal{M} e^{-j\boldsymbol{\phi}} \right\} && (8.38)\\ &= 2\Re\left\{ e^{-j\phi_i} \mathrm{Diag}(e^{j\boldsymbol{\phi}}) \mathcal{M}_{(:,i)} - e^{j\phi_i} (\mathcal{M}_{(i,:)} e^{-j\boldsymbol{\phi}}) \mathbf{e}_i \right\}, && (8.39) \end{aligned}$$

where $\mathcal{E}_{ii}$ is the matrix that has a one in the $(i,i)^{th}$ entry and is zero everywhere else. Writing out a few columns of H reveals that the structure of the Hessian is

$$H = 2\Re\left\{ \mathrm{Diag}(e^{j\boldsymbol{\phi}}) \mathcal{M} \mathrm{Diag}(e^{-j\boldsymbol{\phi}}) - \mathrm{Diag}(\mathcal{M} e^{-j\boldsymbol{\phi}}) \mathrm{Diag}(e^{j\boldsymbol{\phi}}) \right\}. \tag{8.40}$$

The Hessian matrix is not full rank; it has a null-space spanned by the all-ones vector, $\mathbf{1}$. Thus, H is not invertible and the Newton step cannot be computed. However, a *regularized* Hessian matrix computed as

$$\tilde{H} = 2\Re\left\{ \mathrm{Diag}(e^{j\boldsymbol{\phi}}) \mathcal{M} \mathrm{Diag}(e^{-j\boldsymbol{\phi}}) - \mathrm{Diag}(\mathcal{M} e^{-j\boldsymbol{\phi}}) \mathrm{Diag}(e^{j\boldsymbol{\phi}}) - \tilde{\mathcal{M}} \right\} \tag{8.41}$$

is invertible, where $\tilde{\mathcal{M}}$ is a diagonal matrix that has the diagonal elements of $\mathcal{M}$ as its entries. Using this regularized Hessian matrix, the regularized Newton update rule is

$$\boldsymbol{\phi}_{n+1} = \boldsymbol{\phi}_n - \tilde{H}^{-1} \frac{\partial J}{\partial \boldsymbol{\phi}}. \tag{8.42}$$

As part of the regularization, after each update if $|[\boldsymbol{\phi}_n]_i| \geq \pi$ then that value is set to zero.

Convex Optimization of Linearized Objective Function

The problem as stated in (8.27) does not fit the criterion for a convex optimization problem. The first reason is that while the objective function

$$f_0(\boldsymbol{\beta}) = \boldsymbol{\beta}^T \mathcal{M} \boldsymbol{\beta}^* \tag{8.43}$$

is a convex function, the tools for convex optimization do not support *maximizing* a convex function. The other reason (8.27) is not a convex problem is that the constraints $|\beta_i| = 1$ are not convex, either. It is important to note that if the domain of a convex function is convex, then the maximum value of the convex function will occur on the boundary of its domain. With this in mind, the non-convex constraints can be relaxed to $|\beta_i| \leq 1$, which are convex. Thus, the optimization problem can be relaxed to

$$\hat{\boldsymbol{\beta}} = \arg\max_{\boldsymbol{\beta} \in \mathcal{D}} \boldsymbol{\beta}^T \mathcal{M} \boldsymbol{\beta}^*, \text{ where } \mathcal{D} = \{\beta_i \mid |\beta_i| \leq 1\}. \tag{8.44}$$

However this does not help overcome the fact that a convex function cannot be maximized via convex optimization tools.

Since (8.43) is differentiable and convex and the (relaxed) domain is convex, the following statement about the linearization (by a truncated Taylor series expansion) about a point $\boldsymbol{\beta}_0 \in \mathcal{D}$ is true [41]

$$f_0(\boldsymbol{\beta}) \geq f_0(\boldsymbol{\beta}_0) + \Re\left\{\nabla f_0(\boldsymbol{\beta}_0)^H (\boldsymbol{\beta} - \boldsymbol{\beta}_0)\right\}. \tag{8.45}$$

Equation (8.45) states that $f_0(\boldsymbol{\beta})$ will always be greater than or equal to the tangent hyperplane at $\boldsymbol{\beta}_0$. The reason this helps in the development is that the tangent plane is both convex *and* concave and the tools for convex optimization will allow for maximizing a concave function over a convex domain. Let $t = f_0(\boldsymbol{\beta})$, then rearranging (8.45) gives

$$0 \geq \Re\left\{ \begin{bmatrix} \nabla f_0(\boldsymbol{\beta}_0)^H & -1 \end{bmatrix} \begin{bmatrix} \boldsymbol{\beta} - \boldsymbol{\beta}_0 \\ t - f_0(\boldsymbol{\beta}_0) \end{bmatrix} \right\}. \tag{8.46}$$

Equation (8.46) describes a halfspace. The tangent plane at $\boldsymbol{\beta}_0$ is the boundary of this halfspace and is achieved at equality

$$0 = \Re \left\{ \begin{bmatrix} \nabla f_0(\boldsymbol{\beta}_0)^H & -1 \end{bmatrix} \begin{bmatrix} \boldsymbol{\beta} - \boldsymbol{\beta}_0 \\ t - f_0(\boldsymbol{\beta}_0) \end{bmatrix} \right\}, \tag{8.47}$$

which can also be written as

$$t = \Re \left\{ \nabla f_0(\boldsymbol{\beta}_0)^H (\boldsymbol{\beta} - \boldsymbol{\beta}_0) \right\} + f_0(\boldsymbol{\beta}_0). \tag{8.48}$$

In (8.47), $\boldsymbol{\beta}$ is a point in the domain and t is the "vertical" coordinate. From this perspective, the linearized optimization problem is to maximize the vertical direction on the tangent plane subject to staying in the domain. Using the definition of t in (8.48), defining $\mathbf{z} = \boldsymbol{\beta} - \boldsymbol{\beta}_0$ (then $\boldsymbol{\beta} = \mathbf{z} + \boldsymbol{\beta}_0$), and noting that $f_0(\boldsymbol{\beta}_0)$ is a constant and does not affect the optimization, the optimization problem *linearized* about $\boldsymbol{\beta}_0$ can be stated as

$$\text{maximize} \qquad \Re \left\{ \nabla f_0(\boldsymbol{\beta}_0)^H \mathbf{z} \right\} \tag{8.49}$$

$$\text{s.t.} \qquad |z_i + \beta_{0,i}| \leq 1, \ \forall i. \tag{8.50}$$

This *linearized* optimization problem needs to be iterated to find the global maximum. Each iteration produces a new vector,

$$\boldsymbol{\beta}_n = \mathbf{z}_{n-1} + \boldsymbol{\beta}_{n-1}, \tag{8.51}$$

that is on the constraint boundary (due to (8.50)). It is well known that moving in a direction with a positive directional derivative (from the point the gradient is computed at) is a move uphill, thus $f_0(\boldsymbol{\beta}_n) \geq f_0(\boldsymbol{\beta}_{n-1})$ (due to (8.49)).

8.4 Results of Proposed Autofocus Methods

This section demonstrates the proposed methods and compares the optimization strategies on simulated data. The data collected have the phase error shown in figure 8.1. Figure 8.2 shows the original image the data is collected from. The image contains three strong point reflectors and four weaker point reflectors in a Gaussian background. Figure 8.3 shows the reconstruction using the CBP algorithm without any phase correction and figure 8.4 shows the ML reconstruction. The three reflectors are visible, but significant blurring in azimuth is apparent.

In the optimization methods that follow, only the phase errors that affect the strong reflectors will be estimated. This demonstrates that this autofocus method can be used for focusing an arbitrary patch of the image.

8.4.1 Results Using Gradient Ascent

The gradient ascent method works very well, however many iterations are needed to get good enough phase estimates so that the resulting image is in focus. This section demonstrates the gradient ascent method for the simulation described above with the step-size $\mu = 1.3 \times 10^{-7}$.

The top of figure 8.5 shows the phase estimates after $100,000$ iterations and the bottom shows the phase estimate error (note that a constant phase error does not adversely effect the reconstruction). Figure 8.6 shows the norm of the gradient versus the iteration number. Finally, figure 8.7 and figure 8.8 illustrate the CBP and ML reconstructions (respectively) after applying the phase estimates.

8.4.2 Results Using Regularized Newton's Method

Compared to the gradient ascent method, the regularized Newton's method requires orders of magnitude fewer iterations to obtain good phase estimates. This section demonstrates the regularized Newton's method for the simulation described above.

The top of figure 8.9 shows the phase estimates after $1,000$ iterations and the bottom shows the phase estimate error (recall that a constant phase error does not adversely effect

the reconstruction). Figure 8.10 shows the norm of the Newton step versus the iteration number. Finally, figure 8.11 and figure 8.12 illustrate the CBP and ML reconstructions (respectively) after applying the phase estimates.

8.4.3 Results Using Convex Optimization

The software package `CVX` [42] was used to obtain the solution for the convex optimization in each iteration. Compared to the gradient ascent method, he linearized convex optimization method requires orders of magnitude fewer iterations to obtain good phase estimates. Compared to the regularized Newton's method, it requires the same order of magnitude iterations. This section demonstrates the linearized convex optimization method for the simulation described above.

The top of figure 8.13 shows the phase estimates after 500 iterations and the bottom shows the phase estimate error (recall that a constant phase error does not adversely effect the reconstruction). Figure 8.14 shows the norm of the step taken each iteration versus the iteration number (the drop-outs are the iterations where `CVX` could not find a solution). Finally, figure 8.15 and figure 8.16 illustrate the CBP and ML reconstructions (respectively) after applying the phase estimates.

8.5 Comparison of Optimization Strategies

This section discusses the results of the three optimization strategies and discusses the advantages and disadvantages of the different methods. This section concludes by comparing the computational complexity of the different methods.

8.5.1 Optimization Results

It is clear from the figures above that each optimization method is able to estimate the phase errors well enough to form a focused CBP and ML image. It is interesting to note the phase estimates from the three methods.

In figure 8.5, it is clear that the gradient ascent method has a difficult time estimating the first and last few phase estimates. However, the phase estimates in between are very

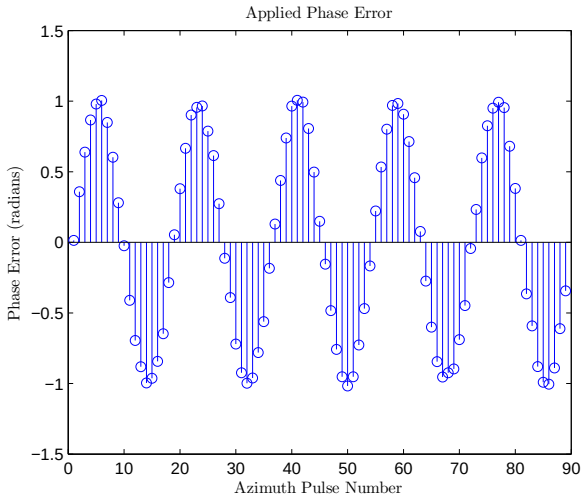

Fig. 8.1: Illustration of the applied phase error.

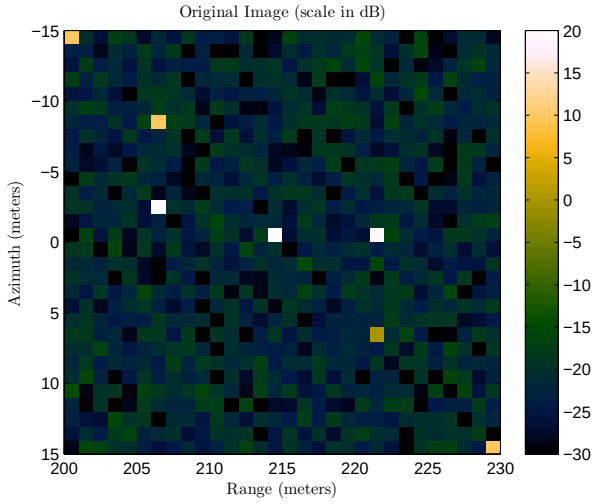

Fig. 8.2: Illustration of the original image.

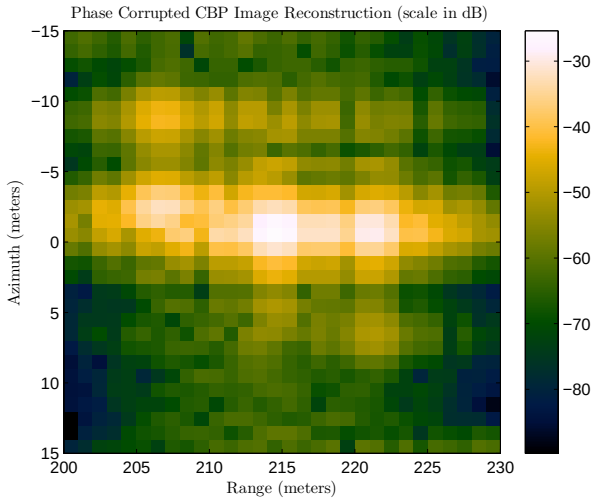

Fig. 8.3: CBP reconstruction without phase compensation.

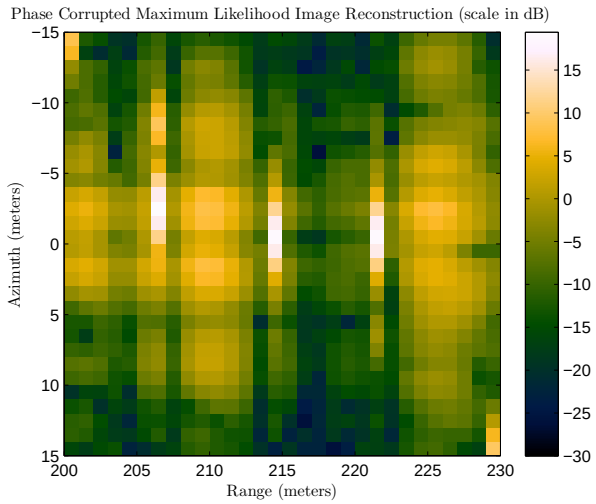

Fig. 8.4: ML reconstruction without phase compensation.

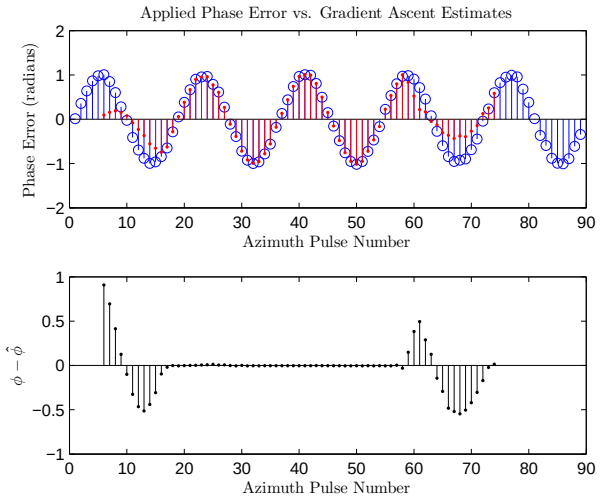

Fig. 8.5: Top: Illustration of the gradient ascent method phase error estimates after $100,000$ iterations. Bottom: Illustration of the phase estimate error.

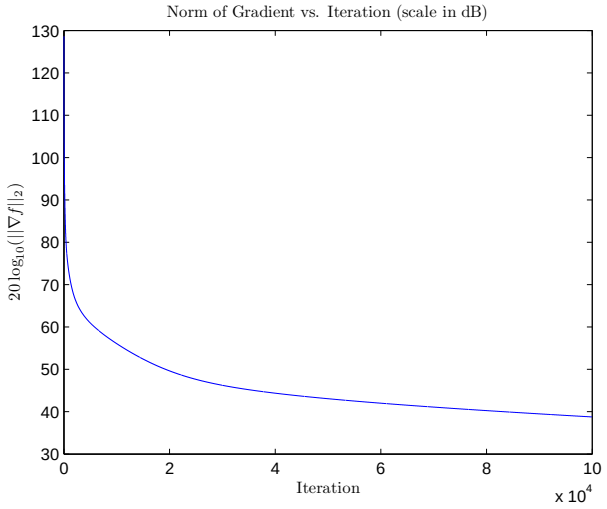

Fig. 8.6: Illustration of the norm of the gradient versus iteration number.

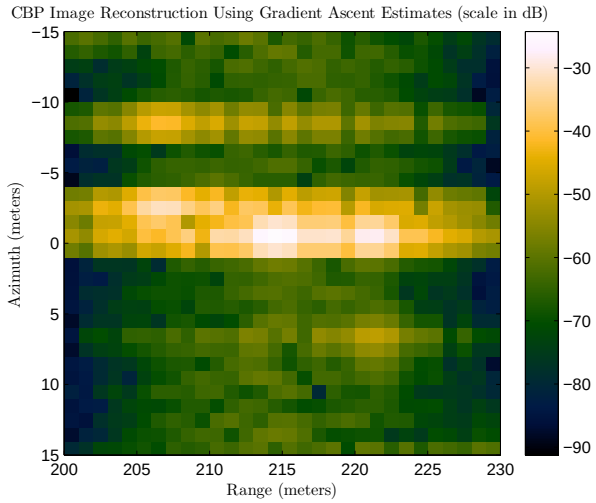

Fig. 8.7: CBP reconstruction after applying the phase estimates from the gradient ascent method. Compare to figure 8.3.

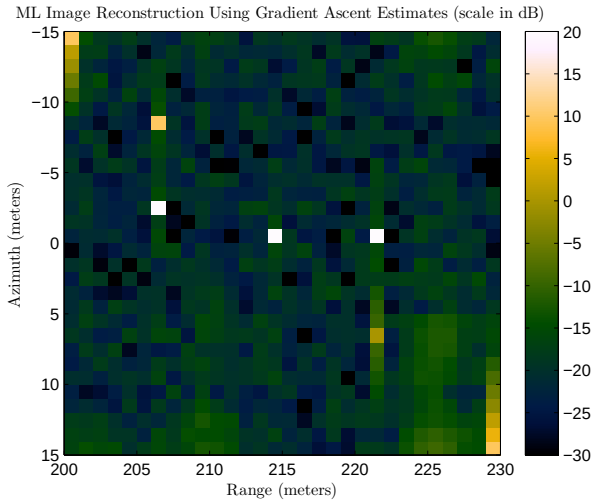

Fig. 8.8: ML reconstruction after applying the phase estimates from the gradient ascent method. Compare to figure 8.4.

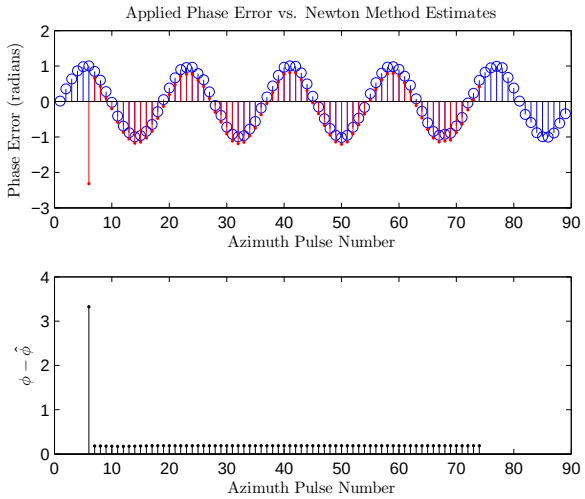

Fig. 8.9: Top: Illustration of the regularized Newton method phase error estimates after $1,000$ iterations. Bottom: Illustration of the phase estimate error.

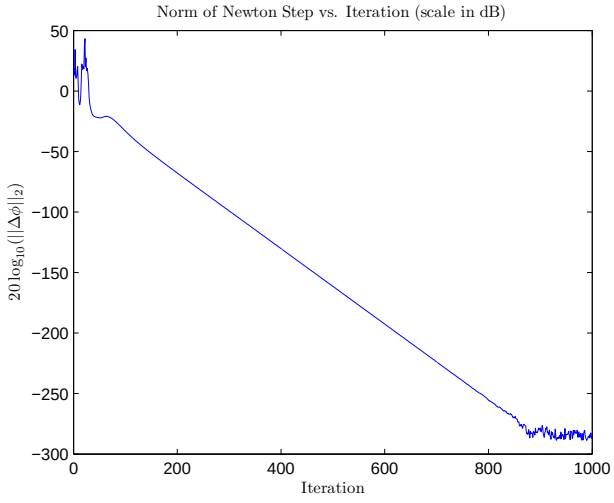

Fig. 8.10: Illustration of the norm of the regularized Newton step versus iteration number.

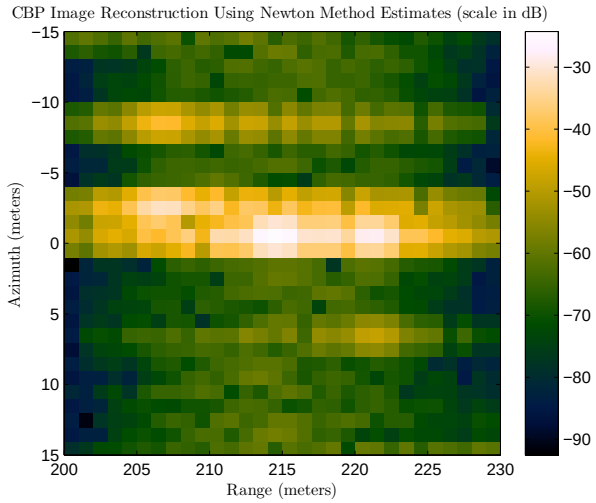

Fig. 8.11: CBP reconstruction after applying the phase estimates from the regularized Newton method. Compare to figure 8.3.

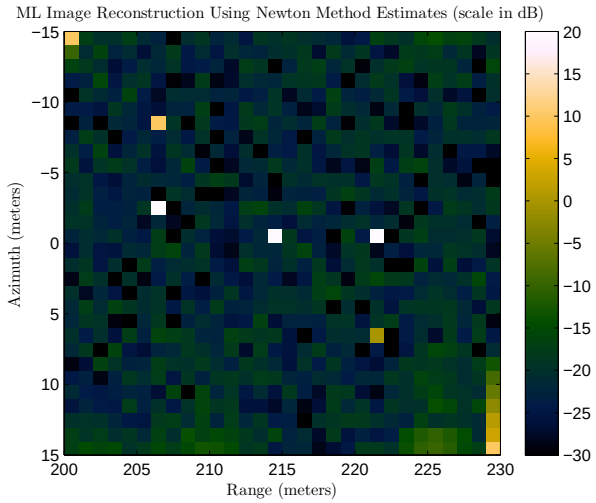

Fig. 8.12: ML reconstruction after applying the phase estimates from the regularized Newton method. Compare to figure 8.4.

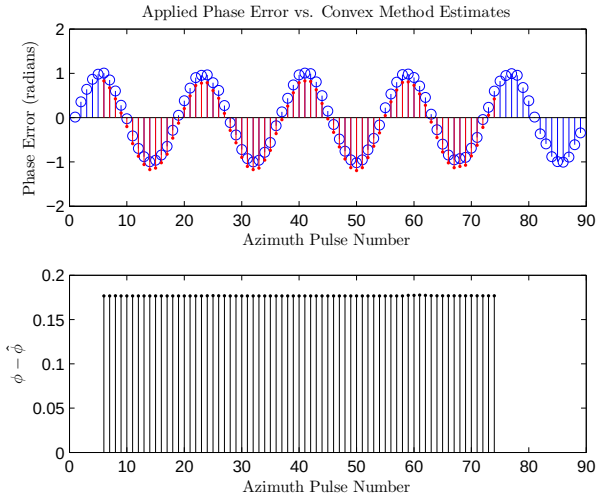

Fig. 8.13: Top: Illustration of the linearized convex method phase error estimates after 500 iterations. Bottom: Illustration of the phase estimate error.

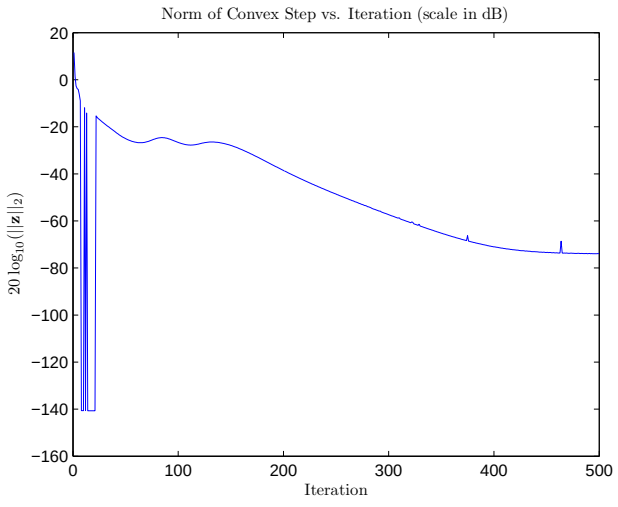

Fig. 8.14: Illustration of the norm of the step taken each iteration versus iteration number for the linearized convex method.

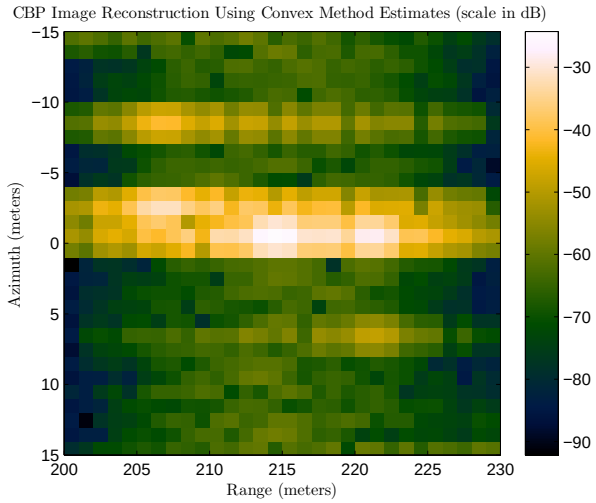

Fig. 8.15: CBP reconstruction after applying the phase estimates from the linearized convex method. Compare to figure 8.3.

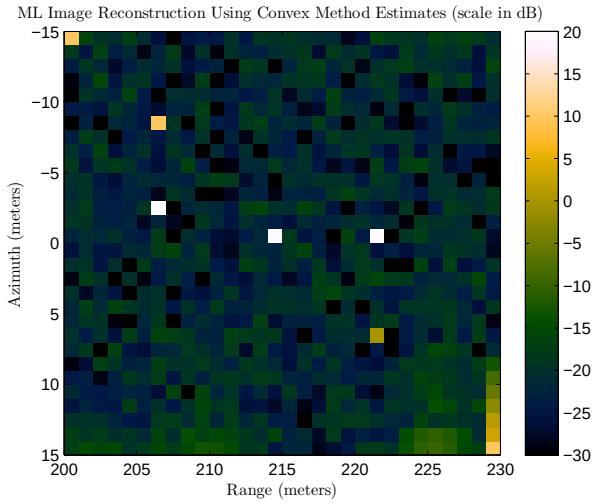

Fig. 8.16: ML reconstruction after applying the phase estimates from the linearized convex method. Compare to figure 8.4.

good. If the number of iterations is increased, the first and last few estimates become better. The gradient ascent method will obtain the solution when the norm of the gradient is zero, however it is can be seen from the slope of the curve in figure 8.6 that the convergence of the norm of the gradient to zero is very slow. From the different simulations that were tried, the gradient ascent method seemed to be the most robust; difficult problems took more iterations, but if the algorithms was allowed to run long enough, good estimates were obtained.

In figure 8.9, it is clear that all the phase estimates (except the first) are very good. It can be seen in figure 8.10 that the convergence of the regularized Newton method is very fast. This method is not quite as robust as the gradient ascent method. The reconstructions were not always better than those obtained using the gradient ascent method for some of the more challenging simulations. In these more challenging cases, the norm of the Newton step still converged quickly to zero, however the phase estimates were not very good. It seems that the choice of the regularization is too dominant in some of the more challenging problems, and the estimated solution is pulled too far away from the true solution.

In figure 8.13, it is clear that all the phase estimates are very good. It can be seen in figure 8.14 that the norm of the step of each iteration starts to converge to zero slowly at higher iterations. However, the step lengths at higher iterations are very small (compared to the gradient ascent method) so that for all practical purposes, the phase estimates are obtained. The convex optimization solver that was used for each iteration was sensitive to the conditioning of $\mathcal{M}$. There are often times the solver could not obtain a solution for one iteration, but it would work just fine for the next; the better the conditioning of $\mathcal{M}$, the less this happened. Good phase estimates were usually obtained if the method were allowed to run long enough.

8.5.2 Comparison of Computational Complexity

It is well known that each iteration of the gradient ascent has complexity $\mathcal{O}(N)$ and each iteration of the Newton method has complexity $\mathcal{O}(N^3)$. It is difficult to quantify the order of complexity of each iteration of the convex optimization method. If a log-barrier

convex optimization solver were tailored to the optimization problem, then the complexity would be $\mathcal{O}(N)$. The `CVX` package uses many different methods to solve convex optimization problems, and it is not clear if the methods use the structure of the objective function and the constraints to reduce the computational complexity of obtaining the solution for each iteration.

It is clear from figure 8.10 that the regularized Newton method converges very quickly. Although each iteration may be more computational, the Newton method may be a better choice than the gradient ascent method because the total computational burden may be less. If a tailored log-barrier solver were used for the linearized convex optimization method, then the clear choice would be to use the convex optimization method because a solution is found in about as many iterations as the Newton method, but the computational complexity is that of the gradient ascent method.

8.6 Summary

This chapter showed that under the certain assumptions, model-based autofocus for stripmap SAR is a constrained subspace fitting problem. It was also shown that the phase error estimates can be obtained without forming the image or iterating between the image and data domains. The optimization methods that were used to obtain the phase estimates were the gradient ascent method, a regularized Newton method, and a linearized convex optimization method. A comparison of these methods was also given and the computational complexity of each was also discussed.

Chapter 9

Summary and Future Work

This chapter summarizes the important elements of each chapter in this dissertation and the contributions made to stripmap SAR. This chapter also extends some of the contributions and suggests ideas for future work in model-based stripmap SAR processing.

9.1 Summary

This section covers the important concepts contained in each chapter and summarizes the contributions made. Chapters 2-4 covered the theoretical foundations of pulsed SAR systems. The forward model for stripmap SAR was derived in Chapter 5 and it was shown that the forward model is linear in the ground reflectivity parameters. The ML image formation method was derived in Chapter 6 and it was shown that CBP is one of the necessary steps in forming the ML image. Two MAP image formation methods were derived in Chapter 7 and it was shown that under the right set of assumptions that MAP methods have a close connection to regularized least-squares algorithms. Finally, a model-based autofocus method was derived in Chapter 8 and it was shown that the model-based autofocus method is a constrained subspace fitting problem.

Chapter 2 covered the concept of resolution, which is the ability to distinguish between closely spaced reflectors. The concept of using pulse compression to obtain increased resolution was also covered.

The role of the antenna in SAR systems was introduced in Chapter 3 and it was shown that the motion and attitude of the SAR sensor, which relates to the pointing direction of the antenna, could be modeled by coordinate rotations and translations. The derivation of the induced azimuth signal and a discussion of the bandwidth of this signal, which determines the choice of the PRF for a pulse SAR system, were also covered in this chapter. A model

for the sampled data was presented in this chapter and it was shown that each collected sample contains information about reflectors on the ground in a neighborhood defined by the pulse duration and the antenna azimuth beamwidth. The last topics covered in this chapter were the resolvability of the SAR sensor, the PSF of the SAR imaging system, and IPI which is an artifact that leaves large star-like patterns around strong reflectors in the formed image and is caused by the choice of the SAR image formation algorithm.

The concepts from Chapter 3 were made explicit for pulsed LFM stripmap SAR in Chapter 4. The first azimuth nulls of the antenna pattern were suggested as the effective azimuth antenna beamwidth. Based on the azimuth beamwidth, the range dependent synthetic aperture length and the time duration that a reflector is under the illumination of the antenna were also discussed. The time a reflector is under the illumination of the antenna leads to the effective bandwidth of the induced signal. The resolution limits for an ideal flight stripmap SAR were stated. Finally, the necessary steps for image formation were discussed; which are range compression, RCMC, and azimuth compression.

The forward model for stripmap SAR was derived in Chapter 5; this comprehensive forward model is a new contribution to stripmap SAR and formed the foundation for all other research in this dissertation. It was shown that the forward model is linear in the ground reflectivity parameters. The fact that the received signal is collected in the presence of thermal AWGN was also discussed and it was shown that the AWGN becomes circularly symmetric AWGN after the received signal is quadrature demodulated and sampled. Including the noise process, it was also shown that the forward model can also be interpreted as a linear statistical model. It was also shown that the forward model can be generated for a user-defined region of interest and that the bounds of the region of interest, the region of interest closure, are controlled by the transmitted pulse duration and the effective antenna azimuth beamwidth.

In Chapter 6, the interpretation of the forward model as a linear statistical model was used to derive the ML image formation method; the ML image formation method (based on the forward model) is also a new contribution to stripmap SAR. It was shown that

forming the ML image is a least-squares problem and reduces to solving normal equations. It was also shown in this chapter that computing the cross-correlation vector in the normal equations is equivalent to the CBP image formation method. It was also shown that solving the normal equations for the ground reflectivity parameter vector eliminates the IPI that the CBP algorithm generates. Showing that CBP is an optimal step in the ML image formation method is also a new contribution to stripmap SAR.

The ML imaging method in Chapter 6 was generalized in Chapter 7 by allowing prior information on the scene being imaged to be incorporated, which allows MAP images to be formed. It was also shown in this chapter that if the prior information can be assumed to be in the exponential family of probability distributions, then MAP estimation has a close connection to regularized algorithms. More explicitly, if the prior information is Gaussian, then the MAP estimates can be computed using regularized least-squares algorithms. Two algorithms were derived that form MAP images; one that is a novel use of the BRLS algorithm and the other is a new BFARLS algorithm that can use the structure of the data matrix of an ideal flight (if the flat earth model holds). The BFARLS uses a new block hyperbolic transformation matrix, which is derived in the Appendix. Forming stripmap SAR images via the novel use of the BRLS and the new BFARLS are new contributions to stripmap SAR.

A new model-based autofocus method for stripmap SAR was derived in Chapter 8. This new autofocus method was derived from the forward model presented in Chapter 5. It was shown that this new model-based approach reduces to a constrained subspace fitting problem. Three methods were derived for optimizing this constrained subspace fitting problem; two methods search along the constraints for the optimal solution and the third method linearizes the problem and uses techniques from convex optimization to find the optimal value. All three methods are iterative, in the sense that many iterations are needed to find the optimal value, however, it was also shown that once the optimal value is found and the phase error estimates are applied, the image is in focus. Hence, iterations between the image and data domains are not needed to find the phase error estimates, as

most conventional autofocus methods do. This model-based autofocus method is a new contribution to stripmap SAR.

9.2 Future Work

There are many different research areas in model-based stripmap SAR that were either only briefly mentioned in this dissertation or not addressed at all. The following suggests possible future work that could stem from each chapter contributing to stripmap SAR.

While the stripmap SAR forward model derived in Chapter 5 is very comprehensive, the forward model could be extended to a higher fidelity model that allows for modeling Rayleigh fading effects, electromagnetic coupling between closely spaced reflectors, and signal dispersion.

It was shown in Chapter 5 that the forward model could be constructed for an arbitrary region of interest and that the region of interest closure includes *all* of the ground that contributed to the data of interest. The inclusion of the ground region in the region of interest closure does not take into account that the data is going to be compressed in both range and azimuth. The size of the forward model could be greatly reduced if the region of interest closure could be made smaller. Future work in this area would be to find the *effective* region of interest closure where the bounds are determined by the compressed data.

The ML imaging method in Chapter 6 was demonstrated on simulated data. The ML imaging method still needs to be tested on actual stripmap SAR data. Future work in this area would be to construct a software framework that could build the data matrix in the forward model for a selected region of interest and then form the ML image.

Some insights into stripmap SAR system design were observed in Chapter 6 that could potentially lead to structure in the grammian matrix in the ML imaging method. For example, if the system could be designed to make the grammian matrix diagonally dominant (or perhaps even identity), then the CBP reconstruction would be the optimal reconstruction. Future work in this area would be to determine if different transmitted pulse types, antenna patterns, or even flight paths could be selected to give the grammian matrix a specific structure to make it easier to invert.

The Cramér-Rao lower bound (CRLB) on the variance of the ML estimates was briefly presented in Chapter 6. Future work in this area would be to do a full development of the CRLB on an actual stripmap SAR sensor and compare the variance of the ground reflectivity estimates from actual images to the CRLB.

In Chapter 7 it was shown that MAP ground reflectivity estimation has a close connection to regularized algorithms. Future work in the area of MAP image estimation would be to explore the dependence of the regularization parameter on the SAR system parameters so the optimal value of the regularization parameter could be computed directly. Also, future work in this area would be to explore other algorithms that would form MAP estimated images if the priors were not Gaussian, but still in the family of exponential distributions.

It was stated in Chapter 8 that the convex solver that was used for the linearized convex optimization was sensitive to the conditioning of $\mathcal{M}$. It was also suggested that the linearized convex optimization method could be made more efficient if a solver were tailored to the problem that used the structure of the objective function and the constraints. Future work in the area of model-based autofocus would be create a solver tailored to the linearized convex optimization method.

If the residual phase error in Chapter 8 is known to be band-limited "enough" (with respect to the PRF), then future work may be to see if it would be possible to estimate a decimated phase error vector, then interpolate to obtain the full phase error vector. If this were possible, then the size of the problem could be controlled.

There are several avenues for future work that were not mentioned in this dissertation. One area would be to explore the idea of extending the forward model to coherent change detection (CCD) to see if it would be possible to estimate the phase difference between scenes without explicitly forming either image. Another area would be to explore the possibility of altering the forward model to allow for multiple antennas, then use it to do model-based interferometric SAR and ground moving target indication (GMTI).

References

[1] C. V. Jakowatz and D. E. Wahl, "Three-dimensional tomographic imaging for foliage penetration using multiple-pass spotlight-mode SAR," in *Signals, Systems and Computers, Conference Record of the Thirty-Fifth Asilomar Conference*, 2001.

[2] A. Elsherbini and K. Sarabandi, "Mapping of sand layer thickness in deserts using SAR interferometry," *Geoscience and Remote Sensing, IEEE Transactions*, vol. 48, no. 9, pp. 3550–3559, 2010.

[3] V. Chen and H. Ling, *Time-Frequency Transformations for Radar Imaging and Signal Analysis*. Norwood, MA: Artech House, 2002.

[4] C. V. Jakowatz, D. E. Wahl, P. H. Eichel, D. C. Ghiglia, and P. A. Thompson, *Spotlight-mode Synthetic Aperture Radar: A Signal Processing Approach*. New York, NY: Springer, 1996.

[5] H. Maitre, *Processing of Synthetic Aperture Radar Images*. London, UK; Hoboken, NJ: ISTE; John Wiley and Sons, 2008.

[6] M. Richards, J. Scheer, and W. Holm, *Principles of Modern Radar: Basic Principles*. Raleigh, NC: Scitech, 2010.

[7] R. Sullivan, *Radar Foundations for Imaging and Advanced Concepts*. Raleigh, NC: Scitech, 2000.

[8] S. Kingsley and S. Quegan, *Understanding Radar Systems*. Raleigh, NC: Scitech, 1999.

[9] C. Balanis, *Antenna Theory: Analysis and Design*. Hoboken, NJ: John Wiley and Sons, 2005.

[10] M. Çetin, *Feature-Enhanced Synthetic Aperture Radar Imaging*. Ph.D. dissertation, Boston University, 2001.

[11] M. Çetin and W. Karl, "Feature-enhanced synthetic aperture radar image formation based on nonquadratic regularization," *Image Processing, IEEE Transactions*, vol. 10, no. 4, pp. 623–631, Apr. 2001.

[12] J. Skinner, B. Kent, R. Wittmann, D. Mensa, and D. Andersh, "Normalization and interpretation of radar images," *Antennas and Propagation, IEEE Transactions*, vol. 46, no. 4, pp. 502–506, Apr. 1998.

[13] B. Wang, *Digital Signal Processing Techniques and Applications in Radar Image Processing*. Hoboken, NJ: John Wiley and Sons, 2008.

[14] M. Richards, *Fundamentals of Radar Signal Processing*. New York, NY: McGraw-Hill, 2005.

[15] I. G. Cumming and F. H. Wong, *Digital Processing of Synthetic Aperture Radar Data: Algorithms and Implementation.* Boston, MA: Artech House, 2005.

[16] M. Bertero and P. Boccacci, *Introduction To Inverse Problems in Imaging.* Bristol, UK: Institute of Physics Publishing (IoP), 1998.

[17] S. Luttrell, "A Bayesian derivation of an iterative autofocus/super resolution algorithm," *Inverse Problems*, vol. 6, Dec. 1990.

[18] C. Oliver and S. Quegan, *Understanding Synthetic Aperture Radar Images.* Raleigh, NC: SciTech, 2004.

[19] J. Horrell, A. Knight, and M. Inggs, "Motion compensation for airborne SAR," in *Communications and Signal Processing, Proceedings of the 1994 IEEE South African Symposium*, pp. 128–131, 1994.

[20] A. Potsis, A. Reigber, J. Mittermayer, A. Moreira, and N. Uzunoglou, "Sub-aperture algorithm for motion compensation improvement in wide-beam SAR data processing," *Electronics Letters*, vol. 37, no. 23, pp. 1405–1407, 2001.

[21] R. K. Raney, H. Runge, R. Bamler, I. G. Cumming, and F. H. Wong, "Precision SAR processing using chirp scaling," *Geoscience and Remote Sensing, IEEE Transactions*, vol. 23, no. 4, July 1994.

[22] A. Moriera, J. Mittermayer, and R. Scheiber, "Extended chirp scaling algorithm for air- and spaceborne SAR data processing in stripmap and scansar imaging modes," *Geoscience and Remote Sensing, IEEE Transactions*, vol. 34, no. 5, Sept. 1996.

[23] M. Soumekh, *Synthetic Aperture Radar Signal Processing: With Matlab Algorithms.* Hoboken, NJ: John Wiley and Sons, 1999.

[24] O. Frey, E. H. Meier, and D. R. Nuesch, "Processing SAR data of rugged terrain by time-domain back-projection," *Proceedings SPIE*, vol. 5980, 2005.

[25] O. Frey, E. H. Meier, and D. R. Nuesch, "A study on integrated SAR processing and geocoding by means of time-domain backprojection," in *Proceedings of the International Radar Symposium*, Berlin, 2005.

[26] S. Xiao, J. Munson, D.C., S. Basu, and Y. Bresler, "An $n^2 \log(n)$ back-projection algorithm for SAR image formation," in *Signals, Systems and Computers, Conference Record of the Thirty-Fourth Asilomar Conference*, 2000.

[27] L. Ulander, H. Hellsten, and G. Stenstrom, "Synthetic-aperture radar processing using fast factorized back-projection," *Aerospace and Electronic Systems, IEEE Transactions*, vol. 39, no. 3, pp. 760–776, 2003.

[28] S. Bin and J. Haibo, "Feature enhanced synthetic aperture radar image formation," in *Electronic Measurement and Instruments, 8th International Conference*, 2007.

[29] T. K. Moon and W. C. Stirling, *Mathematical Methods and Algorithms for Signal Processing.* Upper Saddle River, NJ: Prentice Hall, 2000.

[30] A. H. Sayed, *Adaptive Filters*. Hoboken, NJ: John Wiley and Sons, 2008.

[31] A. H. Sayed, *Fundamentals of Adaptive Filtering*. Hoboken, NJ: John Wiley and Sons, 2003.

[32] R. Morrison, M. Do, and D. Munson, "MCA: A multichannel approach to SAR autofocus," *Image Processing, IEEE Transactions*, vol. 18, no. 4, pp. 840–853, 2009.

[33] P. Samczynski and K. Kulpa, "Coherent mapdrift technique," *Geoscience and Remote Sensing, IEEE Transactions*, vol. 48, no. 3, pp. 1505–1517, 2010.

[34] T. Calloway and G. Donohoe, "Subaperture autofocus for synthetic aperture radar," *Aerospace and Electronic Systems, IEEE Transactions*, vol. 30, no. 2, pp. 617–621, Apr. 1994.

[35] J. Wang and X. Liu, "SAR minimum-entropy autofocus using an adaptive-order polynomial model," *Geoscience and Remote Sensing Letters, IEEE*, vol. 3, no. 4, pp. 512–516, 2006.

[36] R. L. Morrison and M. N. Do, "A multichannel approach to metric-based SAR autofocus," in *Image Processing, IEEE International Conference*, vol. 2, 2005.

[37] C. V. Jakowatz and D. E.Wahl, "Eigenvector method for maximum-likelihood estimation of phase errors in synthetic-aperture-radar imagery," *Journal of the Optical Society of America A*, vol. 10, no. 12, 1993.

[38] F. Berizzi, G. Corsini, M. Diani, and M. Veltroni, "Autofocus of wide azimuth angle SAR images by contrast optimisation," in *Geoscience and Remote Sensing Symposium, 'Remote Sensing for a Sustainable Future,' International*, vol. 2, pp. 1230–1232, May 1996.

[39] R. L. Morrison, M. N. Do, and D. C. Munson, "SAR image autofocus by sharpness optimization: a theoretical study," *Image Processing, IEEE Transactions*, vol. 16, no. 9, pp. 2309–2321, 2007.

[40] M. Viberg and B. Ottersten, "Sensor array processing based on subspace fitting," *Signal Processing, IEEE Transactions*, vol. 39, no. 5, pp. 1110–1121, May 1991.

[41] S. Boyd and L. Vandenberghe, *Convex Optimization*. Cambridge, UK: Cambridge, 2004.

[42] M. Grant and S. Boyd, "CVX: Matlab software for disciplined convex programming, version 1.21," `http://cvxr.com/cvx`, Feb. 2011.

[43] G. H. Golub and C. F. V. Loan, *Matrix Computations*. Baltimore, MD: Johns Hopkins University Press, 1989.

[44] R. Schreiber and B. Parlett, "Block reflectors: theory and computation," *SIAM Journal on Numerical Analysis*, vol. 25, no. 1, 1988.

[45] S. Singer and S. Singer, "Orthosymmetric block reflectors," *Linear Algebra and its Applications*, vol. 429, no. 5-6, pp. 1354–1385, 2008.

Appendix

Appendix

Circular and Hyperbolic Transformations

This appendix derives the block transformations that are needed in the BFARLS algorithm. Both the scalar FARLS and the block FARLS algorithms need a J-unitary matrix Θ in order to transform the pre-array into the post-array. In both cases Θ can be factored into the product of a unitary circular transformation and a J-unitary hyperbolic transformation

$$\Theta = \Theta_c \Theta_h, \tag{A.1}$$

where Θ_c are the circular transformations and Θ_h are the hyperbolic transformations.

In the scalar FARLS, the circular transformations can be accomplished using either Givens or Householder transformations and the hyperbolic transformations can be accomplished by using the Givens or Householder hyperbolic transformations. In this appendix, we will be working with Householder transformations.

A.1 Traditional Circular and Hyperbolic Householder Transformations

The circular Householder transformation is well known, [29, 43]. Most often the transformation is employed to "compress" the energy of a vector or a column of a matrix onto a coordinate axis, thereby introducing zeros into the transformed vector or column.

Consider the complex vector $\mathbf{a} \in \mathbb{C}^n$. To compress the energy onto the i^{th} coordinate, the Householder vector is formed as

$$\mathbf{v} = \mathbf{a} \pm e^{j\phi(a_i)} ||\mathbf{a}||_2 \mathbf{e}_i, \tag{A.2}$$

where $\phi(a_i)$ is the angle of the i^{th} element of $\mathbf{a}$, [30]. The Householder transformation is then computed as

$$Q = I - 2\frac{\mathbf{v}\mathbf{v}^H}{\mathbf{v}^H\mathbf{v}}. \tag{A.3}$$

It is straightforward to verify that Q is a unitary matrix (length preserving) and involutary (applied twice to a vector returns the original vector). Applied to a generic vector $\mathbf{x}$, $Q\mathbf{x}$ is the resulting vector that has been reflected about $\mathbf{v}^{\perp}$. However, applied to the vector $\mathbf{a}$ (from which Q was constructed), $Q\mathbf{a} = ||\mathbf{a}||_2\mathbf{e}_i$.

As an illustration, consider the following matrix (written in terms of its columns)

$$A = \begin{bmatrix} \mathbf{a}_1 & \mathbf{a}_2 & \cdots & \mathbf{a}_n \end{bmatrix}. \tag{A.4}$$

Applying a circular Householder transformation with the intention of "compressing" the energy of the first column into the first element gives

$$QA = \begin{bmatrix} ||\mathbf{a}_1||_2\mathbf{e}_1 & Q\mathbf{a}_2 & \cdots & Q\mathbf{a}_n \end{bmatrix} = \tilde{A}. \tag{A.5}$$

Notice that $\tilde{A}^H\tilde{A} = A^HQ^HQA = A^HA$; thus the Householder transformation applied to a matrix preserves the Frobenius norm and the matrix 2-norm.

The hyperbolic Householder transformation is a slight modification to the circular transformation. Replacing the Euclidean norm with the J-norm, the construction of the hyperbolic Householder vector that will "compress" the energy of $\mathbf{a}$ (with respect to the J-norm) onto the i^{th} coordinate axis is

$$\mathbf{v} = \mathbf{a} \pm e^{j\phi(a_i)}||\mathbf{a}||_J\mathbf{e}_i, \tag{A.6}$$

where

$$||\mathbf{v}||_J = \sqrt{|\mathbf{v}^HJ\mathbf{v}|}. \tag{A.7}$$

The hyperbolic Householder transformation is also a slight modification of the circular transformation

$$Q_J = I - 2\frac{\mathbf{v}\mathbf{v}^H}{\mathbf{v}^H J\mathbf{v}}J. \tag{A.8}$$

It is straightforward to verify that Q_J is J-unitary (*i.e.* $Q_J^H J Q_J = Q_J J Q_J^H = J$) and is also involutary. The inverse of Q_J is $Q_J^{-1} = JQ_J^H J$ and the inverse of Q_J^H is $(Q_J^H)^{-1} = JQ_J J$.

A.2 Block Circular and Hyperbolic Householder Transformations

The generalization of Householder transformations are called block reflectors. Block reflector transformations are common in the literature and can be either symmetric or non-symmetric [44, 45]; however, most produce a resulting matrix that has special properties such as being upper-triangular or block upper-triangular and zeros elsewhere. Sometimes all that is needed is a transformation that compresses the energy of a matrix into a square submatrix, regardless of the symmetry of the transformation and with no other requirement other than being matrix norm preserving (this is analogous to compressing all the energy of a vector into a single element). To illustrate this result, consider the matrix $A \in \mathbb{C}^{m\times n}$. If A does not have full row rank (or $m > n$), then we can zero the rows of A until A has the following form

$$\Theta A = \begin{bmatrix} \tilde{A}_{n\times n} \\ 0_{(m-n)\times n} \end{bmatrix}. \tag{A.9}$$

If $\tilde{A}_{n\times n}$ were upper-triangular, then the traditional Householder matrix could be used or if $\tilde{A}_{n\times n}$ were to be block upper-triangular many of the block reflector algorithms in the literature could be used [45]. Likewise, if $\tilde{A}_{n\times n}$ were to be symmetric. We now develop a method for generating a generic $\tilde{A}_{n\times n}$.

Without loss of generality, let A be a tall matrix ($m > n$) and have full column rank. The range of A is the subspace spanned by the columns of A

$$\mathcal{R}(A) = \text{span}\left\{ \begin{bmatrix} \mathbf{a}_1 & \mathbf{a}_2 & \cdots & \mathbf{a}_n \end{bmatrix} \right\}, \tag{A.10}$$

where $\mathbf{a}_i$ is the i^{th} column of A. The range of A can be extended to form a basis for the m-dimensional vector space $\mathcal{S}$

$$\mathcal{S} = \text{span}\left\{ \begin{bmatrix} \mathbf{a}_1 & \mathbf{a}_2 & \cdots & \mathbf{a}_n & \mathbf{q}_1 & \mathbf{q}_2 & \cdots & \mathbf{q}_{m-n} \end{bmatrix} \right\}. \tag{A.11}$$

The vectors $\mathbf{q}_i$ can be found such that $\mathbf{q}_i^H \mathbf{q}_j = \delta_{ij}$ and $A^H \mathbf{q}_i = \mathbf{0}$, $\forall i$ (*i.e.* the vectors $\mathbf{q}_i$ are orthonormal (with respect to each other) and span the null-space of A^H). Thus, $\mathcal{S}$ is the direct sum of the range of A and the null-space of A^H

$$\mathcal{S} = \mathcal{R}(A) \oplus \mathcal{N}(A^H). \tag{A.12}$$

Let U denote the matrix whose columns are composed of the $\mathbf{q}_i$

$$U = \begin{bmatrix} \mathbf{q}_1 & \mathbf{q}_2 & \cdots & \mathbf{q}_{m-n} \end{bmatrix}. \tag{A.13}$$

The conjugate transpose of the Householder matrix Q such that

$$Q^H U = \begin{bmatrix} 0_{n\times(m-n)} \\ \Lambda_{(m-n)\times(m-n)} \end{bmatrix}, \tag{A.14}$$

where $\Lambda_{(m-n)\times(m-n)}$ is an $(m-n)\times(m-n)$ reverse-diagonal matrix, such that $\Lambda^H\Lambda = I$, is exactly the matrix that produces the result we desire to have in equation (A.9). To be explicit,

$$Q^H A = \begin{bmatrix} \tilde{A}_{n\times n} \\ 0_{(m-n)\times n} \end{bmatrix}. \tag{A.15}$$

Due to the $\mathbf{q}_i$ being orthonormal, the resulting matrix in equation (A.14) can be produced by simple Householder transformations on U where the energy in each column is being compressed down the columns (instead of up the columns as is done in QR decompositions).

To show this result, note that since the matrix Q is constructed from Householder transformations, it has the factorization

$$Q = Q_1 Q_2 \cdots Q_{m-n}, \tag{A.16}$$

where Q_1 is constructed from $\tilde{\mathbf{q}}_1 = \mathbf{q}_1 \pm e^{j\phi(q_m)}\mathbf{e}_m$ (where $||\mathbf{q}_i||_2 = 1$ has been used). To be explicit,

$$Q_1 = I - 2\frac{\tilde{\mathbf{q}}_1 \tilde{\mathbf{q}}_1^H}{\tilde{\mathbf{q}}^H \tilde{\mathbf{q}}}. \tag{A.17}$$

Let $\mathbf{v}$ be a vector that is orthogonal to $\mathbf{q}_1$. Then applying Q_1 constructed from $\tilde{\mathbf{q}}_1 = \mathbf{q}_1 + e^{j\phi(q_m)}\mathbf{e}_m$ to $\mathbf{v}$ gives

$$\begin{aligned}
Q_1^H \mathbf{v} &= \mathbf{v} - 2\frac{\tilde{\mathbf{q}}_1^H \mathbf{v}}{\tilde{\mathbf{q}}_1^H \tilde{\mathbf{q}}_1}\tilde{\mathbf{q}}_1 && \text{(A.18)}\\
&= \mathbf{v} - 2\frac{(\mathbf{q}_1 + e^{j\phi(q_m)}\mathbf{e}_m)^H \mathbf{v}}{(\mathbf{q}_1 + e^{j\phi(q_m)}\mathbf{e}_m)^H (\mathbf{q}_1 + e^{j\phi(q_m)}\mathbf{e}_m)}(\mathbf{q}_1 + e^{j\phi(q_m)}\mathbf{e}_m) && \text{(A.19)}\\
&= \mathbf{v} - \frac{e^{-j\phi(q_m)} v_m}{1 + |q_{1,m}|}(\mathbf{q}_1 + e^{j\phi(q_m)}\mathbf{e}_m) && \text{(A.20)}\\
&= \mathbf{v} - \frac{v_m}{1 + |q_{1,m}|}\begin{bmatrix} e^{-j\phi(q_m)}\mathbf{q}_{1,1:m-1} \\ |q_{1,m}| + 1 \end{bmatrix} && \text{(A.21)}\\
&= \begin{bmatrix} \mathbf{v}_{1:m-1} \\ v_m \end{bmatrix} - \begin{bmatrix} \frac{e^{-j\phi(q_m)} v_m}{1+|q_{1,m}|}\mathbf{q}_{1,1:m-1} \\ v_m \end{bmatrix} && \text{(A.22)}\\
&= \begin{bmatrix} \mathbf{v}_{1:m-1} - \frac{e^{-j\phi(q_m)} v_m}{1+|q_{1,m}|}\mathbf{q}_{1,1:m-1} \\ 0 \end{bmatrix}. && \text{(A.23)}
\end{aligned}$$

Similarly, constructing Q_1 from $\tilde{\mathbf{q}}_1 = \mathbf{q}_1 - e^{j\phi(q_m)}\mathbf{e}_m$ and applying to $\mathbf{v}$ gives

$$Q_1^H \mathbf{v} = \begin{bmatrix} \mathbf{v}_{1:m-1} + \frac{e^{-j\phi(q_m)}v_m}{1-|q_{1,m}|}\mathbf{q}_{1,1:m-1} \\ 0 \end{bmatrix}. \tag{A.24}$$

These two cases can be combined; let $\tilde{\mathbf{q}}_1 = \mathbf{q}_1 \pm e^{j\phi(q_m)}\mathbf{e}_m$, then

$$Q_1^H \mathbf{v} = \begin{bmatrix} \mathbf{v}_{1:m-1} \mp \frac{e^{-j\phi(q_m)}v_m}{1\pm|q_{1,m}|}\mathbf{q}_{1,1:m-1} \\ 0 \end{bmatrix}, \tag{A.25}$$

where $\mathbf{v}_{1:m-1}$ is the vector formed from the first $m-1$ elements of $\mathbf{v}$ and v_m is the m^{th} element of $\mathbf{v}$.

Applying Q_1 to U gives

$$Q_1^H U = \begin{bmatrix} \mp e^{j\phi(q_m)}\mathbf{e}_m & Q_1^H\mathbf{q}_2 & \cdots & Q_1^H\mathbf{q}_{m-n} \end{bmatrix}. \tag{A.26}$$

Using that the columns of U are orthonormal, substituting $\mathbf{q}_i$ $(2 \le i \le m-n)$ for $\mathbf{v}$ in equation (A.25) gives

$$Q_1^H \mathbf{q}_i = \begin{bmatrix} \mathbf{q}_{i,1:m-1} \mp \frac{q_{i,m}e^{-j\phi(q_{1,m})}}{1\pm|q_{1,m}|}\mathbf{q}_{1,1:m-1} \\ 0 \end{bmatrix}, \quad 2 \le i \le m-n, \tag{A.27}$$

where $q_{l,m}$ is the m^{th} element of vector $\mathbf{q}_l$. Forming Q_2 from $Q_1^H\mathbf{q}_2$ and applying to $Q_1^H U$ gives

$$Q_2^H Q_1^H U = \begin{bmatrix} \mp e^{j\phi(q_m)}\mathbf{e}_m & \mp e^{j\phi([Q_1^H\mathbf{q}_2]_{m-1})}\mathbf{e}_{m-1} & Q_2^HQ_1^H\mathbf{q}_3 & \cdots & Q_2^HQ_1^H\mathbf{q}_{m-n} \end{bmatrix}. \tag{A.28}$$

Continuing on in this manner shows that

$$Q^H U = Q_{m-n}^H \cdots Q_2^H Q_1^H U = \begin{bmatrix} 0_{n\times(m-n)} \\ \Lambda_{(m-n)\times(m-n)} \end{bmatrix}, \tag{A.29}$$

as claimed.

Applying Q_1 to the matrix A gives

$$Q_1^H A = \begin{bmatrix} Q_1^H \mathbf{a}_1 & Q_1^H \mathbf{a}_2 & \cdots & Q_1^H \mathbf{a}_{m-n} \end{bmatrix}. \tag{A.30}$$

Using that the columns of A are orthogonal to the $\mathbf{q}_i$ (by construction) and substituting $\mathbf{a}_i$ for $\mathbf{v}$ in equation (A.25) gives

$$Q_1^H \mathbf{a}_i = \begin{bmatrix} \mathbf{a}_{i,1:m-1} \mp \frac{e^{-j\phi(q_m)} a_{i,m}}{1 \pm |q_{1,m}|} \mathbf{q}_{1,1:m-1} \\ 0 \end{bmatrix}. \tag{A.31}$$

Since equation (A.31) holds for any column of A, it is clear that $Q^H A$ has compressed all of the energy in the bottom row of A into the rows above. Continuing in this manner with Q_2 through Q_{m-n} shows that

$$Q^H A = Q_{m-n}^H \cdots Q_2^H Q_1^H A = \begin{bmatrix} \tilde{A}_{n\times n} \\ 0_{(m-n)\times n} \end{bmatrix}. \tag{A.32}$$

The geometric interpretation of this is that the orthonormal vectors that span the null space of A^H are being aligned with the coordinate axes $\mathbf{e}_{n+1}$ through $\mathbf{e}_m$ and thus the reflected range cannot have any components on those axes.

The block FARLS needs the J-unitary equivalent to equation (A.15). Under a strict condition (which will be stated below), a similar result holds for J-unitary block reflectors. Assume that the condition holds, let U be the same as above (*i.e.* the columns of U are orthonormal and span the null-space of A^H), then the inverse of the complex transpose of

the J-unitary block reflection matrix Q_J such that

$$Q_J U = \begin{bmatrix} 0_{n\times(m-n)} \\ C_{(m-n)\times(m-n)} \end{bmatrix}, \tag{A.33}$$

where $C_{(m-n)\times(m-n)}$ is an $(m-n)\times(m-n)$ reverse-lower triangular matrix, is the matrix that produces the desired result

$$(Q_J^H)^{-1} A = J Q_J J A = \begin{bmatrix} \tilde{A}_{n\times n} \\ 0_{(m-n)\times n} \end{bmatrix}. \tag{A.34}$$

The matrix Q_J can be factored into a product of J-unitary Householder transformations

$$Q_J = Q_{J,(m-n)} \cdots Q_{J,1}, \tag{A.35}$$

where each $Q_{J,i}$ has the same construction as in equation (A.8).

The condition that must hold to produce the results in equation (A.34) is

$$\hat{\mathbf{q}}_i^H J \hat{\mathbf{q}}_i = \text{sign}(J_{i,i}), \tag{A.36}$$

where $\hat{\mathbf{q}}_i$ is the vector that $Q_{J,i}$ is constructed from.

The result in equation (A.34) is exactly what we need for the block FARLS algorithm. If the stated condition fails, it is an indication that numerical stability has set in and the block FARLS starts to diverge.

Vita

Roger D. West

Education

- Ph.D. Electrical and Computer Engineering, Utah State University, Logan, UT, 2011.
- M.S. Electrical and Computer Engineering, Utah State University, Logan, UT, 2008.
- B.S. Electrical and Computer Engineering (Summa Cum Laude, Minor in Mathematics), Utah State University, Logan, UT, 2008.
- A.S. Electrical and Computer Engineering, Salt Lake Community College, Salt Lake City, UT, 2005.

Awards

- Space Dynamics Laboratory *Tomorrow Fellowship* recipient, 2008-2011.
- Utah State University *Outstanding Graduate Teaching Assistant*, 2007-2008.
- Utah State University *Presidential Transfer Scholarship* recipient, 2005-2006.

Published Conference Papers

- Maximum Likelihood Estimation of Ground Reflectivity from Synthetic Aperture Radar Data, Roger West, Jake Gunther, and Todd Moon, in *56th Annual Meeting of the MSS Tri-Services Radar Symposium*, 2010.

- A Novel Block Fast Array RLS Algorithm Applied to Linear Flight Strip-Map SAR Images, Roger West, Todd Moon, and Jake Gunther, in *Signals, Systems and Computers (ASILOMAR), Conference Record of the Forty Fourth Asilomar Conference*, 2010.

- Forming Regularized Maximum Likelihood Strip-Map Synthetic Aperture Radar Images Using the Block RLS Algorithm, Roger West, Jake Gunther, and Todd Moon, in *Digital Signal Processing Workshop and IEEE Signal Processing Education Workshop (DSP/SPE)*, 2011.

- Maximum Likelihood Synthetic Aperture Radar Image Formation for Highly Nonlinear Flight Tracks, Jake Gunther, Roger West, Nate Crookston, and Todd Moon, in *Digital Signal Processing Workshop and IEEE Signal Processing Education Workshop (DSP/SPE)*, 2011.

- Model-Based Autofocus for Strip-Map SAR Images Formed via Convolution Back-Projection, Roger West, Jake Gunther, and Todd Moon, in *57th Annual Meeting of the MSS Tri-Services Radar Symposium*, 2011. (Accepted)

- STARTLE: An Open-Source Software Tool for SAR Signal Processing and Imaging, Jake Gunther, Nate Crookston, Roger West, and Todd Moon, in *57th Annual Meeting of the MSS Tri-Services Radar Symposium*, 2011. (Accepted)